Digital and Analog Hologram Tomography for Medical Applications

Inaugural-Dissertation

zur
Erlangung des Doktorgrades der
Mathematisch-Naturwissenschaftlichen Fakultät
der Heinrich-Heine-Universität Düsseldorf

vorgelegt von
Sven Hirsch
aus Idar-Oberstein

Dezember 2006

Referent: Prof. Dr. P. Hering

Koreferent: Prof. Dr. K. Schierbaum

Tag der mündlichen Prüfung: 29.1.2007

Gedruckt mit Genehmigung der
Mathematisch-Naturwissenschaftlichen Fakultät der
Heinrich-Heine-Universität Düsseldorf

Zusammenfassung

Holographische Topometrie birgt das einzigartige Potential der Aufnahme von Oberflächen selbst von bewegten Objekten und liefert dabei eine präzise passende Textur. Beide Anforderungen werden von keiner anderen 3D Vermessungsmethode erfüllt. In der vorliegenden Arbeit werden Verbesserungen an der analogen Methode vorgestellt und eine digitale Methode neu entwickelt.

Der Erfassungs- und der Auswerteprozess sind entkoppelt. Ein Portraithologramm wird mit einer kurzen Aufnahmezeit (20 ns) erstellt, womit keine Bewegungartefakte entstehen. Das Hologramm trägt die gesamte räumliche Information des Objektes, Phase und Amplitude sind gespeichert. Nach der nasschemischen Entwicklung wird das Hologramm mit einem Dauerstrich-Laser optisch rekonstruiert und zeigt das reele Bild. Ein Scanner geht schrittweise durch das reele Bild und nimmt es Schicht für Schicht auf. Durch digitale Bildverarbeitung werden Oberfläche und die entsprechende Textur des Objektes extrahiert. Höhe und Textur werden zu einem digitalen 3D Modell zusammengeführt.

Eine holographische Kamera zur mobilen Aufnahme von analogen Hologrammen wird vorgestellt, mit der erstmalig Hologrammaufnahmen bei Tageslicht möglich sind. Das System ist bedienungfreundlich und wird von medizinischem Personal verwendet. Eine optische Rekonstruktionseinheit wird für dieses System aufgebaut, die den hohen Ansprüchen einer artefaktfreien Digitalisierung des reelen Bildes genügt.

Durch diese Arbeit werden bedeutende Innovationen in die analoge Methode eingebracht. Ein Flächendetektor ersetzt einen kommerziellen Flachbettscanner und eliminiert die Schwächen in Geschwindigkeit, Dynamikumfang, mechanischer Instabilität und von Bildartefakten. Dieser vollkommen neuartige High-Performance Scanner verwendet einen Röntgen-Flatpaneldetektor (FPD) zur flächenhaften Aufnahme jedes Bildes. Der FPD wird für die optische Erfassung angepasst, fabrikationsbedingte Bildfehler des Detektors werden ausgeräumt. Damit gehen viele Verbesserungen einher. Das reele Bild kann nun online betrachtet werden, die Bildrate von 10 Hz reduziert den Scanprozess drastisch von 2 Stunden auf 30 Sekunden. Der Dynamikumfang von 12 bit ermöglicht eine Aufnahme mit hoher Empfindlichkeit. Durch die Beseitigung von Bildartefakten und von mechanischen Unzulänglichkeiten wird eine Rekonstruktion mit deutlich erhöhter Qualität erreicht. Die Positionierung des Sensors ist genau senkrecht zur Scanachse, womit geometrische Abberationen systematisch entfallen.

Die zweite Errungenschaft dieser Arbeit ist die Einführung der volldigitalen holographischen Topometrie, bei der ein CCD-Sensor zur Hologrammaufnahme dient. Verglichen mit der analogen Methode erreicht die digitale Holographie, bedingt durch Beschränkung der Sensorauflösung, nur ein geringes Sichtfeld. Die zur numerischen Rekonstruktion notwendigen Algorithmen werden implementiert, Filtertechniken verbessern die Rekonstruktionsqualität. Eine Skalierung führt zu Bildstapeln mit konstanter lateraler Skalierung und geometrisch korrekter Positionierung. Ein Algorithmus wird implementiert, der die Rekonstruktion echtzeitfähig auf der Grafikkarte berechnet, dabei wird eine Beschleunigung um den Faktor 100 bei großen Bilder erzielt. Eine neue Eichmethode zur Festlegung des Ursprungs des Referenzstrahles wird entwickelt, bei der lediglich ein Objekt bekannter Größe vermessen wird. Mit optimaler Beleuchtung kann aus digitalen Hologrammen bereits Haut dargestellt werden, was einen bedeutenden Schritt zur Gesichtsvermessung darstellt. Mit strukturierter Beleuchtung wird die Sichtbarkeit der Oberfläche eines Objektes verbessert.

Es wird gezeigt, dass Höhenkarten aus numerisch rekonstruierten Bildstapeln erstellt werden können. Zur Vermeidung von Artifakten durch die Specklemuster wird die Skalierung erst nach der Oberflächenfindung durchgeführt. Textur und Höhenprofil werden zur gleichen Zeit aus dem Bild extrahiert. Es werden Anstrengungen unternommen, Aufnahmen verschiedener Perspektiven zu synthetisieren und erste vielversprechende Ergebnisse hierzu werden präsentiert. Dazu werden Eichobjekte aus den verschiedenen Perspektiven aufgenommen und die Transformationsmatrix im Objektraum bestimmt.

Zwei medizinische Anwendungen der analogen Hologrammtopometrie werden präsentiert, die beide nur durch die hier vorgestellten instrumentellen Verbesserungen möglich sind. Im ersten Beispiel werden Möglichkeiten der Planung und Dokumentation von Spaltkorrekturen gezeigt. Selbst geringe Kontraste der kindlichen Hautporen werden vom neuen Sensor detektiert und führen zu exzellenten Gesichtsmodellen. Diese 3D Information wird zur Dokumentation und Bewertung von Operationstechniken der Spaltkorrektur bei Säuglingen verwendet. Die zweite Anwendung beschreibt die Quantifizierung des Einflusses der Schwerkraft auf Weichgewebe. Eine Zahnspange wird zur Registrierung der beiden Gesichtsmodelle des aufrechten und des liegenden Gesichtes verwendet. Durch manuelles Verfolgen von Merkmalen in der Textur konnten erste Verschiebungsvektorfelder extrahiert werden. Eine maximale Hautbewegung von 6 mm wird in der oberen Wangenregion festgestellt, verglichen mit einer volumetrisch ermittelten Verschiebung von nur 1 - 2.3 mm.

Synopsis

Holographic topometry has the unique potential to capture the surface of a living subject even in motion and with an accurately fitting texture. Both tasks cannot be accomplished by any other 3D imaging method. In this thesis the analog method was improved and a digital method newly developed.

The capture and the evaluation processes are decoupled. A pulsed hologram is captured with a short exposure time (20 ns), avoiding any motion artifacts. The hologram contains the complete spatial information of the object; phase and amplitude are recorded. After a wet-chemical processing the analog hologram is optically reconstructed with a continuous wave laser to reveal the real image. The scanner physically travels through the real image to capture it slice-by-slice. Digital image processing extracts the object surface and the appropriate texture. Height and texture information are combined into a digital 3D model.

A holographic camera system for the mobile capture of analog holograms is presented, which, for the first time, allows to capture holograms in daylight. It is easy to operate and enables the use of the system by medical personnel. An optical reconstruction unit was designed for this system to meet the high demands for a scanning of the real image without artifacts.

In the analog method major innovations are introduced with this thesis. Most prominently, a full-sized area detector replaced the commercial flatbed scanner to eliminate the shortcomings of speed, dynamic range, mechanical instability and image artifacts. This novel high performance scanner uses a X-ray flat-panel detector (FPD) as an area sensor to capture each image at once. The FPD was modified to fulfill the the optical sensing needs, artifacts of the FPD were eliminated. The improvements introduced by this new instrument are manifold. The real image may now be monitored on-line, the scan rate of 10 Hz drastically reduces the scan process from 2 hours to 30 seconds. The 12 bit dynamic range allows to record the slice with higher sensitivity. By eliminating image artifacts and mechanical issues, the device led to a vastly improved reconstruction performance in all respects. The positioning of the sensor is exactly perpendicular to the scan axis, which resolves the geometric aberrations systematically.

The second absolute novelty is the introduction of digital holographic topometry, where a CCD sensor is used to record the hologram. Compared to the analog method, the field-of-view is restricted for digital holography due to limitations of the sensor resolution. The algorithms necessary for the numerical reconstruction of digital holograms were implemented. Filter techniques improve the quality of the reconstruction. A scaling procedure leads to image stacks with constant lateral scaling and a geometrically correct positioning. An algorithm was implemented that performs the reconstruction calculation on the graphics hardware, which results in a nearly 100 fold speed increase for the reconstruction of large images. A unique gauging method was developed to adjust the reference beam origin, merely by measuring a target of known extent. With an optimal illumination, human skin can already be visualized in digital holograms, which is a major advance towards facial topometry. With structured illumination the surface visibility may be additionally enhanced for any given object.

It was demonstrated that surface maps can be established from numerically reconstructed image stacks. Due to the speckle pattern progression it is necessary to perform the scaling corrections after the surface finding. The texture and the height profile were extracted at the same time. Efforts to synthesize different perspectives are presented and show first promising results. It is the strategy to gauge the perspectives by known targets and determine the transformation matrix in the object space.

Two medical applications of analog hologram topometry are presented, both are only feasible due to the instrumental improvements presented in this thesis. The first example shows the planning possibilities and documentation for a cleft lip correction. The subtle image contrasts introduced by the infantile skin pores are detectable with the new device and lead to an excellent 3D surface model. This 3D information is used for the documentation and evaluation of cleft correction techniques. The second application shows the quantification of gravitational effects on soft tissue. A jig fixed to the teeth was used to register the two facial models of an upright and a reclined face. By manually tracking features in the texture map, a first sparse displacement map was extracted. The skin shifted maximally in the upper cheek region by a distance of 6 mm, compared to a volumetrically determined difference of only 1 - 2.3 mm.

Contents

Chapter 1

Introduction

In 1971 Dennis Gabor was rewarded the Nobel prize “for his invention and development of the holographic method”. Yet the success of holography did no come overnight ([Joh06]). It is rather an example where the theory is not as compelling as the directly perceivable visual effect.

The origin of holography traces back to a time when lasers were not yet invented. The concept to separate the recording from the reconstruction was already used by microscope designer Ernst Abbe (1840-1905), and was physically implemented by his scholar Miecislav Wolfke (1883-1947) in 1920. Later, from 1939, Sir Lawrence Bragg (1890-1971) proposed a two-step process to enhance the resolution power of a microscope, recording with X-rays and reading out with visible light to leverage the inbuilt magnification of 10,000 due to the wavelength ratio.

In 1947 Gabor (1900-1979) had the idea for improving the resolution of a microscope by recording a diagram of the amplitude and the phase of the wave at the same time, and named it hologram (from the Greek, holos - whole, graphe - writing). Gabor imagined recording a sample by exposition to an electron beam and to read out the recording by visible light. As Bragg, he imagined utilizing the magnification due to wavelength shift to reach a resolution of below 0.01 nm, aiming to visualize a virus. The three-dimensional nature of the recording did not occur to him. He performed a proof of concept by recording and reconstructing with light and communicated the results of his ’holoscope’ to influential British scientists (e.g. Bragg). Gabor published his first paper on wavefront reconstruction in 1948 ([Gab48]). At first even Bragg was sceptical when reading about the concept, noting it seemed "something like a miracle to me that it should work". Yet it was the demonstrations shepherded by the influential Sir Lawrence Bragg that caught the attention for his revolutionary invention. The magic of restoring a seemingly degraded diffraction pattern to a readable information stunned the spectators. The three dimensional property of the holographic reconstruction was alluded to but the phenomenon was not linked to stereoscopic vision.

"The name ’hologram’ is not unjustified, as the photograph contains the total information required for reconstructing the object, which can be two-dimensional or three-dimensional". ([Gab49])

Many researchers were intrigued by the concept of wavefront recording or diffraction microscopy and contributed much to the clarification and generalization of Gabor’s initial idea. Although the interest was euphoric in the first years, towards the year 1957 all development efforts had ceased and even Gabor seemed to have dropped the concept of the diffraction microscope. At the time a coherent light source consisted of a mercury lamp using a pinhole (3 μm) and filters. The weak intensity and the low temporal coherence were the limiting factor for the further progress of the method. One main restriction was the overlap of different diffraction orders which was not solved at the time.

Optical holography started again with the invention of the laser in the early 1960s. These

efficient coherent light sources were ideal for holography and led to the production of the first off-axis optical holograms by Emmeth Leith and Juris Upatnieks in late 1962 ([LU62], [LU63]), who intended to use the method for reconstructing radar images. There was little response of the scientific community about the method with these first results. The lasers at the time had poor temporal coherence and mode stability, and their holograms where degraded by reflections and noise. The two researchers gradually improved their experimentation technique until the three dimensional effect was directly perceivable. With the demonstrations of the first compelling holograms of a toy train in late 1964 the spatial nature of the hologram was unquestionable ([LU64]). Now the development spread by word of mouth and there was no halt for the triumph of holography.

1.1 Preceding works

The concept of holography is nowadays a normal tool in the sciences. The principle is used for different measurement tasks over the complete electromagnetic spectrum (see e.g. [Gat86], [TW81]) and as well in acoustics [YFB02]. Interferometric methods in analog and digital holography are used for example to compare two states of an object, revealing deformation information.

With the development of pulsed lasers it was possible to record dynamic processes and living subjects [Sie68], [Ans70]. Green pulsed lasers are especially suited for skin reproduction, due to the little penetration depth.

In our research initiative conducted at `c ae sa r` (center of advanced european studies and research) we identified analog portrait holography as a candidate for facial topometry. The capture is realized with a short-pulsed green laser, which freezes all movements. It is the key idea to digitize the optically reconstructed real image, which is then used to reconstruct the object surface. The development and improvements to analog holographic topometry was presented in four PhD theses before this dissertation and is documented in many publications.

The first work by Jens Bongartz ([Bon02]) showed that the fast capture is ideal for the measurement of living human faces. In his initial design the real image digitization was performed with a diffusor screen and a CCD camera. His work covers the stationary holographic camera, medical considerations and scattering properties of the skin. The whole recording process from hologram capture, wet chemical processing, optical reconstruction to the surface finding is described. In his work structured stripe illumination was used to enhance the image contrast to detect skin.

Dominik Giel ([Gie03]) introduced speckle illumination for the improvement of the skin contrast. He proposed a multiplexing of the reconstruction beam for a coherent addition of the subimages. Giel discussed inverse filtering and deconvolution for the improvement of the image data. He used mirrors to enlarge the recording aperture. He also performed first test towards digital holography.

Susanne Frey ([Fre05]) used a CMOS flatbed scanner to digitize the real image directly. In this step the diffusor screen was dispensable, which resulted in reduced speckle degradation. The skin contrast was sufficient for the surface detection, no further structured illumination was needed. As an effect the recordings were eyes-safe and the brightness information was used as a pixel precise texture map. Frey proposed a surface refinement, which accounts for the caustic effects of the bright surface spots.

Andrea Thelen ([The06]) focussed on the reconstruction methods and image refinement. The surface detection relies on an evaluation of the local image contrast. Thelen compared 14 contrast measures from literature and derived an optimized operator (Extended Sum Modifies Laplacian) for contrast measure. She used a simulated hologram tomography for the verification of the performance of the different contrast operators. She also proposed an optimized focus determination. For the refinement of the surface she implemented an anisotropic diffusion algorithm.

Some aspects of the technique have been developed in diploma projects. Andrea Thelen [The03] introduced an adaption of the surface detection to account for off-axis effects, Nathalie Ladrière [Lad04] developed an automatic chemical processing, Andreas Zepp [Zep05] showed an aperture extension with analog holograms, Nicola Gisbert [Gis05] registered color photographs with the grayscale texture of the hologram to obtain a colored texture, Stephanie Heintz [Hei06] implemented the algorithms for the numerical reconstruction of digital holograms.

1.2 Scope of this thesis

This thesis documents the latest developments in holographic topometry. Two major topics are presented. Firstly, the digitization procedure of the analog method was substantially enhanced with a novel instrument. The second and significant aspect of this work presents the first successful effort to establish a fully digital variant of holographic topometry. This thesis will provide the foundations of holographic imaging, necessary to appreciate the technological advance.

In chapter 2 the fundamental principles of holography are formulated, with the simultaneous recording of phase and amplitude. The separation of recording and reconstruction is a basic property of holography. The consequential requirements for the recording are provided and the effects of speckle formation and the resulting spatial resolution are discussed. In digital holography the real image is reconstructed numerically utilizing the Fourier transform. Techniques for improving the quality of the reconstruction are presented.

Many efforts have been undertaken to improve the analog holographic topometry. Chapter 3 documents the recent state of the method, describing a new mobile holographic camera and the establishment of an optical reconstruction unit.

Chapter 4 describes the development of a new instrument for the direct scanning of the real image. A novel device using an X-ray flat panel detector brings enormous benefits in terms of precision, speed and dynamics compared to the CMOS flatbed scanner. This innovation effectively improved the reconstruction quality.

Chapter 5 describes the newly developed digital hologram tomography method. A single pulse of a laser is recorded with a CCD camera. The numerical reconstruction algorithms necessary for stack reconstruction of the real image is presented, accompanied by a fast calculation on graphics hardware. A new gauging approach is shown with its implementation. Geometrical corrections of the real image reconstruction are proposed, not yet addressed in literature. With these steps the surface and the texture of small objects is determined. An approach to further improve the axial resolution by synthesizing several views is presented. Skin can already be visualized in the real image.

In chapter 6 two distinct applications for the analog holographic topometry are introduced, which are only possible with the advantages of this method. The first application is the topometry of baby cleft patients, which naturally do move during the recording. With the fast exposure, it is possible for the first time to digitize baby faces. The second application evaluates the gravitational effects on soft tissue. Two recordings of a face, one in upright position and one reclined, are compared to determine the soft tissue shift. The pixel precise texture from the holographic method allows to track features in the face, revealing a real displacement which is larger than the volumetric displacement measurable with textureless data.

Chapter 7 concludes this thesis with a summary of the results. A future perspective of the technique ends this thesis.

Chapter 2

Fundamentals of holography

It is unique to holographic imaging that the phase and amplitude are recorded at the same time without using lenses. The holographic information may be captured with an analog photosensitive plate or electronically with a light sensitive array. All conventional techniques, as photography, record a scene on a photosensitive surface by a projective imaging system (lens). Only the amplitude is registered, information about the relative paths of single contributions gets lost.

In section 2.1 the fundamental equations for holographic image formation will be introduced and consequences for the spatial resolution and speckle formation will be discussed.

The same principles account for digital holography (section 2.2), where the real image may be reconstructed numerically. Here, the Fresnel approximation is emphasized, since it was used exclusively throughout this thesis.

In the reconstructed images the three different diffraction orders overlay and the real image is governed by speckle noise contribution. By appropriate filter methods the quality of the reconstruction may be improved widely.

2.1 Theory of holographic imaging

The holographic information is generated interferometrically by superposition of two coherent beams, a wave scattered from the object and a reference wave. The phase as well as the amplitude information are coded in the resulting fringe pattern. The photographic plate carries the hologram, which bears no resemblance to the original object. The object is inscribed in the hologram in a coded form.

The information of the hologram may be reconstructed by illuminating the plate again with a respective beam. With this procedure the original object wave reconstitutes and the object reappears spatially. To the observer this object is indistinguishable from the original object, only it is monochrome.

2.1.1 Hologram recording

A hologram captures the phase and the amplitude of a wave at the same time. Yet any photographic emulsion or light sensor registers only the intensity, and not the phase of an incident light field. In the formation of the hologram H the object wave O is superimposed with a phase reference R. Provided that these two beams are in a fixed phase relation, i.e. both beams are coherent, the resulting interference pattern carries both, amplitude and phase information.

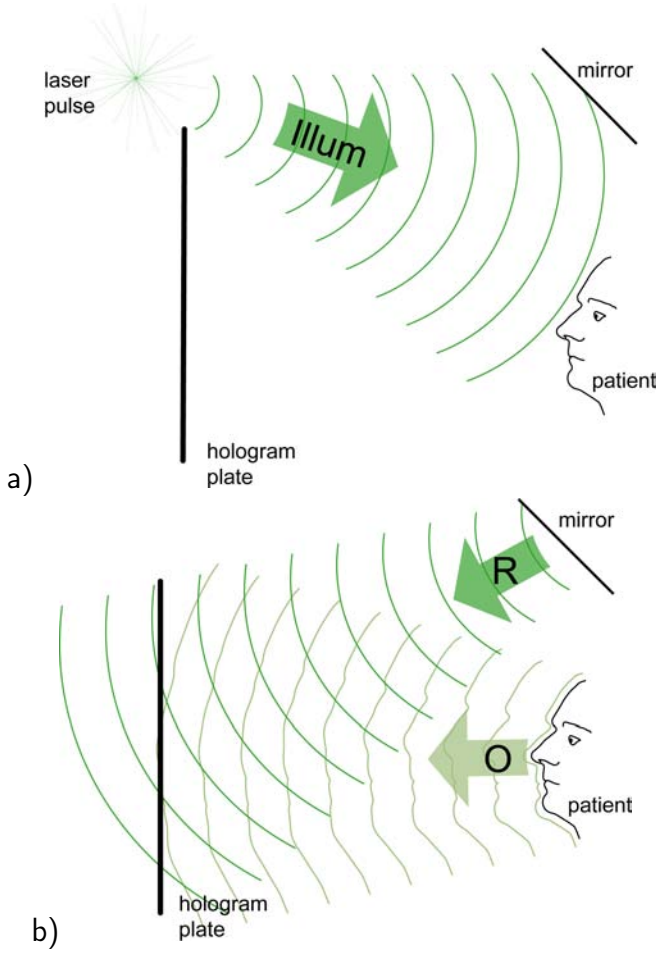

Figure 2.1: Schematic drawing of the hologram recording procedure. a) The initial beam *Illum* partly illuminates the object and partly forms the reference beam. b) The light reflected from the target forms the object beam O. O interferes with the reference beam R on the holographic plate, yielding the hologram H.

Given the light field of the object wave is

$$O(x, y, t) = |O(x, y)| \exp(i\varphi(x, y)) \tag{2.1}$$

with a reference wave:

$$R(x, y, t) = |R(x, y)| \exp(i\varphi(x, y)) \tag{2.2}$$

The intensity of the light field of the hologram H at the point (x, y) is described by:

$$\begin{aligned} I(x, y) &= (H(x, y, t))^2 && (2.3)\\ &= |R(x, y) + O(x, y)|^2 = (R + O)(R + O)^* && (2.4)\\ &= RR^* + OO^* + R^*O + RO^*, && (2.5) \end{aligned}$$

* symbolizes the complex conjugate. The spatial coordinates are omitted for the sake of readability.

So the hologram is the interference pattern between an *object* wave and a *reference* wave.

During the recording process the incoming intensity is converted into a responding signal (optical density, electron charge). The complex transmission factor τ is the fraction between the incident wave E_e and the resulting wave E_t behind the hologram plate.

$$\tau(x,y) = \frac{E_t(x,y)}{E_e(x,y)} \tag{2.6}$$
$$= T(x,y)\exp(i\varphi(x,y)). \tag{2.7}$$

We distinguish two general cases for the transmittance:

φ=const	*amplitude hologram*. Only the optical density of the hologram is modified.
T=const	*phase hologram*. Only the phase is modulated.

Both types of these transmission holograms are used for recording the complete wavefront. In the course of this section only the case of amplitude holograms will be discussed, phase holograms may be treated accordingly. Phase holograms show a higher diffraction efficiency than amplitude holograms and are thus widely used as master holograms.

The exposure B is the entire intensity that reached the plate during the exposure time t_b,

$$B(t) = \int_0^{t_b} I(t)dt. \tag{2.8}$$

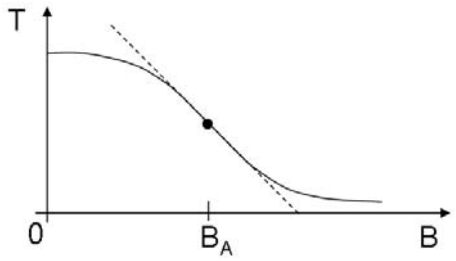

Figure 2.2: Amplitude transmittance of the holographic plate versus exposure B. At the working point B_A the response is approximated as linear.

The mapping between the incident light and the film after development is generally not linear. The emulsions are designed such that the response function is approximately linear in a certain exposure around the working point B_A, as shown in figure 2.2. The real transmittance T is expressed as

$$T = a - mB, \tag{2.9}$$

the constants a and m are specific for each recording medium, but should be constant over the hologram. In digital holography the response is purely linear, the offset a may be neglected.

After exposure and processing the hologram carries the distribution [LK03, p. 102ff]

$$T = a - mt_b\left(RR^* + OO^* + R^*O + RO^*\right). \tag{2.10}$$

2.1.2 Image reconstruction

Now that we have described the recording process of the object wave O, it remains to reconstruct this wave. For reconstruction the hologram is illuminated with a light field $C(x,y)$, modulating the transmittance to give the resulting wave

$$\begin{aligned} A &= CT \\ &= aC - mt_B C\left(RR^* + OO^* + R^*O + RO^*\right) \\ &= \underbrace{\left(a - mt_B\left|R\right|^2\right)C}_{A_0} - mt_B(\underbrace{\left|O\right|^2 C}_{\tilde{A}_0} - \underbrace{R^*OC}_{A_V} - \underbrace{RO^*C}_{A_R}). \end{aligned} \tag{2.11}$$

These four terms in the formation of the image can be identified:

A_0 *Zeroth order diffraction.* The reconstruction wave multiplied with a constant factor.

$\tilde{A}_0$ Broadened *zeroth diffraction* order term, modulated by $|O|^2$. This term is called *halo* sometimes.

A_V *Virtual image.* This term contains the reconstruction of the object wave O, propagating in the initial direction. It can be viewed through the hologram.

A_R *Real image.* The real term contains the complex conjugate object wave O^*, which can be imagined as the time-reversed original object wave O.

Equation 2.11 gives the general case for any reconstruction wave. It is most reasonable to use the complex conjugate reference wave as the reconstruction light field ($C^* = R$). The conjugate for a divergent spherical wave is a convergent spherical wave, resembling the exact time-reversed wave field (see figure 2.3). The reason for this choice is obvious when computing the resulting wave field.

$$\begin{aligned} A &= TR^* \\ &= aR^* - mt_B R^*\left(RR^* + OO^* + R^*O + RO^*\right) \end{aligned} \tag{2.12}$$

The real image term has the form

$$A_R = mt_B\left|R\right|^2 O^*, \tag{2.13}$$

which is proportional to the undistorted complex conjugate object wave O^*. The last term gives the distorted virtual image

$$A_V = mt_B R^* R^* O. \tag{2.14}$$

The real image is a three-dimensional light field, an exact reversal of the object wave, whereas the virtual image is only visible through the hologram by the observer [LK03, p. 104 ff], [EA93, p. 11 ff], [Mei65].

It must be noted that the resulting wavefront is an overlay of the four contributing terms. By a proper design of the reference wave and recording geometry, these terms are suppressed or will spatially not affect the real image. The first order component and the desired real image are spatially well separated in an *off-axis* arrangement, which means that reference wave and object wave include a large angle. This arrangement is common for analog portrait holography. In the digital approach, due to the small recording angle, the various terms overlap and have to be accounted for as discussed in section 5.4.

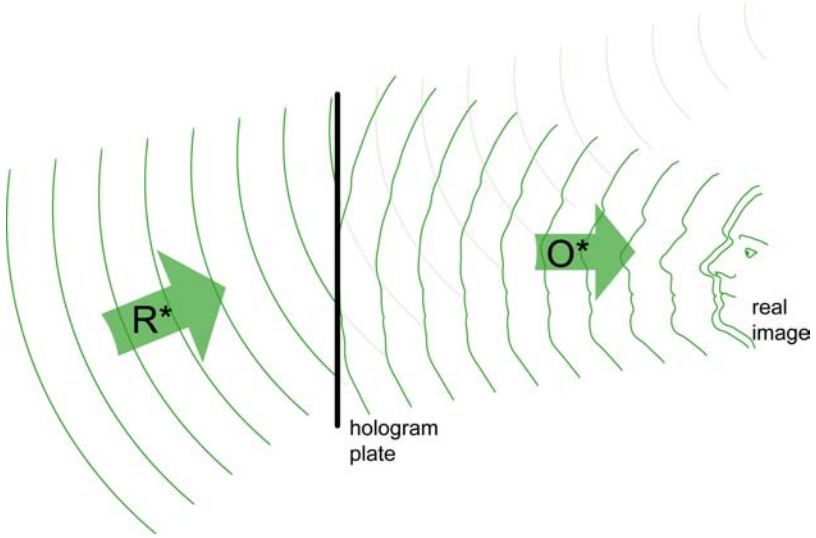

Figure 2.3: A reconstruction with the complex conjugate reference wave R^* generates the conjugate object wave O^*. This time-reversed beam forms the real image.

2.1.3 Spatial frequency resolution

In this section we will dedicate to the superposition of two or more waves: the phenomenon of interference. Each wave $\mathbf{E_i} = \vec{E}_i(\vec{x}) = e_i \exp(i\varphi_i)$ (the temporal term is omitted) contributes to the superposition

$$\mathbf{E_i} = \sum_i \mathbf{E_i}, \tag{2.15}$$

the intensity for a superposition of two waves is

$$\begin{aligned} I &= |\mathbf{E_1} + \mathbf{E_2}|^2 && (2.16)\\ &= (\mathbf{E_1} + \mathbf{E_2})(\mathbf{E_1} + \mathbf{E_2})^* && (2.17)\\ &= {e_1}^2 + {e_2}^2 + 2e_1e_2\cos\Delta\varphi && (2.18) \end{aligned}$$

The resulting distribution consists of the two individual intensities ${e_i}^2$ and the additional interference term $2e_1e_2\cos\Delta\varphi$. This term vanishes for incoherent superposition but for a coherent superposition it is responsible for the fringe pattern formation.

A *constructive interference* establishes where

$$\Delta\varphi = 2n\pi, \tag{2.19}$$

a *destructive interference* requires

$$\Delta\varphi = (2n+1)\pi, \tag{2.20}$$

both for $n = 0,1,2,...$

The spacing of the fringe pattern is determined by the distance from one extreme value to the next. According to figure 2.4 the path difference $\Delta l_1 + \Delta l_2$ has two contributors:

$$\Delta l_1 = d\,\sin\theta_1 \quad , \quad \Delta l_2 = d\,\sin\theta_2. \tag{2.21}$$

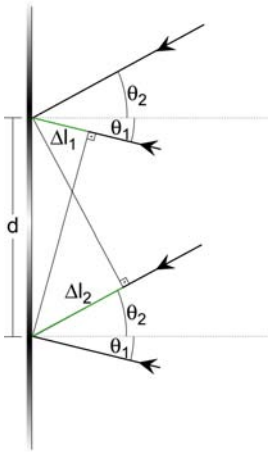

Figure 2.4: The path difference between two extreme values in a distance d for two plane waves is $\Delta l_1 + \Delta l_2$.

The spacing is formed if the path difference equals (multiples of))one wavelength

$$\lambda = d = \Delta l_1 + \Delta l_2. \tag{2.22}$$

With the approximation $\sin\theta_1 + \sin\theta_2 = 2\sin(\frac{\theta}{2})$ we obtain the fringe spacing

$$d = \frac{\lambda}{2\sin\frac{\theta}{2}}. \tag{2.23}$$

The spatial frequency f of the fringe pattern takes the form

$$f = \frac{1}{d} = \frac{2}{\lambda}\sin\frac{\theta}{2}. \tag{2.24}$$

Spatial frequency requirements The interference pattern is formed by the superposition of the object wave with the reference wave. The recording device must be able to resolve this maximal frequency for a given set-up. This concerns the grain size of an emulsion or the pixel spacing for a digital detector.

Shannon-Weavers sampling theorem states that a signal can be recorded unambiguously if it is sampled at least twice in one wavelength

$$\lambda > 2\Delta x. \tag{2.25}$$

This presents the minimal requirement for the pixel spacing. The maximal frequency f, which can be recorded, is called Nyquist frequency f_N,

$$f_N < \frac{1}{2\Delta x}. \tag{2.26}$$

Combining formulae 2.24 and 2.26 we obtain a relationship between the included angle and the resolution of the recording device.

$$\frac{2}{\lambda}\sin\frac{\theta_{max}}{2} = f_N = \frac{1}{2\Delta x}. \tag{2.27}$$

Consequently the maximal angle of inclusion θ_{max} is described as

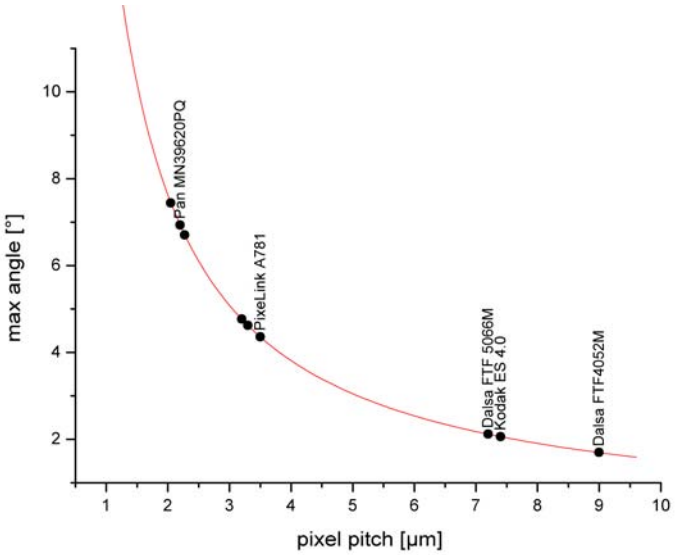

Figure 2.5: Relation between the pixel pitch Δx and the maximal recording angle θ_{max}.

$$\theta_{max} = 2 \arcsin\left(\frac{\lambda}{4\Delta x}\right) \tag{2.28}$$

$$\approx \frac{\lambda}{2\Delta x} \qquad , \sin\theta \approx \theta \text{ for } \theta \ll 10^\circ \ . \tag{2.29}$$

The graph in figure 2.5 shows the functional relation between the sensor pixel pitch and the recording angle. The numbers for the sensors with currently the smallest pixel pitch are denoted. The values for the angle θ_{max} for the sensors used during the investigations are shown in table 2.1.

Camera type	**Sensor**	**pixel pitch [μm]**	**max angle [°]**
PixeLink A781M	FillFactory IBIS4-6600 CMOS	3.5	4.4
Kodak Megaplus ES 4.0	Kodac KAI-4000 CCD	7.4	2.1
Evaluation Kit	DALSA FTF5066M CCD	7.2	2.1

Table 2.1: Pixel spacing and respective maximal angles for the sensors used during this work.

2.1.4 Spatial resolution of the real image

Any imaging optics is limited by diffraction. Consequently one may never focus a beam to a single point, the focus is always a broad distribution. For a simplified calculation, a planar reference beam illuminates a Fresnel zone plate, diffracting the beam to focus on one point ([Rog50]). In this notion the hologram is regarded as a lens.

The extent of the focus point is the theoretical limit for the spatial resolution of a hologram. This distribution is the holographic point spread function (PSF), which in reality is dependent on the position of an object point and many additional factors.

The PSF generally follows a converging cone geometry. At the focus point the distribution deviates from its general cone shape to form a beam waist with a diameter of $2w_0$ (figure 2.6). The derivation of the following two relations may be found in [Sie86, p. 664 ff]. A gaussian beam

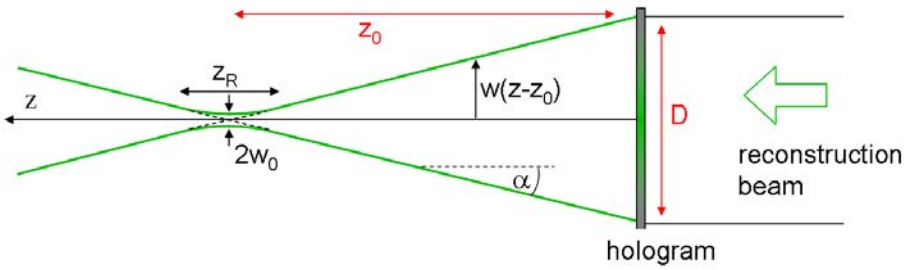

Figure 2.6: The optical reconstruction of a Fresnel zone plate leads to a Gaussian beam profile with a Rayleigh length z_R and a beam waist of $2w_0$.

for illumination results in the half beam waist

$$w_0 \approx \frac{2 \cdot z_0 \cdot \lambda}{\pi \cdot D}. \tag{2.30}$$

This number gives the radius of the Airy disk, the central spot of the diffraction pattern. The axial length of the focus is called Rayleigh length z_R. This number delivers the length in which the beam cross section doubles,

$$z_R \approx \frac{4 \cdot \lambda \cdot z_0^2}{\pi \cdot D^2}. \tag{2.31}$$

The numbers w_0 and z_R can be regarded as the lateral and the axial resolution of the hologram, which are significantly different in analog and digital holography.

	analog Film	**CCD sensor**
λ	532 nm	532 nm
D	20 cm	1.4 cm
z_0	60 cm	60 cm
w_0	1 μm	20 μm
z_R	6 μm	1200 μm

Table 2.2: A comparison between analog film and the digital sensor demonstrates the different spatial resolutions. Only the wavelength of the mobile system is evaluated. The slight difference to the stationary system has little effect on the spatial resolution.

The theoretical limit of resolution for analog holography is in the micrometer range and is mainly due to the large extent of the hologram. In practice the spatial resolution is much less than the theoretical limit. For instance parts of the hologram are occluded by the object itself, an effect called shadowing. In optical reconstruction the reconstruction wavefront never matches the reference wavefront perfectly, which additionally limits the resolution.

The extent of a digital hologram is usually much smaller than in analog holography (table 2.2), here the Kodak camera is compared. The lateral resolution is still in the range of 20 μm which may be seen in reconstructions as well, they reveal a lot of detail (figure 2.7). The axial resolution is significantly lower, it scales proportionally with the sensor area. So an axial resolution of some millimeters can be accomplished. This number is a lot higher than in the analog case, but is, in fact, not far from the requirements for a successful surface reconstruction.

2.1.5 Speckle formation

A grainy pattern results from coherently illuminating a rough surface. The scattered light from the surface fluctuates in space forming a speckle pattern. The speckles form, as the roughness

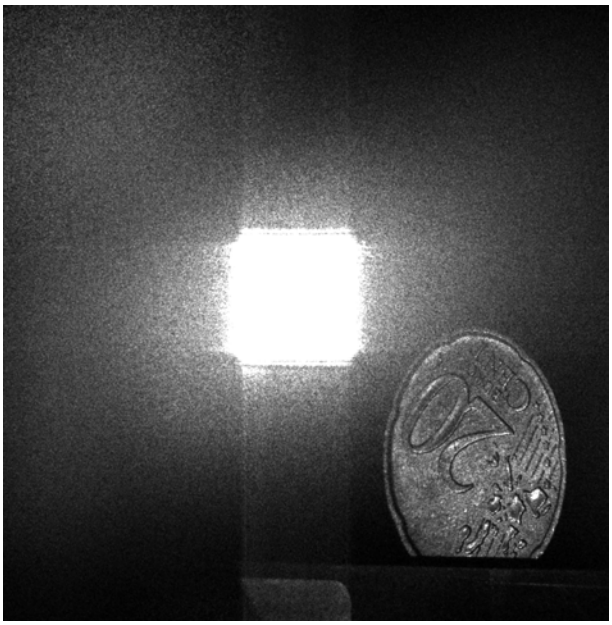

Figure 2.7: In a digital hologram the slices of the numerical reconstruction carry a lot of details. This reconstruction shows a 20 cent coin holographed at a distance of 60 cm. The speckle influence was reduced by a Gaussian smoothing with a range of 2 pixels.

of the surface lies within the order of the wavelength of the illumination.

The elementary scattered waves interfere with each other, forming a stationary spatial pattern. The speckle pattern can be regarded as a unique finger print of a surface, a circumstance utilized for speckle interferometry.

Two forms of speckle formation are distinguished, objective and subjective speckles (figure 2.8). As described above, speckles appear from the reflection on a rough surface, which are objective speckles. When a speckle pattern is viewed through a vision system, which introduces an additional aperture, the speckles are subjective.

For both cases the mean spot size has a characteristic behavior, which is in principle determined by the diffraction limit constituted by the smallest aperture of the complete system.

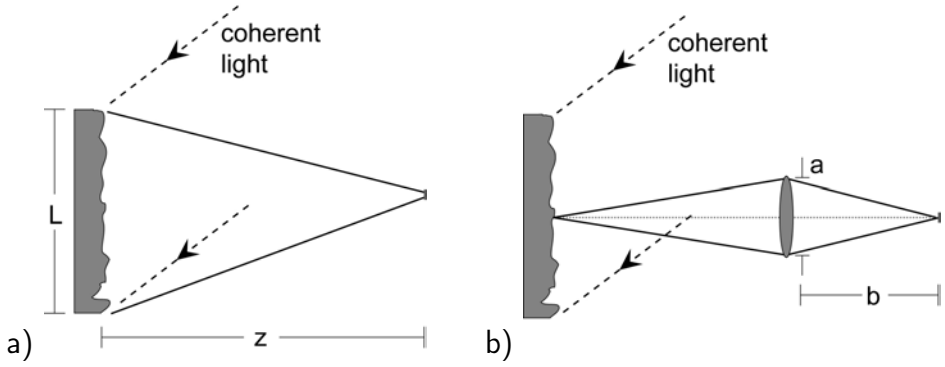

Figure 2.8: The mean speckle size depends a) on the extent L of the object for *objective* speckles and b) on the aperture a and focal length b of the vision system for *subjective* speckles.

Objective speckles For the formation of the objective speckles (figure 2.8 a)) we consider the spatial frequency formula (equation 2.24). Two elementary waves originate from the outer corners of the object, include the angle θ at a distance z. Given this maximal distance L, these

form the highest spatial frequency

$$f_{max} = \frac{2}{\lambda} \sin(\frac{\theta_{max}}{2}) \approx \frac{L}{\lambda z}. \tag{2.32}$$

The wavelength of the resulting fringes provides the mean size of the speckles

$$d_{sp} = \frac{\lambda z}{L}. \tag{2.33}$$

The speckle size increases proportionally with the distance from the origin and depends inversely on the object extent. The object extent forms its own aperture, the same is the case for a hologram. There the speckle formation in the real image can be treated accordingly. The objective speckle size poses the physical limit for the real image formation.

Subjective speckles In the presence of an imaging system, speckle formation is strongly dependent on the limiting aperture. Again, starting from the spatial frequency formula 2.24, this time the vision system with the focal length b introduces the limiting aperture a:

$$f_{max} = \frac{2}{\lambda} \sin(\frac{\theta_{max}}{2}) \approx \frac{a}{\lambda b}. \tag{2.34}$$

The subjective speckle formation (figure 2.8 b)) is the limiting factor for monitoring a coherently lighted object with a camera. This effect can easily be observed by two pictures, which are recorded with a different aperture (figure 2.9). The speckle size decreases with an opening of the iris. Figure 2.9 a) is captured with a small aperture, whereas b) is recorded with a larger aperture.

The images show the author illuminated by the 20 ns laser pulse, in the instance of the hologram capture. The images where taken with a digital video camera SONY XCD-SX910CR, synchronized to the green laser pulse of the mobile holographic system. These images were produced in the course of the diploma thesis of Nicola Gisbert ([Gis05]), who matched color images on the monochromatic texture gained from holographic topometry.

a) 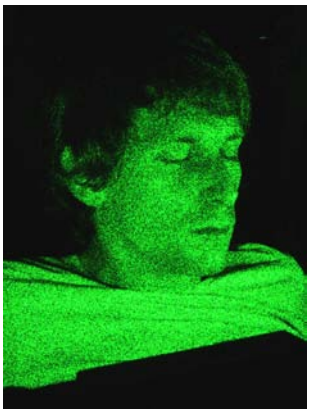 b) 

Figure 2.9: The size of the subjective speckles depends on the aperture of the vision system. a) shows a small aperture, i.e. high *f/stop*, b) is recorded with a wider aperture, i.e. low *f/stop*.

2.2 Methods for digital holography

The basic concept of holography was described above. A reference wave and the object wave superimpose. This interference pattern may be sensed by a photosensitive emulsion or by a light sensitive device. In digital holography the hologram is electronically recorded by a CCD (*C*harged *C*oupled *D*evice) or a CMOS sensor (*C*omplementary *M*etal *O*xide *S*emiconductor).

2.2.1 Numerical reconstruction of digital holograms

In digital holography the reconstruction is realized numerically, and a digital real image appears. The methods for numerical reconstruction of holograms was first described by Schnars ([Sch94], [SJ94]). By evaluation of the diffraction theory one may arrive at compact formulations, which can be effectively implemented in a computer. The method was widely received and led to many developments in metrology.

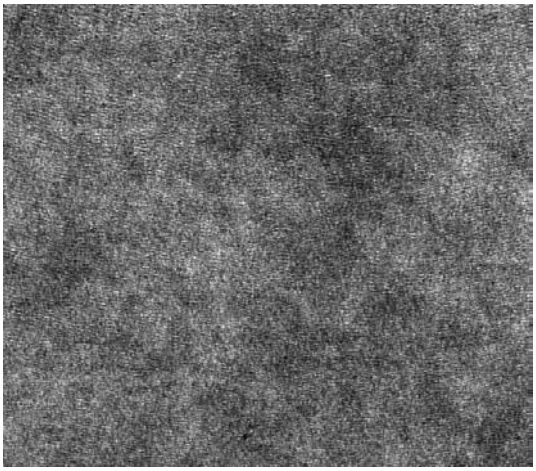

Figure 2.10: A clipping from a digital hologram of a coin recorded with the Kodak Megaplus ES 4.0 CCD camera shows that there is no resemblance between the object and the coded information.

The object is not directly visible in the hologram itself, but exists frequency coded. For a reconstruction of the original light field the hologram is illuminated with the conjugate reference wave (section 2.1.2). For an analog hologram this process is accomplished optically (section 3.2), a digital hologram is reconstructed numerically. The numerical reconstruction is a simulation of the illumination with the reconstruction beam.

In the following chapter the methods for numerical reconstruction of digitally recorded holograms will be laid out.

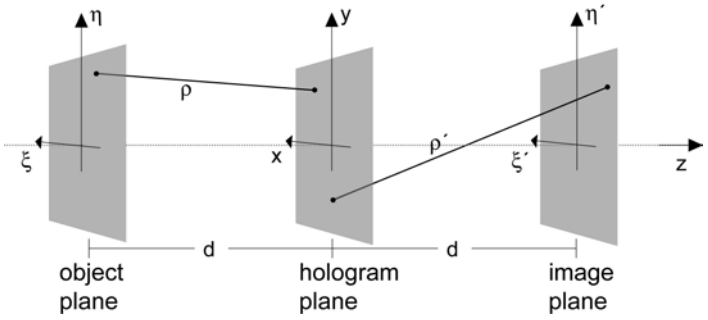

Figure 2.11: Coordinate system for numerical hologram reconstruction (according to [SJ05])

The starting point for the calculation is the *Fresnel-Kirchhoff integral* (Equation 2.35), which

describes the diffraction of a light wave at an aperture, perpendicular to the incoming beam. In this general formulation a hologram is regarded an aperture as well, [KF86, S. 316]. When illuminating a hologram $h(x, y)$ with a reference wave E_R, the resulting light field is

$$\Gamma(\xi', \eta') = \frac{i}{\lambda} \int_{-\infty}^{\infty} \int_{-\infty}^{\infty} h(x, y)\, E_R(x, y)\, \frac{\exp(-i\frac{2\pi}{\lambda}\rho')}{\rho'}\, dxdy \tag{2.35}$$

with

$$\rho' = \sqrt{(x - \xi')^2 + (y - \eta')^2 + d^2}. \tag{2.36}$$

ρ' is the distance between a point in the hologram plane and a point in the reconstruction plane. The geometrical conventions for the coordinates are illustrated in figure 2.11.

The real image reveals in the reconstruction of a hologram when the reference wave E_R is replaced by its complex conjugate $E_R{}^*$ (See equation 2.13 in section 2.1.2). This modifies equation 2.35 to

$$\Gamma(\xi, \eta) = \frac{i}{\lambda} \int_{-\infty}^{\infty} \int_{-\infty}^{\infty} h(x, y)\, E_R{}^*(x, y)\, \frac{exp(-i\frac{2\pi}{\lambda}\rho)}{\rho}\, dxdy \tag{2.37}$$

with

$$\rho = \sqrt{(x - \xi)^2 + (y - \eta)^2 + d^2}. \tag{2.38}$$

The real image emerges where the object resided during recording. The coordinates ρ' have to be replaced by ρ since the reference wave impinges from the opposite side.

Formulae 2.35 and 2.37 are generally not equal, only for a plane reference wave $E_R = E_R*$ is the case. The distance d is a negative value.

The direct computation of the Fresnel-Kirchhoff integral is very time consuming, which is why there are approximations needed. Two common methods are the *Fresnel Approximation* [Kre02b] and the *convolution approach* [Kre02a], both compute with less effort. The Fresnel approximation was used for the numerical reconstructions presented in this thesis. The convolution approach is, in theory, precise, but it requires the introduction of a lens factor. This factor in turn introduces approximations.

Fresnel approximation

If the angle between the points in the object plane ξ and η and the points in the hologram plane x and y are small in respect to the distance d between the planes, the square root in formula 2.38 can be expanded to a Taylor series

$$\rho = d + \frac{(\xi - x)^2}{2d} + \frac{(\eta - y)^2}{2d} - \frac{\left[(\xi - x)^2 + (\eta - y)^2\right]^2}{8d^3} + \dots \tag{2.39}$$

If the forth term is small compared to the wavelength, it may be neglected [KF86]:

$$\frac{\left[(\xi - x)^2 + (\eta - y)^2\right]^2}{8d^3} \ll \lambda, \tag{2.40}$$

and the distance ρ may be reduced to the linear and the quadratic terms:

$$\rho = d + \frac{(\xi - x)^2}{2d} + \frac{(\eta - y)^2}{2d}. \tag{2.41}$$

With the further approximation of the denominator $\rho = d$ in equation 2.37 , which holds true for small angles we attain the following result:

$$\begin{aligned} \Gamma(\xi,\eta) &= \frac{i}{\lambda d}\exp\left(-i\frac{2\pi}{\lambda}d\right)\times \\ &\int_{-\infty}^{\infty}\int_{-\infty}^{\infty} h(x,y)\,{E_R}^*(x,y)\,\exp\left[-i\frac{\pi}{\lambda d}\left((\xi-x)^2+(\eta-y)^2\right)\right]dxdy\,. \end{aligned} \tag{2.42}$$

Carrying out the multiplication under the integral, the factors can be drawn out. This gives the continuous Fresnel approximation:

$$\begin{aligned} \Gamma(\xi,\eta) &= \frac{i}{\lambda d}\exp\left(-i\frac{2\pi}{\lambda}d\right)\exp\left[-i\frac{\pi}{\lambda d}\left(\xi^2+\eta^2\right)\right]\times \\ &\int_{-\infty}^{\infty}\int_{-\infty}^{\infty} h(x,y)\,{E_R}^*(x,y)\,\exp\left[-i\frac{\pi}{\lambda d}\left(x^2+y^2\right)\right]\exp\left[i\frac{2\pi}{\lambda d}\left(x\xi+y\eta\right)\right]dxdy\,. \end{aligned} \tag{2.43}$$

This formula enables the reconstruction of the light field originating from the hologram $h(x, y)$.

In the following the similarity to the Fourier Transform will be pointed out. By a substitution of the factors to

$$\nu = \frac{\eta}{\lambda d} \quad and \quad \mu = \frac{\xi}{\lambda d} \tag{2.44}$$

equation 2.43 simplifies to

$$\begin{aligned} \Gamma(\nu,\mu) &= \frac{i}{\lambda d}\exp\left(-i\frac{2\pi}{\lambda}d\right)\exp\left[-i\pi\lambda d\left(\nu^2+\mu^2\right)\right]\times \\ &\int_{-\infty}^{\infty}\int_{-\infty}^{\infty} h(x,y)\,{E_R}^*(x,y)\,\exp\left[-i\frac{\pi}{\lambda d}\left(x^2+y^2\right)\right]\exp\left[i2\pi\left(x\nu+y\mu\right)\right]dxdy\,. \end{aligned} \tag{2.45}$$

Here the similarity to the continuous Fourier Transform (see Appendix A) becomes obvious. Besides the factor in front of the integral, we detect an inverse Fourier transform $\mathcal{F}^{-1}$ (see equation A.4) of a fuction determined by the reference wave, a phase correction factor and the hologram:

$$\begin{aligned} \Gamma(\nu,\mu) &= \frac{i}{\lambda d}\exp\left(-i\frac{2\pi}{\lambda}d\right)\exp\left[-i\pi\lambda d\left(\nu^2+\mu^2\right)\right]\times \\ &\mathcal{F}^{-1}\left[h(x,y)\,{E_R}^*(x,y)\,\exp\left[-i\frac{\pi}{\lambda d}\left(x^2+y^2\right)\right]\right]\,. \end{aligned} \tag{2.46}$$

This equation describes a continuous signal. The function $\Gamma(\nu, \mu)$ is sampled on a matrix of MxN points as by a CCD sensor, with a stepping of Δx and Δy. These intervals are the dimensions of the individual pixels. The discreet signal expresses as

$$\begin{aligned}\Gamma(m,n) &= \frac{i}{\lambda d}\exp\left(-i\frac{2\pi}{\lambda}d\right)\exp\left[-i\pi\lambda d\left(m^2\Delta\nu^2+n^2\Delta\mu^2\right)\right]\times \\ &\sum_{k=0}^{M-1}\sum_{l=0}^{N-1} h(k,l)\,{E_R}^*(k,l)\,\exp\left[-i\frac{\pi}{\lambda d}\left(k^2\Delta x^2+l^2\Delta y^2\right)\right]\exp\left[i2\pi\left(km\Delta x\Delta\nu+ln\Delta y\Delta\mu\right)\right]\end{aligned} \tag{2.47}$$

for $m = 0, 1, \ldots, M-1$; $n = 0, 1, \ldots, N-1$

The pixel size in the image plane is $\nu = m\Delta\nu$ and $\mu = n\Delta\mu$. It has to be noted that the description of the sampling as realized with a comb function is a simplification, yet for demonstration it is acceptable. In general each value is an integration of the incoming intensity over the pixel extent.

According to [SJ05] the relation for a Fourier transform among Δx, Δy and $\Delta\nu$,$\Delta\mu$ exists:

$$\Delta\nu = \frac{1}{M\Delta x} \qquad \Delta\mu = \frac{1}{N\Delta y}, \tag{2.48}$$

and after re-substitution of

$$\Delta\xi = \frac{\lambda d}{M\Delta x} \qquad \Delta\eta = \frac{\lambda d}{N\Delta y} \tag{2.49}$$

we get the final formulation of the Fresnel approach. With the substitutions of the pixel pitch from formula 2.49 and formula 2.48, equation 2.47 expresses completely in the object plane:

$$\begin{aligned}\Gamma(m,n) &= \frac{i}{\lambda d}\exp\left(-i\frac{2\pi}{\lambda}d\right)\exp\left[-i\pi\lambda d\left(\frac{m^2}{M^2\Delta x^2}+\frac{n^2}{N^2\Delta y^2}\right)\right]\times \\ &\sum_{k=0}^{M-1}\sum_{l=0}^{N-1} h(k,l)\,{E_R}^*(k,l)\,\exp\left[-i\frac{\pi}{\lambda d}\left(k^2\Delta x^2+l^2\Delta y^2\right)\right]\exp\left[i2\pi\left(\frac{km}{M}+\frac{ln}{N}\right)\right].\end{aligned} \tag{2.50}$$

The *intensity* of the light field is

$$I(\xi,\eta) = \left|\Gamma(\xi,\eta)\right|^2. \tag{2.51}$$

The *phase* of the light field is

$$\phi(\xi,\eta) = \arctan\frac{Im\left[\Gamma(\xi,\eta)\right]}{Re\left[\Gamma(\xi,\eta)\right]}. \tag{2.52}$$

With the approximation the *image dimension* is fixed to

$$\Delta x = \frac{d_{obj}\,\lambda}{N\Delta\xi}. \tag{2.53}$$

The hologram may be regarded as an aperture with a dimension of $N\Delta x \times N\Delta x$. A diffraction pattern develops behind the hologram. $\Delta\xi = \lambda d/N\Delta x$ is the radius of the Airy disk or the speckle diameter, which sets the physical limit of the image formation.

The seemingly complicated calculation as outlined above can be reduced to a simple formulation:

$$\Gamma(\xi, \eta) = c_1\{\mathcal{F}^{-1}\,(h\,E_R^*)\,c_2\}. \tag{2.54}$$

This is a complex multiplication of the hologram h with the phase factor c_2 and the conjugate reference wave $E_R{}^*$. The result of this undergoes an inverse Fourier transform. The constant factor c_1 in front of the summation can be neglected.

This formula is applicable for any reference wave. In the case of a spherical reference wave

$$E_R = exp[-i\,\frac{\pi}{\lambda\,d_{ref}}\,(x^2\Delta\xi^2 + y^2\Delta\eta^2)], \tag{2.55}$$

whereas for a plane reference wave it is a constant factor.

This computation is applied to any distance d separately, where only the phase factor differs. The computational effort is linearly dependent on the number of reconstructed slices.

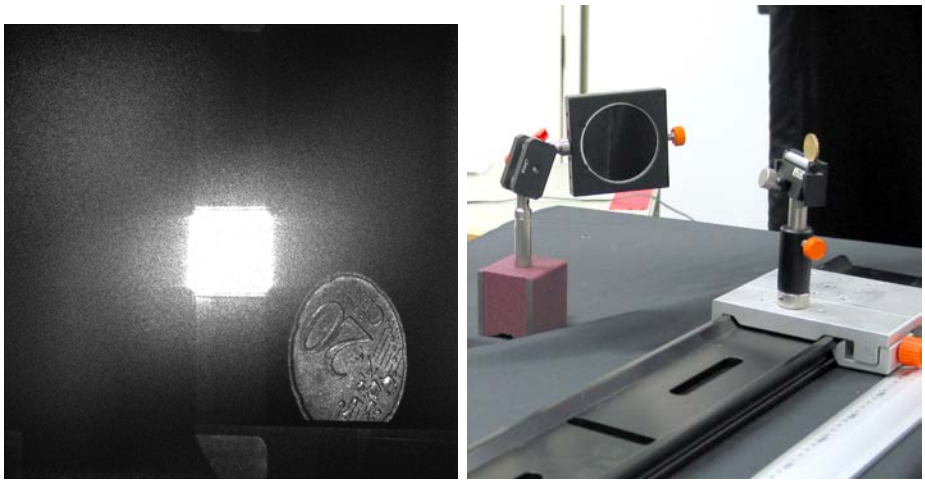

Figure 2.12: Reconstruction of a coin in 60 cm distance from the sensor and a photograph of the original scene.

The calculation of the Discrete Fourier Transform (or its inverse) is well established. The calculation may be optimized tremendously, since many factors appear multiply in the double summation. So by reusing these values the calculation time is reduced from $\mathcal{O}(N^2)$ to $\mathcal{O}(N\,log_2\,N)$, without loss ([BB05, S. 337-339]).

In numerical reconstruction any plane of the real image can be calculated at an arbitrary distance. It is as if one introduces a projection screen in a real image. By successively calculating the slices, the real image is composed digitally. This procedure is coined digital hologram tomography.

Alternative reconstruction methods

The basis for numerical reconstruction of digital holograms is the Fresnel-Kirchhoff integral (equation 2.37). There are different reconstruction techniques than the above mentioned Fresnel approach for retrieving numerical reconstructions of digital holograms. As shown above the Fresnel approach is characterized by the Taylor approximation.

Convolution approach

One very common alternative is the so-called convolution approach ([Kre02a]), which is in principle exact. This sounds promising, yet there is a limitation: it involves an approximation for a

lens. The convolution approach will be sketched very briefly just for the sake of completeness.

The Fresnel-Kirchhoff integral is regarded as a convolution, following the convolution theorem the integral may be separated.

$$\Gamma(\xi,\eta) = \mathcal{F}^{-1}\{\mathcal{F}(h\,E_R{}^*)\,G\} \tag{2.56}$$

with

$$G(n,m) = exp\{-i\frac{2\pi d_{obj}}{\lambda}\sqrt{1-\frac{\lambda^2(n+\frac{N^2\Delta x^2}{2d\lambda})^2}{N^2\Delta x^2}-\frac{\lambda^2(m+\frac{M^2\Delta y^2}{2d\lambda})^2}{M^2\Delta y^2}}\}. \tag{2.57}$$

Opposed to the Fresnel approach, the pixel size is not fixed. The pixel size has to be adjusted with a numerical lens L. The reconstruction is:

$$\Gamma(\xi',\eta') = \mathcal{F}^{-1}\{\mathcal{F}(h\,E_R{}^*\,L)\,G\} \tag{2.58}$$

with a lens formula:

$$L(\xi',\eta') = exp[-\frac{i2\pi}{\lambda}\frac{\xi'^2+\eta'^2}{2f}] \tag{2.59}$$

The only reasonable solution for the lens factor is to confine the imageable area exactly to the respective area from the Fresnel approach. As shown in section 5.4, the information is projected back into the unit cell of the imageable field. After reconstruction the complete field is simply a periodic repetition of the unit cell. If the size of the field is larger, this periodic information is observed. If a smaller field of view is chosen the resolution is limited by the speckles. As shown above, the Fresnel reconstruction describes the physical limit.

We found no benefits in the image quality retrieved from the convolution approach compared to the Fresnel approach. In actual fact the reconstructed images showed more artifacts. Consequently we did not pursue the convolution approach any further, the numerical reconstructions in this thesis were performed exclusively with the Fresnel approach.

Fresnelet reconstruction

One very promising approach was introduced by Liebling ([LBC+02]). Similar to the wavelet analysis he developed an approach where the signal is decomposed into a set of basic functions, the so called Fresnelets. These serve like a basic set of Fresnel zone plates.

Wavelet analysis has many applications in image processing. One major advantage in comparison with the Fourier transform is the adaptability. This multi resolution approach bears the possibility of applying local filters in different neighborhood sizes. Liebling was able to develop an adaptive filtering to reduce the noise and the zeroth order term in the reconstruction without significant information loss. So instead of a global filter, the filter works locally, preserving information in regions where no filtering is required.

[Hei06] evaluated the MATLAB algorithm, which was provided by the developer. We found it to be computationally demanding, and in our evaluation the image quality did not improve significantly. Especially for large images the computation was not possible at all.

The Fresnelet approach is nonetheless interesting because of the adaptive filtering possibilities. For the algorithm there certainly is a lot of potential for speeding up the computation. The results we gained from the Fresnel implementation were satisfactory, so at the current state a stage for a further improved algorithm seems to be unnecessary.

2.2.2 Improvement of the reconstruction quality

Spatial separation

In an in-line or near in-line set-up, the reconstructed image contains the real image (first order diffraction), the virtual image (minus first order diffraction) and the undiffracted reference wave (zeroth order diffraction). Figure 2.13 shows one reconstructed plane without prior image improvements.

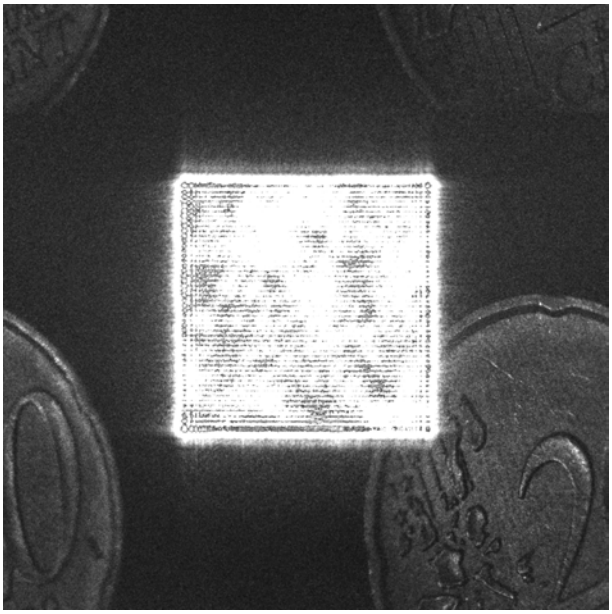

Figure 2.13: The reconstructed image consist of the real image, the virtual image and the undiffracted reference wave. The object distance here is 40 cm.

The real image is in focus, the virtual image out of focus, the zeroth order resides exactly in the center. The digital case can be viewed like the analog scenario. The simulated reference beam illuminates the hologram. Most parts of the beam pass the hologram undiffracted, only multiplied with the hologram pattern. For the analog case the zeroth order is far out of the relevant area, and does not interfere with the real image.

By placing the target out of the regime of the zeroth order (off-axis) the relevant information can be separated spatially (figure 2.14). The unused parts are discarded in the further processing.

The disadvantages are obvious. More than one half of the image information is not used after image reconstruction. The reference beam may be incident with a tilt towards the CCD sensor. If the reconstruction beam is calculated accordingly, the DC-term will not reside in the center but towards the edge of the reconstructed image. This leaves more information undistrrted from the DC-termn and thus enlarges the imageable area noticeably. It is still difficult to retrieve the angle precisely by measuring, a systematic approach seems to be better suited (section 5.3).

DC term suppression

The hologram contains the image information in a coded form as an interference pattern of an object wave with a reference wave. If this information is reconstructed into the original wave field, not only the real image evolves. The disturbing terms of the virtual image the zeroth order and the broadened zeroth are also visible.

The zeroth order (DC-term) comprises of parts of the reference and object beams that pass the hologram without being diffracted ${a_R}^2 + {a_O}^2$ (equation 2.11). The result is a bright distribution

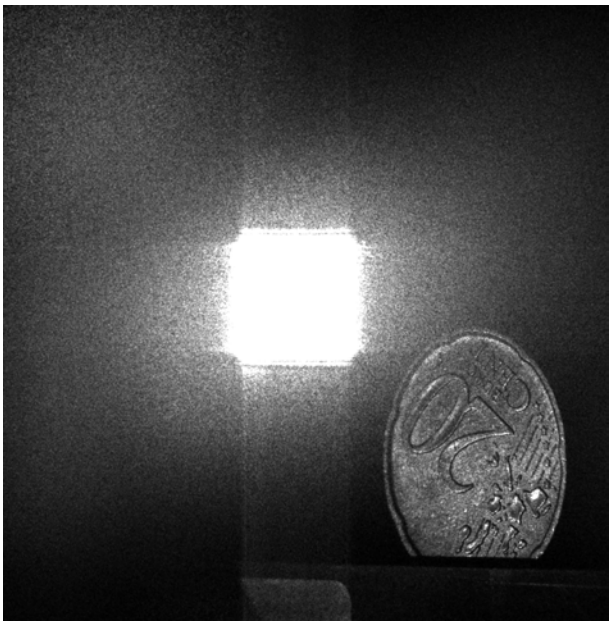

Figure 2.14: By placing the object off-axis in one half of the image, the diffraction orders may be separated spatially.

at the position where the simulated reference beam originates from ${a_R}^2$. By default this is the center of the image, but the reference beam may be simulated with a tilted incidence. ${a_O}^2$ is usually weaker and may be noticed as a halo.

The reconstructed image is disturbed by the overlay of the different diffraction orders. The object beam O and the reference beam R may be measured individually. These parts may be subtracted from the hologram H before reconstruction. This HRO-subtraction method is very effective, but it involves a higher experimental effort since three measurements are needed within a short time interval.

In a pulsed laser system the intensity distribution varies from pulse to pulse. Nonetheless the intensity distribution of the reference beam can be captured separately and subtracted from the hologram. A double measurement of the object, with and without reference beam, is obviously not appropriate because the inherent advantage of the single-pulse measurement would be compromised.

The DC-term is very disturbing, since it covers all relevant information in its proximity. By a carefully considering the positioning of the object, an overlap of the different orders may be avoided. Yet it is desirable to suppress the influence of these unwanted image parts as much as possible([KJ97]).

Mean value subtraction An undiffracted plane reference wave adds a constant intensity to the complete hologram. It would be most desirable to eliminate this contribution from the hologram before the reconstruction.

The contribution of the reference wave can be approximated. In a large distance the spherical reference wave front may be regarded as plane.

$$H_m = \frac{1}{NM} \sum_{x=0}^{N-1} \sum_{y=0}^{M-1} h(x,y) \tag{2.60}$$

By subtracting the mean value H_m from the complete hologram before reconstruction, the influence of the zeroth order may be effectively reduced ([KJ97], [CMD00]), as visible in figure

2.15. The same effect is achieved when two holograms of different random speckle patterns are subtracted ([DMS03]), where the zeroth-order term cancels out.

High Pass Filter Another approach for abandoning the undesired zeroth order is making use of the information distribution in the image.

The undiffracted part of the object wave contains lower frequencies than the one originating from the interference between the waves. So the relevant information is mainly contained in the high frequencies. By applying a high pass filter, the contribution of the low frequencies is eliminated ([SJ05, p. 56/57]). With this measure the zeroth order contribution is widely eliminated.

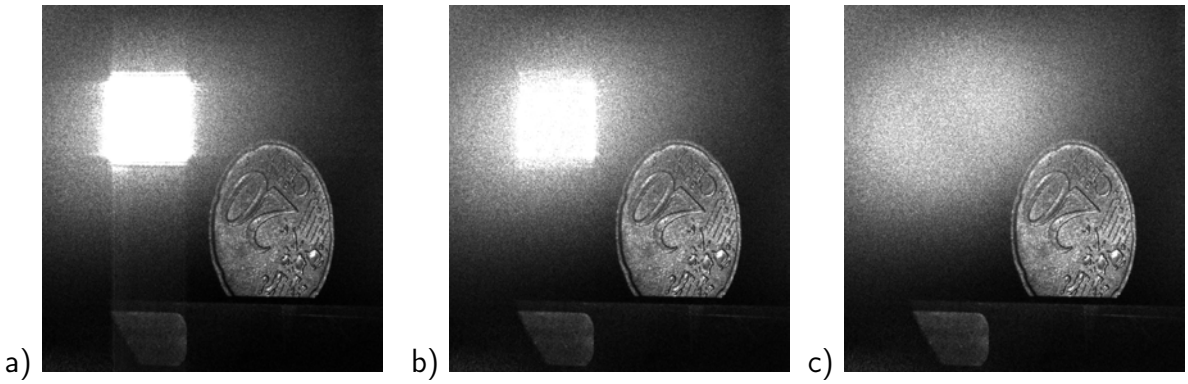

Figure 2.15: Comparison between a reconstruction of an a) unfiltered hologram b) mean value subtraction and c) high-pass filter and mean value subtraction.

There are several methods to implement a high pass filter. Most commonly used is the subtraction of a floating mean from the image realized as a convolution. In this homogeneous shift invariant operation the mean value of a predefined neighborhood (i.e a box function) is subtracted from the point itself. This operation is inappropriate from a signal processing point-of-view since the transfer function (i.e. the fourier transform of the filter function) of the box function takes the form of a sinc-function and is hence not homogeneous ([Jäh02, p. 303]). As a result some image frequencies are amplified unproportionally, deteriorating the image information. Nonetheless the floating mean is widely used in digital holography (eg. [GSRP05]).

A better approach is the smoothing with a Gaussian filter, where the transfer function is as well a Gaussian function. In optics the window smoothing is called apodization ([Goo05, p. 152]). Instead we used an approach in the Fourier domain, where the transformed image is multiplied with a Gaussian window function G for filtering:

$$h' = \mathcal{F}^{-1}\{G\,\mathcal{F}(h)\} \tag{2.61}$$

In the Fourier domain the filter range may be easily varied and optimized. This brings an additional noise suppression opposed to the mean value approach. The resulting images show a nearly complete elimination of the DC-term as demonstrated in the image stack reconstruction in figure 5.7. This optimization was introduced into our reconstruction routine just recently, so not all of the images shown in this thesis gained from this advance.

Compared to the mean value subtraction the high pass filter is accompanied by an information loss. In this aspect the alternative reconstruction method with Fresnelets (see section 2.2.1) should have advantages, where the information loss is only local. As shown in figure 2.15 the mean value subtraction alone does not improve the image quality largely, whereas a combination of a high pass filter with a mean value subtraction eliminates the DC-term contribution effectively.

Speckle reduction

The contribution of speckle formation is noticeable in the reconstructed images, since the mean speckle diameter is only half the diameter of the image resolution. The speckles contribute to the noise in all spatial frequencies.

For a visual inspection the high spatial frequencies are most disturbing. These contributions may be reduced by smoothing with a Gaussian, mean or median filter. We chose the Gaussian filter, the mean is never a proper choice (see above), the median is more appropriate for shot noise.

The purpose of smoothing is an elimination of high spatial frequencies in the images. With this strategy the image is more clearly distinguished from the background noise. But as another consequence, image information is compromised. A smoothing is equivalent to a reduction of the effective resolution in the image.

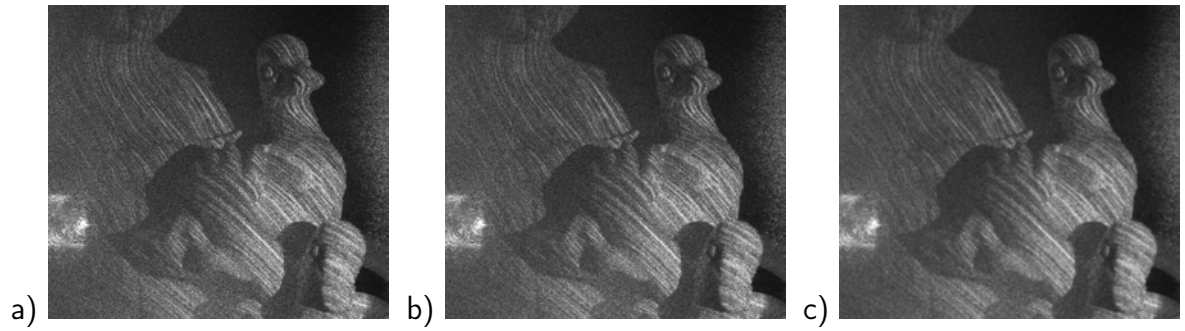

Figure 2.16: Comparison between a) unfiltered hologram and a Gauss filtered reconstruction b) width = 1.0 and c) width = 3.0.

The images shown are usually filtered with a Gaussian of 1.0 - 2.0 pixel width, which visibly improves the image quality. The speckle formation has to be further accounted for, since this noise contribute to the entire spatial frequency spectrum.

2.3 Summary

In this chapter the concept of holographic imaging was outlined. Analog and digital holography share their fundamentals, the same concepts apply for both the analog and the digital holography for the recording and the readout process.

The spatial resolution is directly connected to the hologram extent. Subsequently, the definition for the spatial resolution was delivered. The axial resolution derives from the the Rayleigh length and the lateral resolution may be regarded as the beam waist diameter.

In coherent imaging, speckle contribution always has to be considered since it may not be avoided, the difference between objective and subjective speckle formation is explained.

The Fresnel approximation for the numerical reconstruction of digital holograms was outlined and alternative methods briefly mentioned.

Apart from the physical dimension, the recording material is different in grain size and sensitivity. The grain or pixel size defines the maximal angle at which an interference pattern may be recorded unambiguously.

The small field of view causes an overlap of the different diffraction orders. Despite the limited angle of view the images can be separated spatially. Special filters can be applied to eliminate the unwanted contributions.

Chapter 3

Analog Holographic Topometry

The known methods for object topometry show excellent results for static objects (white-light, photogrammetric, laser scanner) where the acquisition time may be deliberately long ([VR02]). When applying these systems to living persons the performance of these systems drops rapidly, simply because of motion artifacts.

Holographic topometry was especially designed for the digitization of human faces. Due to the short acquisition time, living subjects can be captured without movement artifacts, which overcomes the fundamental shortcoming of all established techniques.

Many aspects of holographic topometry have been described by four previous dissertations. Bongartz established the method for the first time ([Bon02]), Giel introduced speckle illumination and the possibility of mirror setups ([Gie03]), Frey introduced the direct real image scanning ([Fre05]) and Thelen focussed on the improvement of the surface reconstruction algorithms ([The06]).

This chapter introduces the experimental set-up for hologram tomography with an emphasis on the recent developments. The method of analog holographic topometry is a process where the recording and the read-out of the hologram are performed in two separate steps.

The object is captured into a pulsed portrait hologram (section 3.1) using the first mobile camera for daylight capture. The camera is described in detail with the components, pulsed laser, the beam delivery, and the shutter system. After capture, the hologram is processed chemically.

The reconstruction is performed in a separate unit (section 3.2). A new set-up was established to meet the needs for the mobile holographic camera, which involved a design of the reconstruction beam (section 3.2.1) for the reconstruction of the real image. A mismatch of the wavelength from recording laser to the reconstruction laser introduces a wavelength shift.

The real image is digitized slice by slice (see chapter 4), to capture the entire 3D information in an image stack. In a last step, the surface is determined numerically (section 3.3) from the image volume. The resulting digital surface model of the object is visualized as a 3D model (e.g. VRML).

3.1 Analog portrait holography

For holographic imaging we have two recording systems in use in our group. Both are especially designed by *Geola uab* (Lithuania) for producing analog portrait holograms. First we purchased a commercially available holographic camera GP-2J. With this stationary instrument, the hologram plate is placed is made for operation in the dark with red safe-lights. The camera (figure 3.1) consists of a pulsed laser system and the beam forming optics all contained in a housing for safe operation. The laser has a specified output energy of 2 J in the green at 526.5 nm wavelength.

Compared to the continuous wave Nd:YAG reconstruction laser with a wavelength of 532 nm there is a slight shift in wavelength (section 3.2.2). This shift will induce a scaling into the reconstructed real image, which may be corrected numerically.

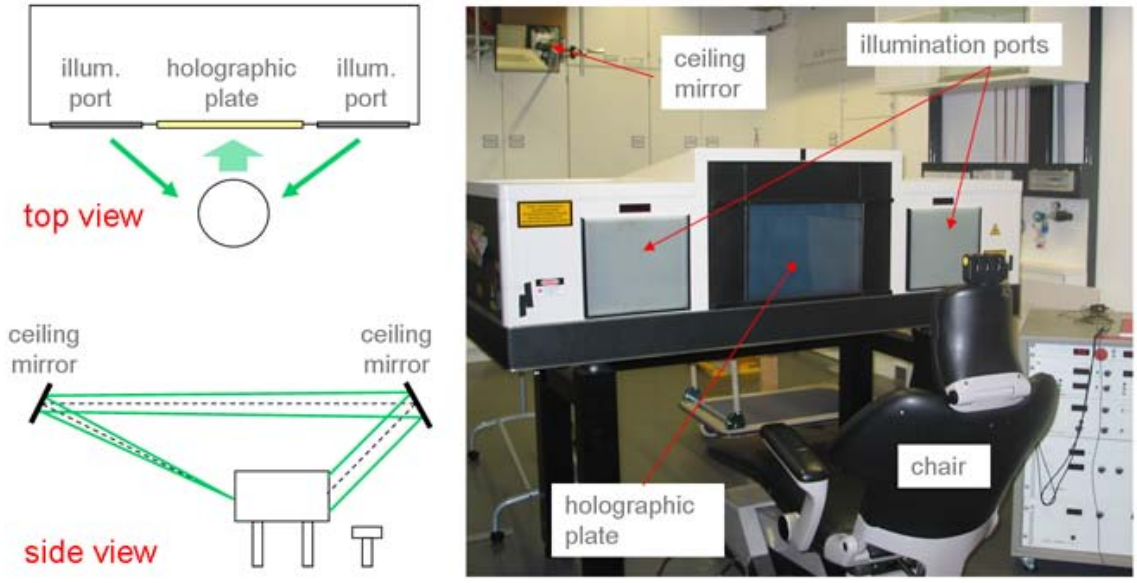

Figure 3.1: The stationary holographic camera. Schematic top view, side view and photograph of the system.

In principle the set-up of the system is very similar to the mobile unit with variations in the beam forming and mirror set-up and the laser construction. The system is described in depth by Bongartz ([Bon02]), where the interested reader can find detailed information.

3.1.1 Mobile holographic camera

A mobile holographic system was custom designed together with *Geola uab*. The HSF-MINI (figure 3.2) camera can be used for in and out of lab applications. With the experiences from the work with the lab system a compact system along with a computer interface was designed. In the course of this work the mobile camera was implemented and refined and so it will be addressed more detailed. The elements of the holographic camera are the Nd:YAG laser, the beam delivery, the shutter system and the control unit.

Compact design

The principal aim of the construction was to develop a system, which can be set up in the field and transported by a station wagon or a little van. The laser and the optical elements for beam forming are mounted on the same breadboard. In this way the area of the breadboard was reduced to half the size.

The reference beam delivery is mounted on the camera case via a rig, so the complete camera can be moved in one piece. This allows for an easy placement of the camera towards a target. The reference beam is a lot shorter compared to the lab system, so the object beam needs less compensation length within the camera housing. The length of the reference beam is approximately 3.60 m measured from the virtual focus of the beam forming optics to the center of the hologram plate. For comparison, the stationary system has a reference beam length of about 9 m, resulting in a flatter wave front at the hologram position.

Figure 3.2: Mobile holographic unit HSF-MINI developed together with *Geola uab* (Lithuania). Here the camera is shown without the diffusor plates for eyes-safe operation. The tower on the right houses (from top to bottom) the control unit, the laser power supply, the amplifier power supply, and the heat exchanger.

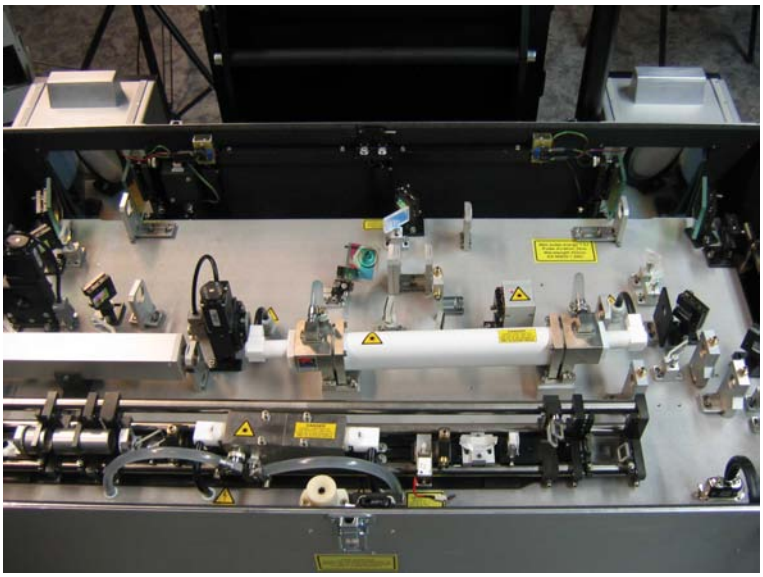

Figure 3.3: Top view of the HSF-MINI camera with the top cover open.

Pulsed single frequency laser

The heart of the holographic camera is a solid state pulse laser system. The stability requirements for portrait holography are described in detail by [Bon02]. A very short laser pulse in the green makes the coherent recording of skin possible. The laser used has a specified coherence length greater than 3 m, so objects within a volume of approximately 3 m x 3 m x 3 m may be recorded.

The laser is a frequency doubled Nd:YAG in an oscillator-amplifier arrangement, optimized for the needs in holography. Especially for the reference beam a clean and reproducible beam is required, a good mode selection of the *TEM00* and frequency stability need are provided.

Both, the flashlamp and the amplification crystal, are liquid cooled with a permanent coolant flow. The heat dissipation is realized by a air-water heat exchanger. The system is mobile, since no connection to external cooling cycle is required.

For the sake of compactness the laser cavity is set up in an invar housing (3 rods) fixed to a breadboard. Figure 3.3 shows the camera from above with the top cover open. The master

oscillator works with a flash lamp pumped Nd:YAG crystal and produces infrared radiation at 1064 nm. In the ring oscillator a saturable absorber functions as a passive Q-switch. The frequency selection is realized by two etalons inside the cavity. A clean transversal beam is guaranteed by a dove prism and an arrangement of a Faraday rotator along with a $\lambda/2$ wave plate. These components are responsible for the wave characteristics of the primary pulse in terms of temporal and spatial coherence, pulse width, and mode and frequency selectivity.

The primary pulse is expanded by a telescope and directed twice through a flash lamp pumped Nd:Glas rod for amplification. After the first pass, the beam is reflected by a phase-conjugating Brillouin mirror and travels back through the rod again. With this measure, impurities in the amplification process are compensated to a great extent. The output energy is controlled indirectly by adjusting the voltage of the pumping flash lamp (1.6 - 2.2 kV). The assignment of the amplifier voltage to a respective output energy is satisfactorily reproducible.

The last step of the pulse generation is the frequency doubling to achieve the visible green radiation. This conversion is realized by a second harmonic generation of a KDP crystal. The resulting pulse has a duration of 20 ns (FWHM) at 532 nm wavelength and delivers a pulse energy of up to 1.4 J in the green. For reasons of heat dissipation in the amplification crystal rod, the repetition rate in *high energy mode* is limited to one pulse per 3 minutes.

For adjustments of the recording set-up or the checking of the illumination, the laser may be operated without amplification, so no heating of the crystal is involved. This *pilot mode* has an adjustable repetition rate of up to 5 Hz, whereas this number is deliberately limited by the manufacturer. For the measurements in digital holography this *pilot mode* was used ($\approx$ 3 mJ). Using this low energy operation, motion series may be captured with a digital hologram capture.

Beam delivery

The second part of the camera is the beam delivery. The beam is diverted inside the camera housing, one part being used for the reference beam, the second part for illumination. The illumination part is again split in two parts and directed to the right and left port. The variable beam splitting is accomplished by a $\lambda/2$ wave plate combined with a thin film polarizer. The wave plate is mounted in a motorized rotation stage. Such, the ratio between reference wave and the illumination beam as well as the port balance are easily adjustable over the software interface (or manually).

The reference wave is focussed on a pinhole with a convex spherical lens (+400 mm). For formation, the beam is diverted by two concave lenses: a spherical lens (-100 mm) and a cylindrical lens (-150 mm). In comparison, the stationary system has only one concave spherical lens for beam forming. This particular optical arrangement of the mobile system forms the reference wave with an elliptical profile. The elliptical profile allows for a confined and rather homogeneous energy distribution at the hologram plate. If the beam forming was realized with a circular profile, a lot of energy would arrive beside the plate and thus would not contribute to the exposure. This optimized beam profile was be accounted for in the reconstruction unit (figure 3.12).

A mirror inside the camera case directs the beam through an aperture on the upper side of the camera housing. The beam arrives at the hologram plate over two external mirrors with increasing size. This overhead reference beam scheme (figure 3.4) leaves enough free space in front of the camera for positioning of the target. At the plate the beam is vertically S-polarized. The angle of incidence onto the plate is chosen to be the Brewster angle. For the transition from air to glass (n = 1.52) the Brewster angle is approximately 57^o. If the Brewster angle was not met, two things would happen. Firstly, light is reflected on the outside glass surface leading to a double interference. Secondly and more severe, the glass plate acts like a Fabry-Perot interferometer, so internal reflections result in a strong interference pattern. This would degrade the object information in the plate. By choosing the Brewster angle for incidence the

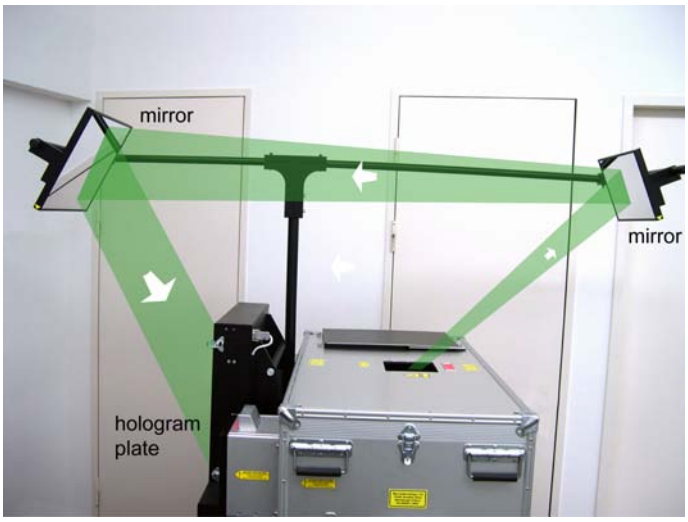

Figure 3.4: Overhead reference beam scheme. The beam leves the camera houing through a hole in the top cover. Over two mirrors the reference beam hits the hologram plate at the Brewster angle.

light passes the hologram plate without self-interference.

The illumination beam is split into two parts, exiting from the right and left port. Before, each part undergoes equivalent forming optics. The beam is expanded with a lens and over 3 mirrors it hits a double sided diffusor plate with a spot size of approximately 20 cm diameter (figure 3.5). A Fresnel lens right before the diffusor reduces the divergence of the distribution eminent from the plate. in this way the illumination is confined to the relevant area.

Like the illumination beams, the reference beam is S-polarized in the vertical direction. This matching is essential, any deviation from a parallel orientation of the polarization may not contribute to the interference. The plate is then exposed but carries no interference information.

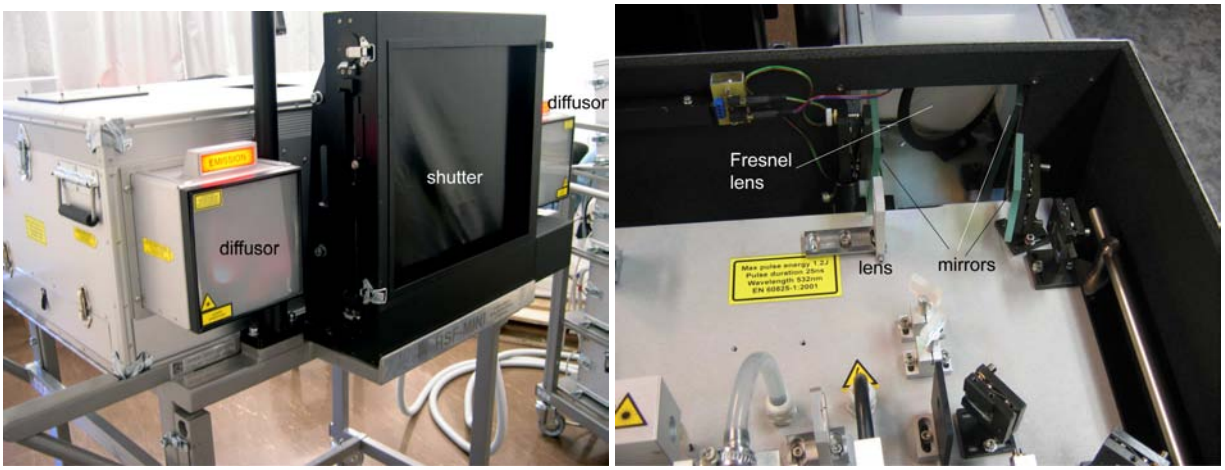

Figure 3.5: Left: The double sided diffusor at one of the illumination port. Right: The Fresnel lens with the following diffusor.

The level of illumination for medical portrait holography complies with the regulations for eye safety ([dFu], [oNI00]). Yet the emulsion demands for a sufficient energy (20 - 40 $\mu J/cm^2$), which is one determining factor for hologram quality.

For eye safety the intensity of the beam at the place of the eye and the spot size are the determining factors. Laser light scattered by a diffusor is treated as an extended light source. The operation software limits the pulse energy to be eyes-safe.

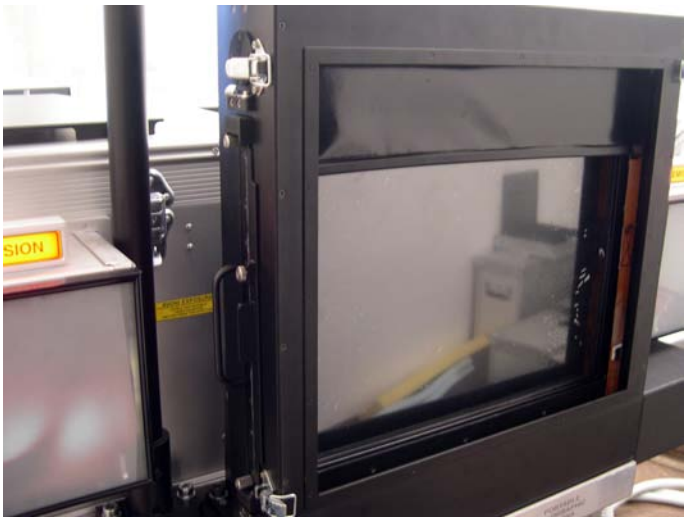

Figure 3.6: The curtain of the shutter exposes the holographic plate. The image shows the state shortly after exposure.

> ! If the energy limitation is exceeded or if the diffusor plates are removed, the recording is not eyes-safe.

Besides the above mentioned light source specifications, the final energy density on the retina depends on the wavelength, the eye geometry and the pupil size. The eye safety calculations assumes the worst case scenario for radiation exposure. This means that the eyes are maximally dilated. It has to be noted that the value for actual eye damage is magnitudes above the official safety limit.

Shutter system

In conventional holography one always has to work in darkness or under safelight conditions. For medical application of the method it is crucial to reduce the irritations for the patient as much as possible. The mobile holographic system features a curtain shutter mechanism that allows to capture holograms in daylight up to an ambient light intensity of about 300 lux (figure 3.6).

When the exposure is triggered, the curtain starts revolving around the hologram plate (figure 3.7). The shutter revolves one time without halting. At the very moment that the entire plate is exposed, the laser sends one pulse and illuminates the hologram plate. The curtain continues its movement until the plate is covered completely again and halts. The curtain needs about 100 ms for one revolution.

The mechanism works as following: For the preparation of the exposure a motor spins up, generating a noticeable noise level. When the motor reaches its desired speed, the camera is ready for exposure. On exposure a clutch couples the curtain with the motor, starting the movement. A sensor detects the moment of maximum opening and triggers the high energy pulse. The shutter maintains its rotation during exposure. After one complete revolution the clutch halts the motor instantly.

As stated above the hologram capture process can be performed completely in daylight. For this purpose a cassette system was developed that allows an introduction of the hologram plate into the camera under normal light.

Therefore the hologram plate resides inside a cassette, which is protected against exposure by a metal sheet. The plate is loaded into the cassette and removed under safelight conditions. For hologram capture the cassette is introduced into the shutter system and the metal cover sheet is retracted. The hologram plate is then protected solely by the shutter curtain. After hologram

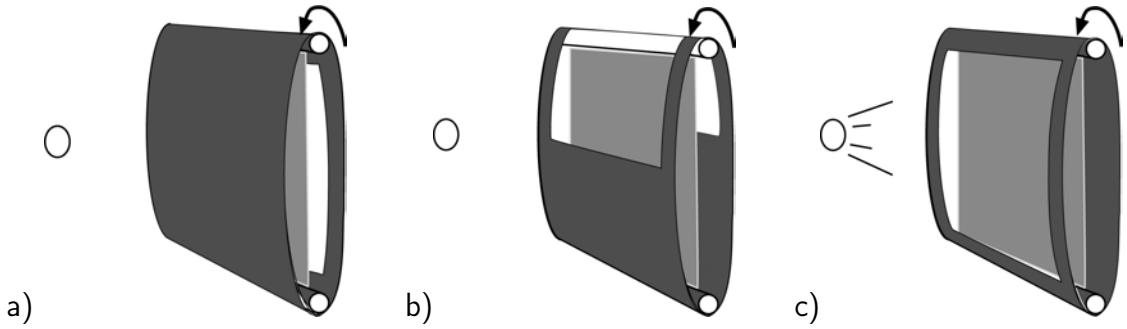

Figure 3.7: The curtain rotates around the holographic plate. a) Closed curtain. b) The curtain starts its rotation. c) The high energy pulse is synchronized to the moment when the shutter exposes the entire plate. The curtain rotates to position a) and halts.

Figure 3.8: Ready for capture. The black shutter curtain covers the hologram plate, so the hologram capture is done in daylight. Left and right are the diffusor plates for eyes-safe recording.

exposure, the metal sheet is inserted again and the cassette can be removed safely. The film handling by the cassette system is similar to the procedure for conventional X-ray processing.

Camera operation

The mobile system is a custom design, operated entirely by a single computer program, developed under the language Lab Windows (Natial Instruments). The computer program runs under the operating system Windows98, as a realtime system is needed. All functions described above are set with a touch screen interface. Complete computer control allows for a simplification of operation and incorporation of safety features but is also prone to malfunction. As a fallback system the camera may be operated manually. So in case of a computer failure the beam adjustments and the exposure trigger can be achieved by technical personnel only.

The operation software was revised several times in the course of this work and finally arrived at a state where operation is safe and functional. The exposure delay time was reduced to approximately 300 ms, which is especially important for the capture of small children (see section 6.1). Now the capture of a hologram is performed by trained, yet nontechnical personnel.

At the system startup all parameters are set automatically. The guidance through the capture process is such that safety steps have to be followed until an exposure is possible. Unnecessary functions are disabled by default and there is an energy threshold for eyes-safe recording implemented.

The standard recording procedure is very simple. As described above, the camera is loaded with a hologram plate. With the initiation of the motor it is ready for exposure. A pulsing sound alerts when the camera is ready for a high energy exposure.

The patient takes a seat in front of the camera, facing towards the shutter system. Height is adjusted in such way that an optimal positioning towards the plate is achieved. The positioning is not very critical, since no focussing optics are involved. The illumination tolerates a reasonable variation in position as well.

The operator monitors the positioning of the patient and triggers the exposure. Choosing the right moment for exposure is usually no problem. Especially for little children it is more challenging, since they naturally move a lot. As shown by the results in this thesis it is nonetheless easily possible to attain good capture results. The hologram capture is instantaneous and the patient may leave right away. The information necessary for the spatial reconstruction is imprinted into the emulsion within the pulse duration on 20 ns. The energy density on the plate during exposure is 20-40 mJ/cm^2.

3.1.2 Chemical processing

The cassette with the exposed hologram plate is transferred to a dark room where the film processed chemically. The processing of the plate is usually performed manually. The plates are coated with the emulsion of the type VRP-M by Slavich ([sla]). It is a silver halide emulsion dispersed in gelatin with a medium grain size of about 40 nm. This equals a resolution of about 3000 lines/mm.

After exposure the hologram carries the so called latent image. From an exposed hologram, both, phase or amplitude hologram, may be generated, which is determined by the chemical processing. Amplitude holograms exhibit a lower diffraction efficiency, since the modulation is realized through absorption in the dark regions. Modulation of the phase holograms offers a higher efficiency in respect to the diffraction of light, but the bleaching procedure introduces additional noise. In the course of this thesis only phase holograms were used.

For a phase hologram the emulsion is processed with the developer SM-6 for 2 minutes, the degree of development is uncritical. After washing the plate from the developer residues for about 2 minutes, the plate is exposed to the bleach PBU-Amidol for 2 minutes until the emulsion is transparent again. As a last step the plate is rinsed of the bleach by water and dried. The optimal chemical processing for the pulsed holograms was described by [Bje95].

Some efforts have been made towards an automation of the development step. For the processing of a holographic emulsion on film, we manipulated a X-ray film developer along with an adaptation of the chemistry ([Lad04], [LFT+04]). Film material is cheaper than glass plates and allows an automated processing, but it is still difficult to attach the film perfectly plane to the suction plate whilst capture and optical reconstruction. Due to this restriction we still favor plates for hologram captures.

SM-6	Sodium Hydroxide 12.0 g, Methyl Phenidone 6.0 g, Ascorbic Acid 18 g, Sodium Phosphate (dibasic) 28.4 g, if 12H2O 71.6 g, water to 1 l

PBU-Amidol Bleach	Potassium Persulphate 10.0 g, Citric Acid 50.0 g, Cupric Bromide 1.0 g, Potassium Bromide 20.0 g Amidol 1.0 g, water to 1 l

3.2 Optical reconstruction

The second step in holographic topometry is the optical reconstruction of the real image. Provided the prerequisite of a conjugate beam is met, a light field emanates from the hologram plate that resembles the object at its original position (real image). A scanner records the object slice by slice, stepping throughout the real image from the tip of the nose up to the auricles. This digitization of the real image yields a 3 dimensional image volume containing the focussed and the unfocussed information.

During this work a new optical reconstruction unit was established, designed for the different geometric requirements of the mobile holographic camera. In the following section the geometric considerations are sketched and the realization of the optical set-up is presented.

3.2.1 Reconstruction beam geometry

As described by theory, the reconstruction beam is supposed to be the exact reversal of the reference beam, i.e. the conjugate reference beam. The shape of the wave front at the place of the holographic plate needs to be reversed. So it is the aim to form a converging spherical wave.

The reconstruction set-up can be regarded as a single convex lens arrangement (figure 3.9), where the lens is equivalent to a spherical/parabolic mirror. A lens with the focal length f is illuminated with a beam originating from the position d_{rek}. The simplification neglects the tilting of the lens.

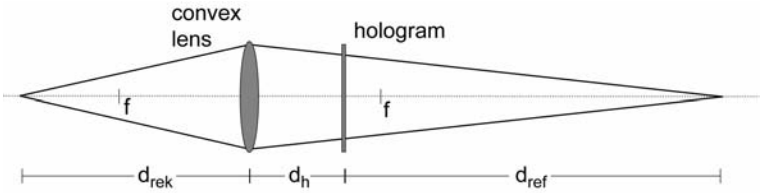

Figure 3.9: A simple model for the hologram reconstruction dimensioning is a single convex lens with the focal length f.

The lens formula gives a simple relation for a given focal length f between the object distance d_g and the image distance d_b:

$$\frac{1}{f} = \frac{1}{d_g} + \frac{1}{d_b}. \tag{3.1}$$

for a reference length d_{ref} and a distance of the hologram d_h the above relation expands to

$$\frac{1}{f} = \frac{1}{d_{rek}} + \frac{1}{d_{ref} + d_h}. \tag{3.2}$$

The length of the of the reconstruction d_{rek} is calculated by:

$$d_{rek} = \frac{1}{\frac{1}{f} - \frac{1}{d_{ref}+d_h}}. \tag{3.3}$$

For a mirror with the focal length of 2 m and a hologram distance of 1 m the result depends on the reference beam length. This value is different for the stationary d_{stat} and the mobile holographic system d_{mob}.

$$d_{stat}(d_{ref} = 8.8\,m) \approx 2.5\,m \tag{3.4}$$
$$d_{mob}(d_{ref} = 3.6\,m) \approx 3.5\,m. \tag{3.5}$$

So compared to the reconstruction unit for the stationary system the length has to be enlarged by 1 m. The new reconstruction unit was constructed so that the reconstruction beam length can be varied by that range to accommodate to the different geometric requirements.

The optics for the beam forming is chosen such that the spherical mirror is widely illuminated. This is achieved by a telescope for beam expansion and a following convex lens. The reconstruction length is measured from the focus behind this convex lens to the mirror.

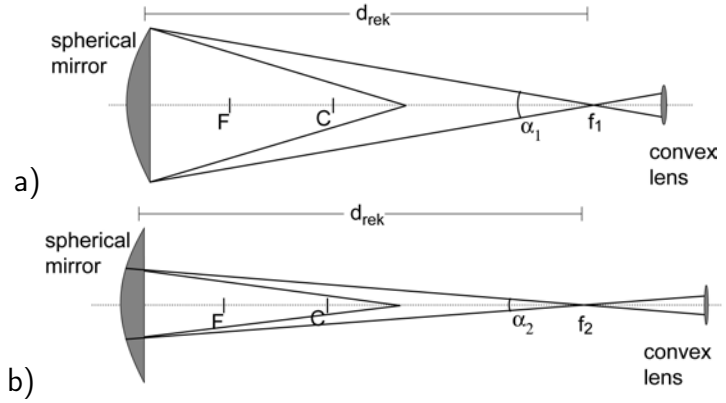

Figure 3.10: The shape of the wave front remains the same at distance d_{ref} for different dimensions of the beam diversion, although the angle of divergence may differ ($\alpha_1 > \alpha_2$). The different focal length ($f_1 < f_2$) from a) short to b) long needs to be accounted for by displacing the lens. The focal length F of the spherical mirror is half the center of curvature C.

The determining factor is the distance d_{ref} between the focus of the beam formation and the hologram plane. The dimension of the beam forming optics in the camera is only responsible for the spatial energy distribution of the reference wave on the hologram plate. It does not influence the shape of the wave front and the angle of convergence α. Given a certain reference path length, the dimension of the diverging optics only determines how much of the mirror/hologram will be illuminated. The beam diversion may be realized with either a convex or a concave lens. Figure 3.10 illustrates the influence of different convex lenses leading to the same wave front.

A strongly diverging optic (figure 3.10 a)) delivers a wider distribution, yet the spherical shape of the wave front will be identical. Only the intensity distribution of the spherical wave front will be different for a different dimension of the diverging lens. The original beam profile is gaussian. In practice the different profile has little influence on the quality of the real image formation.

The geometry above does not account for a tilt of the mirror α towards the beam (figure 3.11), which cannot be avoided due to the spatial requirements. This tilt is accompanied by a cylindrical abberation of the reconstruction beam. The angle between the incident and eminent beams at the mirror is minimized.

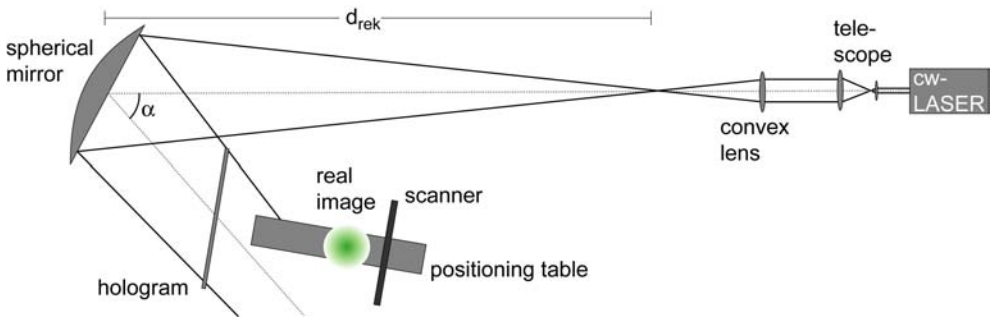

Figure 3.11: The conjugation of the beam is realized with a spherical mirror. The tilt of the mirror α introduces a cylindrical abberation to the reflected beam.

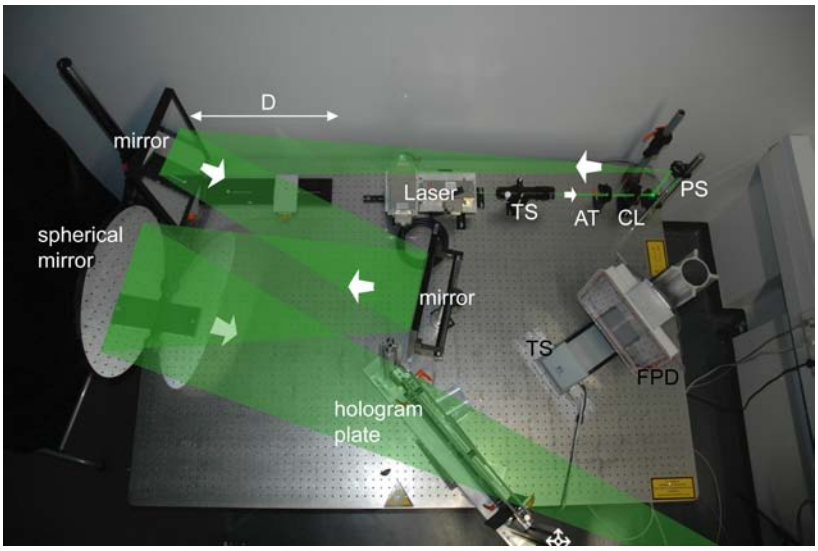

Figure 3.12: Reconstruction set up for the mobile unit seen from above. The beam was folded two times to realize the path on the small optical table. The picture shows the setting for the mobile camera. For the stationary system the mirror on the left may be adjusted by a travel length of D. The path of the beam is sketched, the focus of the reconstruction beam resides approximately 3.6 m behind the hologram plate. Telescope(TL), attenuator (AT), convex lens (CL), periscope(PS), translation stage (TS), and flat panel detector (FPD).

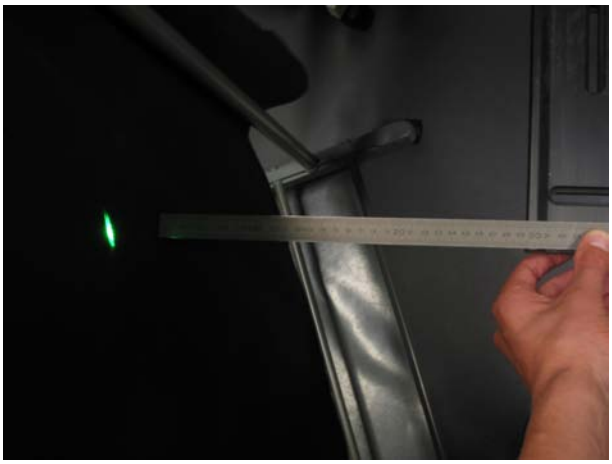

Figure 3.13: The focus resides 3.6 m "behind" the hologram plate showing a shift of about 10 cm, introducing a mild astigmatism in the reconstruction beam.

It was one of the aims to realize the reconstruction on a small optical table. To manage a beam formation on the 1.70 m x 1.20 m small area, the beam had to be folded several times.

The light source is a diode pumped frequency-doubled Nd:Vanadate laser with continuous wave single longitudinal mode operation at a wavelength of 532 nm. The OEM laser of the type Compass 415M from Coherent provides 300 mW laser power. The laser runs on TEM00 with an output beam diameter of 0.3 mm. The temporal coherence has been determined with a Michelson interferometer to be 6 mm. The Coherent Verdi V2 used in the reconstruction unit for the stationary system in comparison has a spectral width of $<$5 MHz. [Fre05] argued that a reduced coherence length will result in a reduced Fresnel zone. Experiments showed that the coherence length of this industrial laser is sufficient for excellent reconstruction results.

Behind the laser the beam is enlarged by 1:10 telescope TL. After an adjustable attenuation (polarizer) AT follows a convex lens CL which is responsible for the primary formation of the beam. The periscope PS brings the beam up to the appropriate height on the optical table. The beam travels once across the optical table to the first deflection mirror. This mirror is mounted to a rail and may be adjusted to account for the different reference path lengths by a travel length of D. After a second deflection the beam impinges on the spherical mirror. There the divergent beam is reflected to form the conjugate reference beam, which is convergent.

The hologram plate is positioned at a fixed distance to the spherical mirror. The hologram plate holder may be adjusted in the position and orientation towards the reconstruction beam. The flat panel detector FPD sits at the site of the real image, mounted to a translation stage TS. The reference beam of the camera is elliptic due to the combination of a cylindrical and spherical lens. In turn, a slight tilt of the spherical mirror is accompanied by a cylindrical abberation. This effect may be utilized to imitate the influence of the cylindrical lens in the reference beam.

Due to the arguments above it is obvious that this introduces a slight shift in reconstruction focus (astigmatism) of about 10 cm, the focus is not axisymmetric. Figure 3.13 shows the focus 3.6 m behind the hologram plate, which mirrors the exact reference geometry.

We used a spherical mirror for this reconstruction unit. This choice is only suitable for the paraxial approximation, to avoid abberations a parabolic mirror should be used instead. Tests showed that this choice indeed reduces the abberations further, yet in the current configuration a spherical mirror performs sufficient. A further discussion of real image aberrations connected with geometric deviations in the reconstruction set-up may be found in [Fre05].

The recording reference beam is a diverging Gaussian beam impinging to the hologram from above. After the formation, the conjugate beam impinges onto the hologram from the opposite direction to that during the recording. The real image appears at the exact position where the illuminated object resided during the recording (figure 3.14). This spatial light field is digitized for the measurement process.

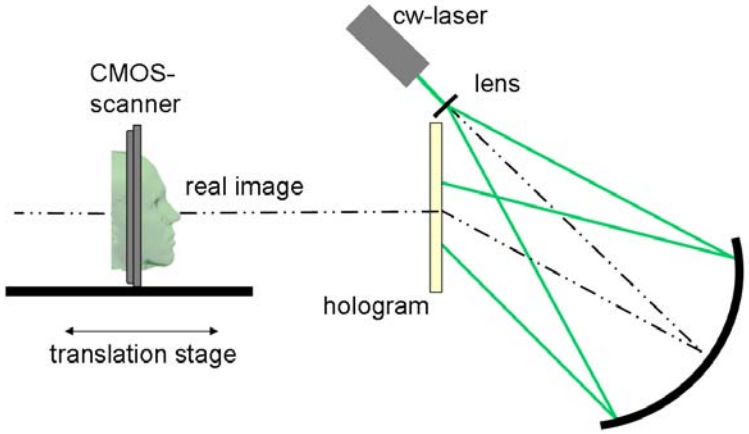

Figure 3.14: Optical reconstruction with the complex conjugate reference beam. The real image appears as a three-dimensional light field at the former position of the recorded object.

During the recording of a hologram the orientation of the plate towards the reference beam can differ by a small tolerance. This circumstance must be accounted for in the optical reconstruction, where the final alignment of the hologram towards the reconstruction beam is done under direct visual control. The criterion for a good reconstruction quality is the absence of any abberations.

An optimally reconstructed real image is difficult to attain under direct eye observation. The fine tuning is best done under real time observation of the real image with a fast scanner (section 4.3). The immediate visual feedback speeds up the alignment process.

It takes a lot of experience to manually align a hologram precisely. A good alignment is crucial to the reconstruction quality: An astigmatism or coma will result in an irregular modulation of found surface result and degrade the surface accuracy. An automatic or semi-automatic system for adjustment would be substantial on the way to an optimal surface quality.

3.2.2 Scaling due to wavelength shift

In theory an exact conjugate reference beam may be tailored by the above geometry. In practice there are circumstances that lead to image distortions. The imaging equations ([Har96]) lead to the lateral magnification M_{lat} and longitudinal magnification M_{long} of the real image for the paraxial approximation

$$M_{lat} = \frac{dx}{dx_{obj}} = \left[1 - z_{obj}\left(\frac{1}{\mu z_{rek}} - \frac{1}{z_{ref}}\right)\right]^{-1}. \tag{3.6}$$

In the paraxial approximation the relation between the longitudinal (axial) and lateral scaling

$$M_{long} = -\frac{{M_{lat}}^2}{\mu} \tag{3.7}$$

is generally not equal. One major source of scaling is a mismatch of the wavelength between the reference beam λ_{ref} and the reconstruction beam λ_{rek} ([Lat71]). The wavelength ratio is

$$\mu = \frac{\lambda_{rek}}{\lambda_{ref}}. \tag{3.8}$$

For the mobile system, both lasers have the same wavelength of 532 nm. The stationary system operates with an amplified Nd:YLF laser at 526.5 nm wavelength, $\mu = 1.0104$. The reconstruction

beam length needs to deviate from the recording set-up by a factor of $d_{reco} = 1.18\, d_{ref}$. Only then an isotropic scaling occurs which can easily be corrected numerically as [Bon02] pointed out. This factor may be verified experimentally by measuring a test target of known dimensions. By comparing the physical dimensions with the dimensions of the reconstructions the deviation may be compensated for.

3.2.3 Digitization of the real image

In the optical reconstruction of a hologram an exact copy of the patient's face is generated. The real image is recorded slice-by slice to give an image stack containing the real image.. Each slice within the stack is a two-dimensional projection at a different axial position within the three dimensional image. This procedure was coined hologram tomography by Bongartz ([Bon02]) alluding to the the scanning process in computer tomography.

There are different possibilities for retrieving each slice. Bongartz and Giel used a diffusor screen and a CCD-camera. Frey realized a scanning directly in the real image with a conventional CMOS flatbed scanner (CanoScan LiDE 60). Within the scope of this thesis a flat panel area detector was implemented, which captures each slice at once. An evaluation of these techniques will be presented in section 4. The axial shift in all three approaches is realized with a linear translation stage that moves the sensor through the real image by a defined stepping (figure 3.14). Depending on the subject of the hologram an inter-slice distance of 0.1 - 1 mm is chosen, where a typical data set consists of 200 - 320 slices. The total number of scans is chosen to be convenient for the further computation steps.

In the process of hologram tomography the continuous information of the real image is converted into a discreet image volume data set. Each slice contains sharp in-focus information and blurred information from out-of-focus regions as in a conventional image. Figure 3.15 shows an exemplary set of slices through the real image at progressing positions.

The first image, shortly before the face, is entirely unfocused. The second tomogram shows a sharp image of the tip of the nose, the third of the eyes, the fourth of temples and the last of the ears. The digitized image volume contains the relevant topological information from the hologram.

Figure 3.15: Exemplary set of tomograms of the real image at different positions. In each slice some regions of the face are imaged sharply, while others are unfocused. The focus progresses from the tip of the nose up to the ears (from left to right).

3.3 Surface extraction

The third step in holographic topometry is the finding of the object surface. In the process of optical reconstruction the light converges from the hologram plate to the focussed points of the real image and diverges again. After digitization of the real image, the object is represented

by focussed points in the image volume. So the digitized volume is an overlay of focussed and unfocussed regions. The task is to discriminate between these contributions numerically.

Focussed regions carry more information in a higher spectral range than unfocussed regions. Hence the local contrast in a small neighborhood will be larger for focussed parts. A mathematical operator measuring image contrast is employed to give a measure for the degree of focus (figure 3.16). This method relies on the fact that the targeted objects show sufficient modulation in their surface.

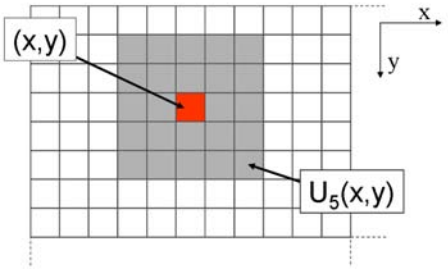

Figure 3.16: Sketch of a local pixel neighborhood $U_5(x, y)$ of the point (x, y) with a size of 5 pixels.

A detailed discussion about different focus operators can be found in [The06]. In this work a Extended Sum-Modified Laplacian operator (XSML) shows the best performance for extracting the focus information of the real image. The presented operator is an optimization of the Sum Modified Laplacian (SML) proposed in [NN94]. This technique uses the second order derivative as high pass filter before the summation is performed. Pixel variance is another well established method [Gie03],[Die02]. A comparison of several operator may be found at [ST98].

The XSML or SML operators are generally used during this thesis for generation of surface data. The focus operator delivers a value $F_{xy}(z)$ at each point (x, y) and each tomogram with the position z. Figure 3.17 shows one slice of a typical scan (a) and the corresponding focus values (b). Regions in focus produce higher focus values than unfocused regions.

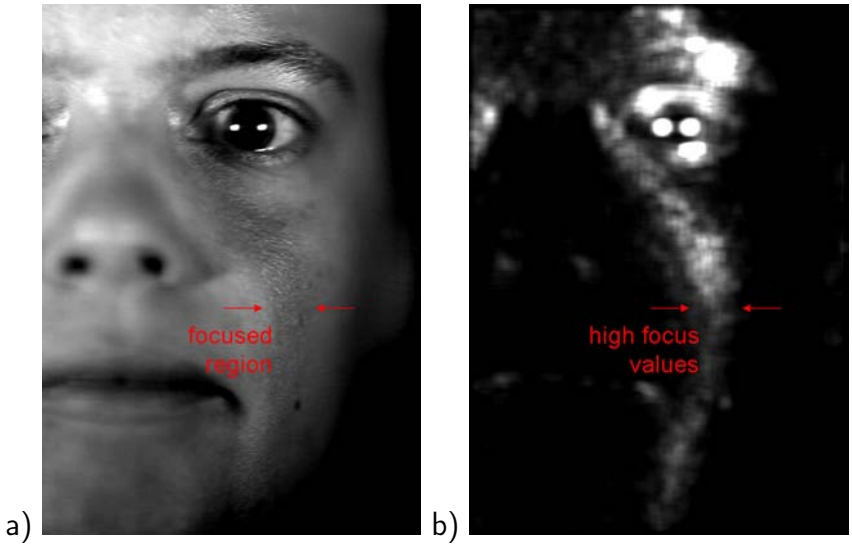

Figure 3.17: a) One slice of a typical scan shows clear focus profile, which is clearly extracted by b) the focus value. White corresponds to high contrast values, black to low contrast values.

For the extraction of the object surface the maximum of the focus measure along the z-axis is searched for. For every lateral point in the image plane a corresponding z-coordinate is expected. In this 2.5d approach undercuts are unaccounted for. A typical depth profile of the focus value is depicted in figure 3.18.

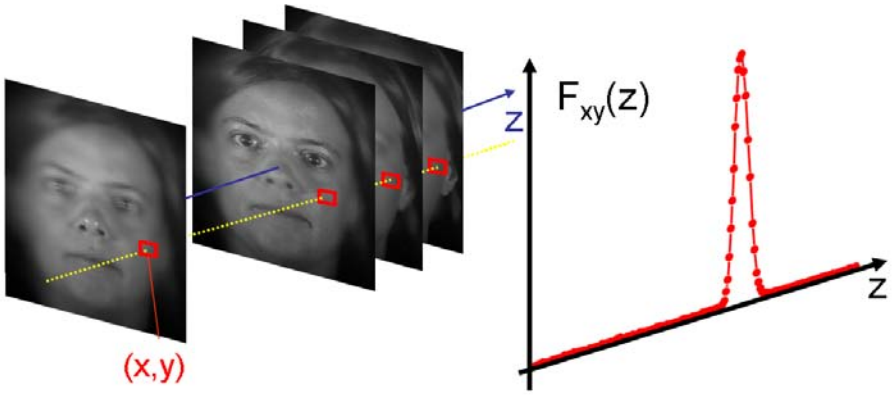

Figure 3.18: For each lateral point (x, y), the focus values $F_{xy}(z)$ are maximized, which delivers the desired z-coordinate.

The extracted depth information forms the height map, which assigns one height value to each pixel. The height value represents the slice, in which the contour resides. In this thesis the height maps are coded by gray values, low numbers are dark colors (front) and higher numbers are light (back). The height map is a parallel projected surface.

The z-value is used to extract the according intensity information from the image volume. These values are combined into one image, which is the parallel projection of the surface image with unlimited depth of sharpness (figure 3.19). In the course of this work it is named *texture image*. The pixel-to-pixel correspondence, which is inherent to the described process, makes any further registration procedure between the model and the texture expendable. The texture image and the height map are combined into the final digital computer model. The illumination during recording is monochromatic, so there is only one color represented as a gray scale value..

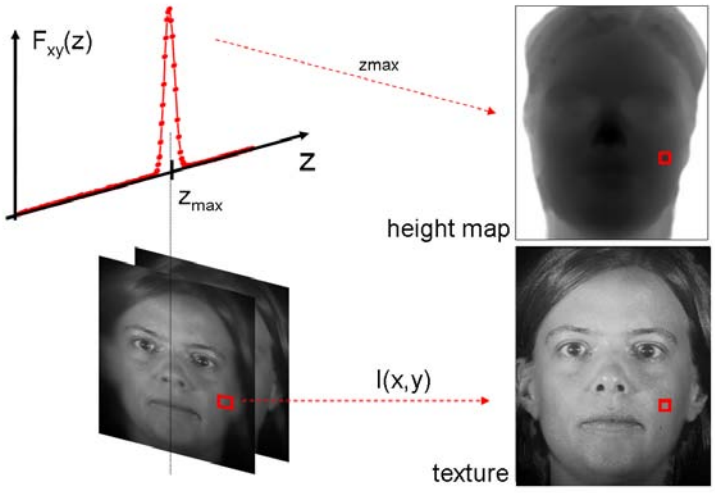

Figure 3.19: Simultaneous extraction of the height information of the face and the corresponding texture.

3.3.1 Surface visualization

The gained digital surface models are coded with the Virtual Reality Modelling Language (VRML). This graphical file format allows an interactive display of textured surfaces in three dimensional scenes. VRML is intended to be a universal exchange format for multimedia and is used in a variety of application areas such as engineering and scientific visualization [VRM97].

A VRML-file can be displayed by any program that conforms to the VRML-standard. There are several versions of the standard and also the format did not show the unifying force that it was meant to have. So individual viewers extend the standard, whilst others do not conform completely. We found the internet browser plug-in *blaxxun Contact* Plugin[1] performed sufficiently according to our requirements.

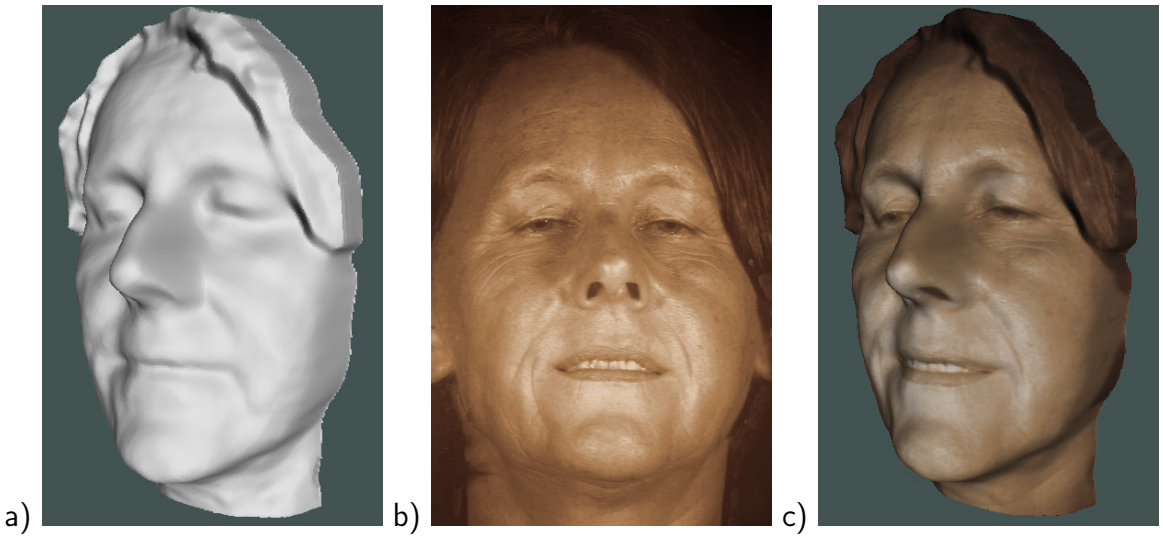

Figure 3.20: The VRML modell combines the surface data a) with the precisely fitting texture file b) to form the final digital model c).

A VRML-file is a plain text file. It provides the viewer with information about the illumination and the viewing position. Following the objects are described and specific interaction scripts are introduced. We code the topometry as a set of three-dimensional points (x, y, z), where the neighboring points are connected to form a trigonal model. The texture image is mapped precisely on the object surface (figure 3.20). For a more pleasant appearance, this gray scale image is sometimes dyed with one color. The node positions are projected into the texture image coordinate system. These projected node coordinates are also written into the VRML-file so that the texture is positioned correctly in the resulting model. Figure 3.21 shows a textured model gained from hologram tomography. The view was rendered with the ray tracing software *Deep Exploration* (Right Hemisphere).

The display of surface data set via a VRML viewer is far from optimal as the visualization of the 3d content is influenced widely by the software. Different VRML viewers may display the same file differently and the display of each viewer can be customized to some extent. The information is denoted as a readable ascii file without any compression, so VRML-files tend to get very large in size and are not encrypted. At the loading process the file is parsed, so it takes an unnecessarily long time to interpret. To enable a reasonable performance for the models the number of lateral surface points is reduced significantly by a number of 4 in each direction. An additional drawback is, that the color dynamics is restricted to 8 bit, which does not account for the improved scanning dynamics. A file viewer, which supports the interactive adjustment of the dynamics parameters, would be most helpful.

Although the VRML format has its drawbacks, there are no other generalized exchange formats for 3D available that support height and texture information at the same time. For internal use we usually write a proprietary file format *.pts* which can be interpreted directly by the 3D program *RapidForm*, the software we routinely use for processing and evaluation of scan data.

[1] http://www.blaxxun.com

Figure 3.21: Screenshot of a textured digital model dyed in light brown. The real image scan of this example is realized with a conventional flatbed scanner.

3.4 Summary

This chapter gave a short introduction to analog hologram topometry. It explains the method from the recording of a pulsed hologram to the textured digital computer model. A new mobile holographic camera is presented that is able to capture holograms in daylight. The camera is compact and features a rolling curtain shutter system to block the unwanted ambient light. An optical reconstruction unit was developed, especially designed for the different recording geometry of this system.

The real image is reconstructed in natural scale, since no wavelength shift is present. This image is then digitized slice-by-slice with a flat panel detector, which travels through the real image. From the image volume the object surface is extracted numerically. This is realized by discriminating the focussed regions from the unfocussed parts with a contrast operator. The surface position along with the texture information is extracted from the real image.

The texture and the height map are combined into a digital computer model. A short introduction to the visualization of the resulting three-dimensional computer models was given.

Chapter 4

Advanced real image digitization

The direct scanning of the real image is accompanied by new possibilities for holographic topometry. With this approach was possible to produce textured digital face models from eyes-safe recordings.

It is one aim of this thesis to further improve the strategy for the digitization of the real image. In the course of identifying a new digitizing technique many shortcomings in the conventional set-up were identified and eliminated.

In section 4.1 the former digitizing techniques are presented, a digital camera and a CMOS flatbed scanner. Although the direct real image scanning introduced many advantages the digitizing suffered from severe shortcomings. At first a new stabilized scanner was built (section 4.2 to overcome the instability but it revealed that a new approach to digitizing was necessary.

The sensor design based on a flat panel detector (section 4.3) is a absolute novelty, which was especially developed for the digitization needs of hologram tomography. Besides the fast data provision, this innovation is accompanied by enormous implications for the complete technology. For the first time it is possible to reconstruct holograms from young children.

4.1 Previous digitizers

Two generations of digitization techniques were used to scan the real image before this thesis. The first implied an indirect imaging of a projection on a diffusor screen, where a digital video camera captured the slices. The second approach was a commercial flatbed scanner that scanned the slice directly in the real image. In this way it was possible to generate textured face models of eyes-safe recordings. Although the quality of the scan allowed a successful reconstruction the CMOS scanner suffered from severe artifacts and has several shortcomings in speed, dynamical range and mechanical stability.

4.1.1 Digital camera

The first indirect digitizing solution applied in the project used a digital camera observing the real image on a diffusor screen. A high-resolution camera (Kodak Megaplus ES 4.0) was focussed on a diffusor screen using a normal camera lens. The camera was shifted with the diffusor screen and recorded the real image of the hologram projected on a diffusor screen ([Bon02]) slice by slice.

The system was fast, but suffered strongly from the influences of the diffusor screen. The screen showed significant directional behavior. An imaging system involving a lens naturally suffers from geometric distortions and the magnification has to be determined. With the use of

coherent illumination additionally subjective speckles appear (see section 2.1.5) which dominated the image structure.

A lot of efforts were taken to overcome these effects like introducing a wobbling motor on the optical desk, or the so-called MUPEGA method for incoherently adding single sub holograms ([Gie03]).

4.1.2 Commercial flatbed scanner

The next step was to record the real image directly in the light field. With the abandoning of the diffusor screen one main source of image degradation was eliminated. The effects of subjective speckle error and brightness falloff due to the scattering characteristics of the diffusor prevented a progress in surface quality. A conventional flatbed scanner was identified to be ideal for digitization ([Fre05]). But only contact scanners are capable of recording the light field directly.[1]

A CMOS flatbed scanner features a scan line that is as wide as the document itself. No limiting aperture is involved and no subjective speckles may form. The main part of the scanner is the CIS (Contact Image sensor) module. This unit contains a CMOS scan line, a self-focussing lens array (selfoc) and an LED illumination. The scanning is realized by travelling the CIS over the document with steady speed. Between the sensor and the document a rod lens array line, usually called selfoc lens, projects the image onto the sensor. The selfoc lens has a sharply defined focus on the document. This leaves enough space for an LED illumination applied from the side.

A direct scan of the real image involves no magnifying imaging optics. The scan is a one to one representation of the scanned object and preserves the exact dimensions of the object. A further scaling of the image is not needed.

After one scan a translation stage shifts the sensor axially by one step and the scanning starts again. Thus the real image is digitized slice-by-slice.

The CMOS scanner frequently used in the project is the Canon LiDE60 (or its predecessors). This A4 scanner can deliver 600 dpi images, which is the optical limit of the CMOS line and has a USB2.0 data transfer.

4.1.3 Improvements through direct scanning techniques

The direct scanning of the real image was a huge step forward for the quality of the digitization. The quality of the slices was so good that the structured illumination could be abolished. With this principle it was now possible to evaluate eyes-safe holograms with diffuse illumination. The surface information and the texture information was extracted simultaneously ([Fre05]), resulting in textured images.

The scanned images are flat and no geometric distortions are apparent (within the tolerances of a low-cost product). By reducing the abberations in the optical reconstruction highly resolved images were attained.

Nonetheless the surface reconstruction was not ideal. It was the next step to identify error sources of the CMOS-scanner and further improve the principle of direct real image digitizing. A CMOS-scanner displays the typical shortcomings:

- speed

[1] CCD scanners in turn, usually features a lens, which focusses the scan field on a small sensor. Although the sensors are available in a higher sensor quality, this scanner type is not applicable. The lenses, i.e. its aperture, result in additional speckle patterns and a longer focus length. A CCD sensor line is usually only 2-3 cm wide with a resolution of 4000 - 8000 dpi. An additional optical system is needed to project the focal plane on to the sensor. The necessary optics is the reason why a CCD sensor is generally more bulky then a CMOS sensor.

- dynamic range
- artifacts
- stability

Speed The scanning of one slice needs between 25 s and 60 s (depending on the scan resolution of 150 dpi - 600 dpi). The typical time needed for digitizing 256 slices of the real image is between 1.5 h and 3h. The alignment of the hologram plate is performed manually. By iteratively tuning the orientation of the hologram plate an optimal placement may be achieved. A fine adjustment requires the visual feedback from the scanned image. This process is hampered by the slow speed of the scanning.

Dynamic Range The image quality of a CMOS scanner is naturally very poor. Gray scale images may be scanned with 8 bit resolution which equals 48,2 dB. The gain and offset vary widely over the CMOS line, making a radiometric calibration indispensable. The noise level of the scanners is additionally very high 2-3 bit, so an effective dynamic range of 30-36 dB seems reasonable. Needless to say that it is impossible to cover the dynamic range of a hologram.

Mechanical stability A consumer CMOS scanner is built to rest on a table top (some may be placed on the side as well). The CIS module is transported with a winch. The starting position of the module varies. This results in a noticeable shiver of the scanned image. Additionally the module may wobble while scanning due to mechanical tolerances. Although the imaged area is generally flat, there are distortions due to the misalignment of the sensor segments and the shiver of the scan line. The fixation rig of the scanner with the translation stage was not satisfactory. The tolerance in positioning resulted in images with irreproducible geometric skew.

Artifacts As shown by [Fre05] the scanners suffer from severe artifacts due to the selfoc lens array. The digitized real image was smoothed by a box function in order to reduce these artifacts. A second drawback is the reduced field-of-view of the scanner due to the selfoc lens. To counter this, the scanner had to be aligned parallel to the hologram plate. Information further off-axis from the selfoc lens is invisible. A CMOS line array consists of several individual small segments, that are glued together. An A4 sensor typically consists of 27 butted segments. At the transitions defects occur, and additionally the alignment accuracy of the individual segments is questionable (see figure 4.2).

4.2 Stabilized 2-axes scanner

It was the first goal to eliminate the mechanical stability issues and image artifacts. A first test with a removal of the selfoc lens revealed that the image artifacts vanish. As a prototype we built a CMOS scanner with a 400 dpi CMOS line camera (Eureca GmbH, Köln) having an array length of 8 cm (figure 4.1 a)). This scan line has a variable integration time (1-10 ms), so it may be adjusted to different light intensities. No selfoc lens was used.

The working principle is similar to that of a conventional scanner. To scan one slice of the real image, the CMOS sensor shifts perpendicular to the sensor line in the lateral image plane with a precision translation stage (figure 4.1 b)). The velocity of the translation is adjusted to produce a geometrically correct image. A second stage shifts the sensor axially. Such the real image is digitized slice-by-slice. Two translation stages from Physik Instrumente (PI) served for the precision shifting of the sensor line.

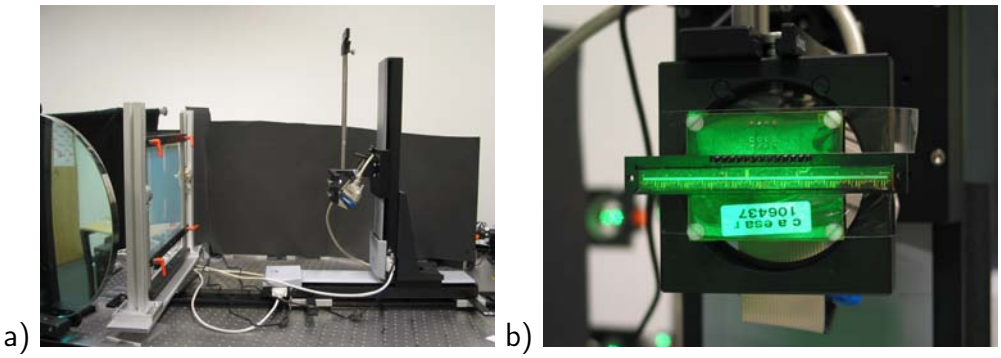

Figure 4.1: a) The CMOS camera is mounted on two translation stages to perform a scanning along two axes. b) Closeup of the CMOS camera.

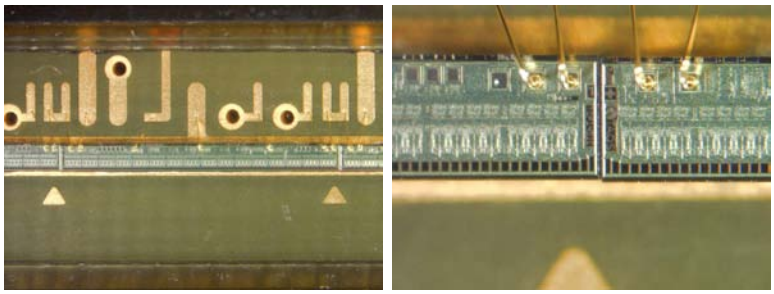

Figure 4.2: A CMOS scan line from an A4 document scanner is composed of 27 single butted lines. At the line borders several pixels are lost. Under a microscope the alignment variations of the CMOS line are clearly visible.

The self constructed CMOS scanner showed that good mechanical stability will effectively improve the surface finding. The absence of the rod lens array additionally removed the image artifacts completely. A good resolution was maintained since less smoothing had to be applied after the scanning process. The scanning speed was comparable to the commercial CMOS scanner, which is still too slow.

The described system shares the general shortcomings of a CMOS device concerning dynamics and linearity. One property of a CMOS sensor is the high noise level. Additionally the individual pixels show a wide variation in gain and offset. In the image presented in figure 4.3 the intensity information of the CMOS sensor was corrected by a linear radiometric calibration. In this case a dark image and a light image are captured and for each pixel the gain and offset can be calculated. Without this correction the images are not useable for reconstruction.

There are CMOS lines with up to 1200 dpi resolution available (21 μm pixel size), that would improve the given set-up in terms of theoretical resolution. A A4 scan line usually consists of about 27 individual CMOS segments that are butted side by side. There is a tolerance in the alignment of about 50 μm and furthermore, at the line between the individual segments there is usually a gap of 100 μm (figure 4.2). This space is partly replaced by sensor elements that are jolted in size towards the end. Although the information is physically lacking there are at least no missing lines in the scanned image.

A new design was considerably faster than the described system. A rate of 1000 lines/s could be attained at a line width of A3. With this set-up the scanning time is reduced to 5 s per image at a resolution of 600 dpi. The further development of this system was stopped when the superior performance of the flat panel digitizer was clear. The only advantage compared to the system presented below is the increase in resolution by a factor of 3.

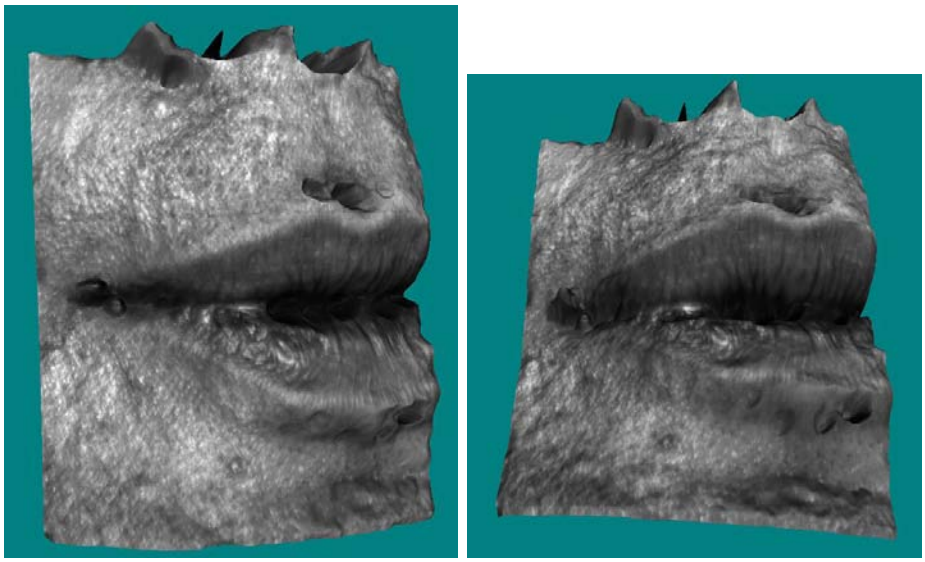

Figure 4.3: VRML-model generated from a real image digitization with the stabilized CMOS scanner

4.3 High performance digitizing

A novel technique for a direct digitization of the real image was developed in this thesis. An area sensor was custom designed, capable of capturing each slice at once, improving the system performance tremendously.

The sensor used, is a flat panel detector based on the PaxScan 2520V by *Varian*. The resolution of this X-ray sensor is 200 dpi which equals a square pixel size of 127 μm. The effective size of the active area is roughly 25 cm x 20 cm, the total number of pixels is 1920 x 1536.

4.3.1 Customization of the flat panel detector

There are no monolithic optical detectors commercially available with a large size. An large-sized X-ray flat panel detector (FPD) was identified as a candidate for the digitizing task. In the booming digital radiography market, these compact panels replace the conventional film systems, cumputed radiography cassette systems, and CCD cameras. These systems are exclusively designed for X-ray use and are not available for the optical spectrum. In collaboration with the manufacturer a detector was developed that was able to manage the optical sensing task.

Optical sensing The flat panel digital X-ray detectors are divided into two basic types: direct conversion detectors and indirect conversion detectors.[2]

We used an indirect conversion type, where the light sensitive sensor has its maximal sensitivity between the wavelength of 500 nm - 530 nm. The scintillator responsible for the conversion of X-ray to light was abolished, which yielded a sensor perfectly suited to the wavelength of the green reconstruction laser.

Surface modification The surface of the substrate shows height variations of several micrometer, which result in severe artifacts in the scanned image (figure 4.4). This phenomenon

[2]The direct sensors convert the radiation directly into a electric charge using amorphous selenium as a substrate. In the indirect detectors a scintillator first converts the X-rays into visible radiation, which is then detected. The most common scintillator materials are cesium iodide and gadolinium oxysulfide. The manufacturing technology is similar to TFT displays production.

does not appear in X-ray capture, only with coherent monochromatic illumination the pattern is visible. The variations are introduced in manufacture, a protective coating was identified as the source. A sensor was produced with less height variations, the coating was omitted in the waver production. After these modifications, the digitized images were free of artifacts.

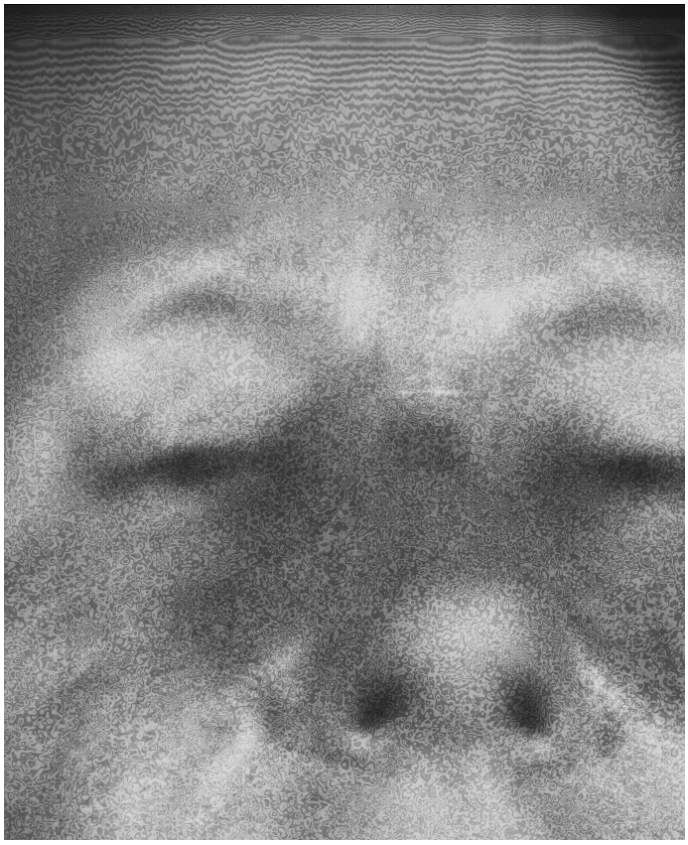

Figure 4.4: Due to height variations of the substrate the flat panel detector shows strong image artifacts. This artifact was eliminated by reducing the height tolerance in the manufacture process.

For protection against environmental influences the sensor substrate is covered by a transparent acrylic glass plate. The capture is unsensitive to minor scratches of the cover glass, since the sensor resides about 1.5 cm below.

4.3.2 Advances from high performance digitizing

The introduction of the flat panel detector for real image scanning brought many advantages to the holographic topometry method. Besides a more convenient use, many issues were resolved that compromised the surface quality before.

Speed

The system operates at a frame rate of up to 10 Hz. The digitization of a complete stack (256 slices) takes only 25 s which is equivalent to a speedup of about 300 times compared to the CMOS scanner, which needed about 2 hours. The panel is shifted axially through the real image by a translation stage. Opposed to the other scanning approaches the panel moves through the real image at a constant velocity. This avoids unwanted vibrations of the hologram, caused by the abrupt acceleration and deceleration of the translation stage. We eliminated this error source by positioning the sensor in front of the desired position and accelerating it in a 3 s pre-feed before the digitizing starts. During the constant movement (typically 1 - 10 mm/s) through the real

image no vibrations occur. The inter-slice distance is adjusted by the ratio between the velocity and the frame rate (1 - 10 Hz). While digitizing the sensor is "free-running" with the internal clocking of the sensor. A first inspection showed no deviations from the timing specifications of the manufacturer, so all slices show a constant spacing.

With the on-line image display the alignment process can now be performed under direct monitoring of the real image. This option facilitates the alignment procedure and results in an additional speedup of the complete digitizing procedure.

Dynamical range

The new detector has a grayscale range of 12 bit with little noise equivalent distortio, which equals a dynamic range of 65 - 72 dB. The sensitivity of the device may be additionally adjusted to account for different intensity needs. Skin pores and highlights are covered at the same time.

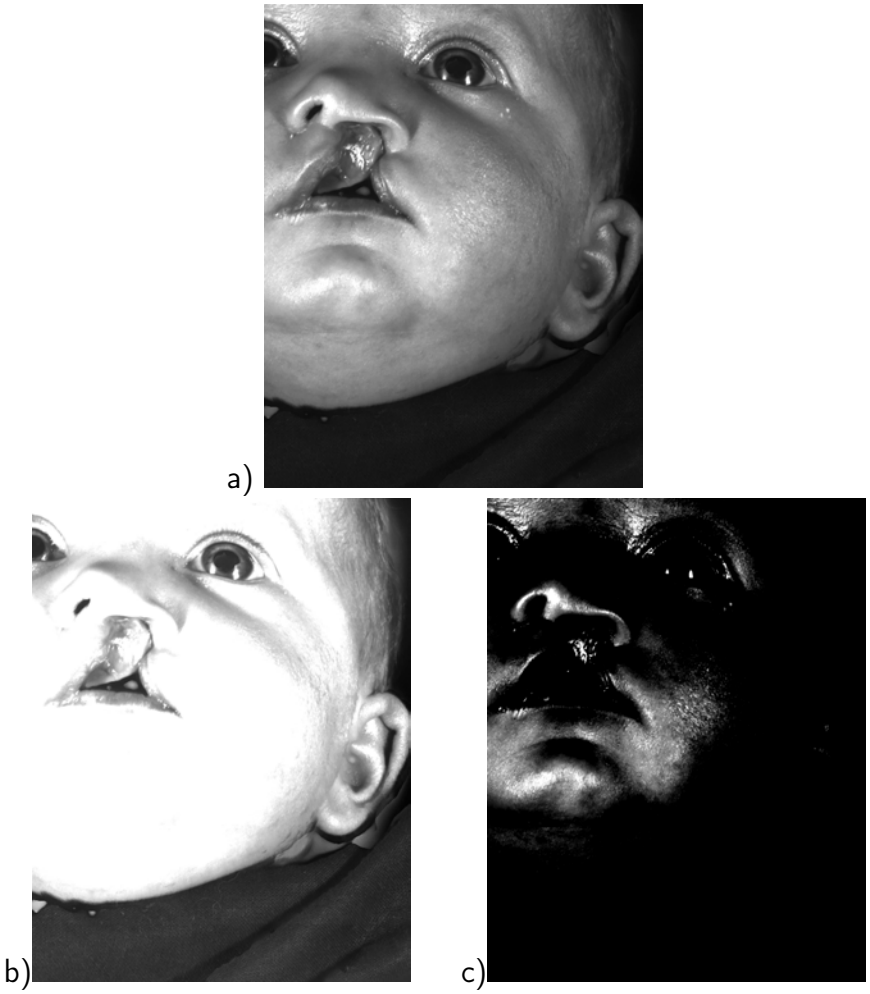

Figure 4.5: These three images display the same information, only the color range is adjusted differently. a) shows the a texture image covering the complete dynamic range. In b) the dark parts are shown. c) shows the variation in the lightest image parts. The image is the entirely focussed texture image, which underlies the VRML model from figure 4.7.

The texture information has now a grayscale range of 12 bit resolution. These values cannot be seen on a normal monitor, which only provides 8 bit per color depth. In digital radiology it is usual to use *window* (contrast) and *level* (offset) for the display of X-ray data on a monitor. Only a part of the 12 bit information is mapped to the 8 bit range, which may be visualized by a monitor. Figure 4.5 illustrates the influence of the displayed contrast window. A specialized viewer with

dynamic color depth is needed to leverage the full potential of the texture information.

As discussed earlier (see section 3.3), the determination of the surface in the real image is realized by a local focus measure. The focus measure need to be robust against noise contributions. There are several sources of noise in the digitized image. One contribution is speckle formation, which becomes dominant for high resolution scans ($\Delta x \leq 50\mu$m). The other determining factor is detector noise.

As pointed out by [The06] the quality of the focus detection is strongly influenced by noise. The high noise equivalent of the CMOS scanner is compensated by a smoothing of the image content. An implicit smoothing is applied by increasing the neighborhood size in the focus finding, which improves the robustness against noise at the cost of an effective reduction of resolution.

The dynamics of the FPD allows to visualize very dark regions along with highlights. Due to the low noise equivalent even small variations in image intensity are detected. The quality enhancement for optimal holograms is noticeable, the surface can be found reliably even in regions with little image contrast.

Figure 4.7 shows four perspectives on a textured VRML model gained from hologram tomography of a baby cleft patient discussed in section 6.1. The views were rendered with the ray tracing software *Deep Exploration* (Right Hemisphere). Due to the high dynamics of the digitized image, even subtle variations in the cloth can be detected. It is possible to realize a model from the tip of the nose up to the ears.

For the first time, holograms of infant faces can be digitized and reconstructed. For a demonstration of the application see section 6.1. The new method allows a fast and reliable digitization with a high dynamic. Even holograms with very low contrast may still be used for the reconstruction. The hologram quality is less critical for reconstruction quality than it was with the older techniques.

Mechanical stability

The sensor is fixed ruggedly to the translation stage (see figure 4.6). The sensor area is now perpendicular to the translation axis. The height of the detector may be adapted to different positions of the real image. The portrait orientation is needed for some recording set-ups, so the detector may be rotated easily by 90 degrees.

The detector position and alignment is stable during its travel through the real image. The shivering of the real image, as induced by the mechanical tolerances of the previous CMOS-scanner does not occur. The solid construction of the area sensor excludes any variations due to unwanted wobbling and misalignment of the scan line. The flatness of the area sensor prevents geometric distortions.

The new digitizer has a resolution of 200 dpi (i.e.127 μm pixel size) which is nominally lower than the 600 dpi ($\equiv 42$ μm pixel size) of the CMOS scanner. The images from the CMOS-scanner suffer from the wobbling of the scan head, which introduces unnoticeable local irregularities. As a consequence the scanned images show local misalignment. Although the image appears to be highly resolved, the surface finding is limited by this degradation.

The perpendicular arrangements eliminated the error introduced by the tilt of the CMOS scanner. As a result well-aligned image stacks are generated, with no internal skew. The models gained an undistorted geometry from this improvement. This prerequisite enabled an accurate study of the gravitational effect on the facial appearance (see section 6.2).

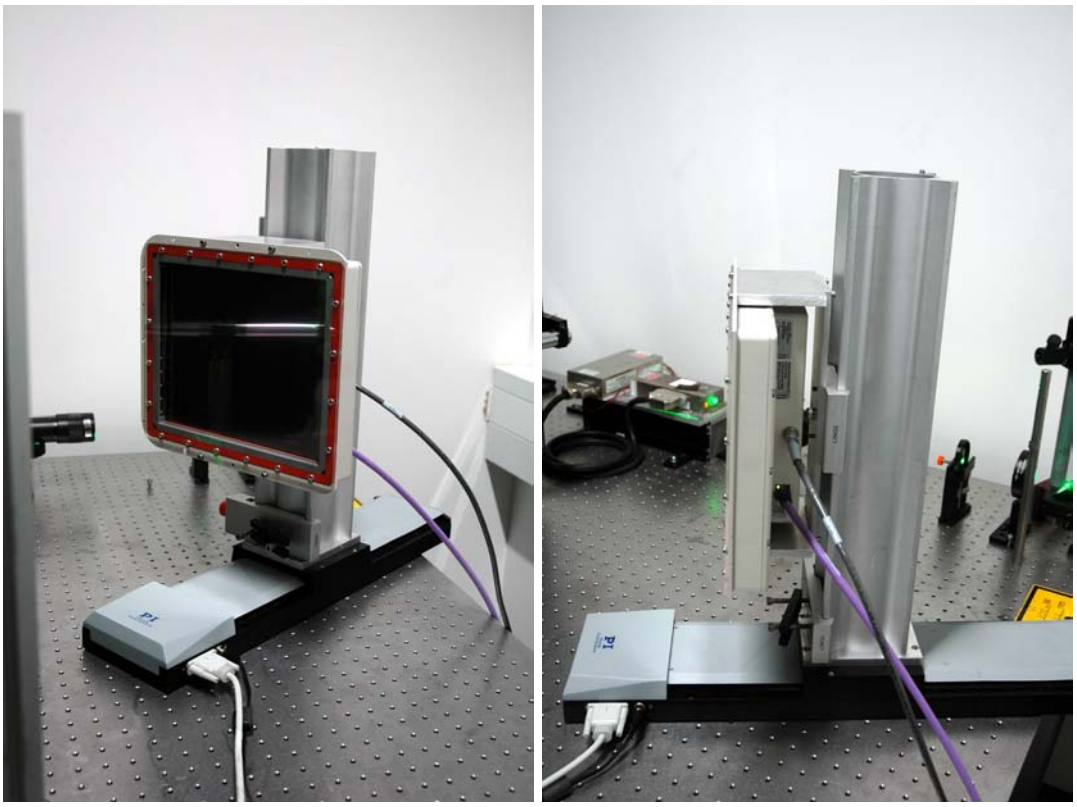

Figure 4.6: The flat panel detector is mounted ruggedly onto the translation stage.

Image Artifacts

The sensor images are free of selfoc lens artifacts. Besides the obvious image modulation, the lens array restricted the effective field-of-view. The FPD does not suffer from these limitations, in effect the focal depth is shorter than with the CMOS-system.

The detector is more sensitive to ambient light and needs to be shielded from stray light. For relief the sensor can be equipped with a green filter glass, making the capture less susceptible to ambient light.

The effects due to surface modulations was eliminated, the residual may be compensated by radiometric gain calibration. The readout is organized in blocks, so the varying response needs to be calibrated. The manufacturer supplies a linear calibration and a defect concealment. This effectively adjusts the gain levels of the individual segments and results in a homogeneous image.

4.3.3 Implementation of the high performance imaging

The detector head is connected to a host PC over Gigabit ethernet cable, so besides a standard ethernet card (Intel Pro/1000 GT) no additional hardware is needed. The ethernet card is controlled by a special driver (Pleora), that is responsible for the quick and stable data transfer. The image data are grabbed directly into the main memory of the host PC, which is equipped with 2.5 GB RAM.[3] The direct memory grab allows a steady high transfer rate.

The detector is mounted to a translation stage (PI) controlled by the host PC. We wrote a C^{++} program to synchronize the image capture with the translation of the detector for digitizing the complete real image with a constant step width. A gain correction and defect concealment

[3]The amount of maximally addressable memory on a 32 bit Windows system is limited. Each program can acquire a maximum of 2 GB memory.

is realized with a library supplied by the manufacturer. After data acquisition the image stack is written to hard disk. Currently our software only implements this basic functionality. A maximum number of 320 images may be held in main memory.

The detector may also be operated by the driver software *Viva*, which is supplied by the manufacturer for fluoroscopic imaging. This software supplies all other functionalities that are needed. An on-line visualization of the image data is possible with this software, additionally image stacks may be loaded into the program. This is convenient for further processing, since the software provides tools for editing the defect maps and image calibration.

4.3.4 Limitations of the high performance digitization

The overall size of the detector 20 cm x 25 cm minimally fulfills the requirement for capturing a complete head. The slightly larger size of the A4 scanner (21 cm x 30 cm) offers additional buffer to allow for real image drift.

To ensure a minimal real image drift in the digitization, it is recommended to align the detector with the principal axis of the PSF. This is however no restriction, since for any scanning method a perfect alignment to the PSF will yield the best possible digitizing result. The detector mount allows for an easy height adjustment.

The optical resolution of the sensor is not as high as the CMOS-scanner used before. Although an optical resolution of 600 dpi was formerly possible, scans were usually performed with only 150 dpi resolution, since otherwise the amount of data was too large to handle in postprocessing. Additionally the information now has a higher grayscale range of 12 bit, so 16 bit are used for the storage format. This doubles the memory demand again. In near future, sensors with a smaller pixel pitch (42 μm - 67 μm) will be available, which are developed for mammography X-ray examination.

4.4 Summary

It is one effort of this thesis to improve the digitizing technique. An X-ray flat panel detector (FPD) was identified as an ideal device for direct real image digitization. The device was adapted to the needs for optical sensing with coherent monochromatic light. In a tight collaboration with the manufacturer, the surface quality of the sensor was optimized. As a result real image slices free of artifacts can now be recorded.

As used before, the digitizing with a commercial CMOS flatbed scanner had many shortcomings regarding speed, dynamic range, mechanical stability. The scan module incorporates a selfoc lens, which additionally introduced disturbing line artifacts.

As a first approach a stabilized CMOS was built with a CMOS line and two translation stages. This design revealed an improvement of the mechanical stability and the removal of the selfoc lens effects.

We developed a program to synchronize the FPD with a translation stage. The real image digitization is performed with a steady shift velocity, avoiding mechanical vibrations.

This new sensor generation for high performance digitization brought many advantages to analog hologram topometry method. The speed of sensing was improved by a factor of 300, reducing the time needed for a real image scan from 2 h to 30 s. The device has a higher dynamic range (72 dB) than the low cost CMOS device, which allows for a wider contrast range.

Image artifacts originating from the selfoc lens were eradicated. The FPD shows no line artifacts and the focus extent is reduced. The mechanical stability was improved and geometrical inconsistencies of the previous CMOS scanning method were eliminated.

In summary the implementation of the new digitizing technique brought an enormous advancement in the quality of the surface reconstruction even with the compromise in detector resolution and size. The hologram quality is less critical than it was before. Even holograms with a very low contrast may still be used for the reconstruction. Although the resolution of the high performance digitizer is lower than with the flatbed scanner, the good image quality and the improved stability produces excellent digital surface models.

Due to this innovation even subjects with subtle skin contrast may be digitized, which was not possible with the former scan methods. The 3D model from a baby cleft patient shows a good reproduction of highlights and at the same time even the cloth is detected reliably (figure 4.7).

Figure 4.7: Four views of a digital model taken of a baby cleft patient. This superior model quality can only be achieved with the new high performance digitizing. For demonstration of the high dynamic range of texture see figure 4.5.

Chapter 5

Digital Hologram Tomography

Digital holography has proofed to be a valuable tool for metrology. Where analog holography already developed many interferometric techniques, the digital counterpart is on a steady rise. Tasks such as microscopy, deformation analysis, object contouring, particle sizing and velocimetry, and position measurement have been realized.

The advantages of a fully digital approach are obvious. No photo material is consumed and the hologram is directly accessible for further processing. The reconstruction is realized numerically, so the chemical processing and the optical reconstruction are dispensable. By speeding up the calculation, a realtime three-dimensional display will be possible.

The measurement of object surfaces is a very live field in digital holography. Light in flight measurements were used to display the depth map of a light bulb ([CNG01]), others use phase shifting techniques [YYMY06], [YIYY06]. One approach to reconstruct the object surface used analog holography to circumvent the problems of speckle noise and performed a surface determination similar to our analog hologram topometry ([MWLJ04]).

The CCD sensors are more sensitive compared to the analog material, so less energy is needed for the exposure. The restriction in pixel size of current sensors still limits the imageable field-of-view of a digital hologram. Methods are proposed to overcome the limited resolution of the chip. One approach describes a coarse sampling of the digital hologram [KG02], [KG03]. Another approach improves the resolution by using a diffraction grating for widening the solid recording angle ([LLB$^+$02]). Additional efforts are taken to account for lens abberations ([SM00]).

The visualization of spatial data is another active field, where holography might contribute substantially (e.g. [WLJ$^+$03]). Another publication describes the reconstruction of a digital hologram from a different perspective ([YAC02]).

In this chapter the digital hologram tomography is presented. With this technique it is possible to reconstruct an object surface with a single laser pulse. It is the first time that height and texture maps are extracted directly from the real image.

In section 5.1 the experimental realization of the pulsed digital holographic recordings is described, the component are a laser and sensor array for recording. The next step is the numerical reconstruction of the real image slices (section 5.2). For this purpose a computer program was developed, which is able to reconstruct the complete real image stack with corrected geometric dimensions. A new implementation on the graphics board shows the potential for a realtime display of the real image.

A new gauging method allows a determination of the recording geometry without measuring the optical path (section 5.3). The imageable area may be extended by considering the illumination (section 5.4). Structured and diffuse illumination techniques are presented (section 5.5) and the visualization of skin is shown (section 5.6). With the methods developed the surface

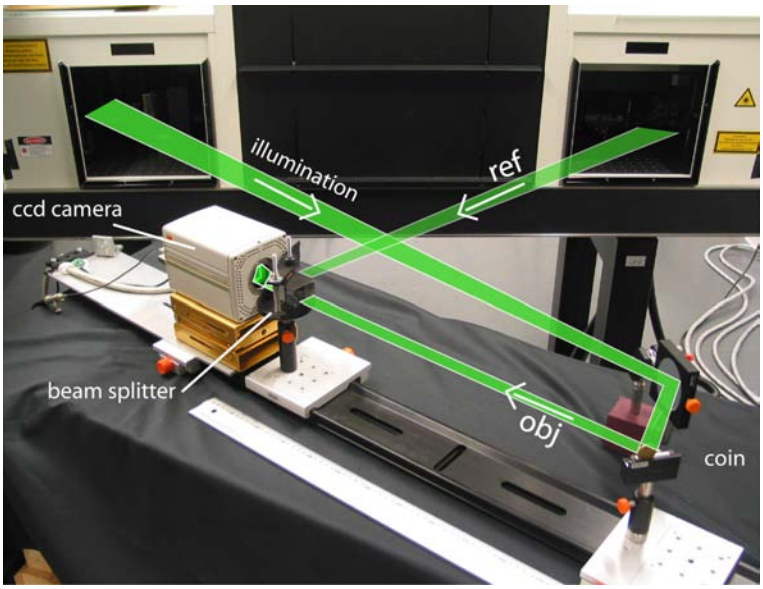

Figure 5.1: A coin is shown as a target from the perspective of the camera. The mirror guides the illumination beam from the side onto the target.

reconstruction of a coin is demonstrated (section 5.7), where the height map and the texture is generated. Section 5.8 shows a promising approach to synthesize several view to attain a larger aperture.

5.1 Experimental setup

As the analog counterpart the concept of holography relies on the separation of the recording and the reconstruction steps. The interference fringes are recorded on a CCD sensor instead of a photosensitive emulsion. With the knowledge of the recording wave, the real image may be reconstructed numerically by a computer. The wave field is reconstructed slice by slice and combined to the digitized real image.

5.1.1 Pulsed holography

In the experiments for digital holography we worked both with the mobile system HSF-MINI and the stationary laboratory system GP-2J. Picture 5.1 shows a set-up with the stationary camera. Contrary to the ordinary use as an analog portrait camera, the beams are reassigned in their purpose. The left port is used for illumination, the right port serves as the reference beam. The diffusor plates are removed to retrieve a spherical wave. The overhead reference beam of the holographic camera is not used at all. The camera features motorized beam splitters, making the adjustment of the beam intensities and the energy balance between reference and illumination beam very convenient.

The reference beam formation was realized in two different scenarios. The first one uses a diverging lens inside the camera and a mirror which guides the light to the outside. At the site of the camera this reference beam has a very wide intensity distribution. Unfortunately it is prone to dust on the optics, so diffraction fringes are widely visible.

As a second approach the reference wave is formed with a pinhole (figure 5.2). By focusing the beam on a pinhole (30 μm) a reference beam with ideal gaussian shape evolves. The beam shows a diameter of 3 cm in 1.5 m distance. The more homogeneous the reference beam is, the better it is approximated by the simulated spherical reconstruction beam. The residual fringes are due to dust on the beam splitter and CCD chip. The drawback in this set-up is an energy loss at the pinhole.

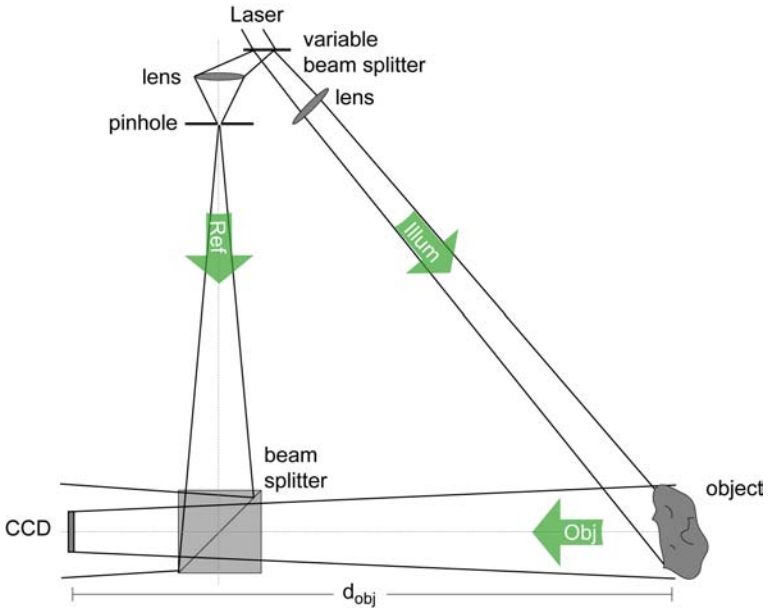

Figure 5.2: Schematic set-up for capture of digital holograms. The laser light is split into reference beam and illumination by a variable beam splitter. The object scatters the light back to the CCD sensor. The spherical reference beam is shaped by a pinhole. A beam splitter directs the beams into the optical axis, where both interfere on the CCD sensor.

The illumination beam from the left port is further collimated to allow for a confined illumination area. This is realized with a convex lens in the beam, which resides inside the laser housing. Further mirrors were used for a variable illumination guidance (not shown). For structured illumination different diffracting elements are introduced in the illumination path (diffusors, line patterns, mirrors).

The beam splitter brings the reference beam and the object beam in line. The reference beam passes a glass beam splitter (50/50) which reflects the beam directly onto the CCD sensor. The object beam passes the beam splitter, meeting the reference beam on the CCD surface. Density filters are introduced at demand for a coarse adjustment of the beam intensity ratio. The CCD camera, the beam splitter and the target are mounted on an optical rail for a simple alignment.

The coherence length of the laser is larger than 6 m, so it is dispensable to match the optical path lengths between reference and object beam. Furthermore any set-up for holography needs to fulfill strict stability requirements, the optical path may not vary by more than 1/5th of the recording wavelength during exposure. With the use of a short-pulsed laser this prerequisite is easily met without any further precautions.

Conventional holographic film has a dramatically higher resolution than CCD sensors ($>$ 50 times). With high-resolution film wide recording angles are possible, allowing an off-axis arrangement. In digital holography the recording is usually only slightly off-axis by a few degrees. The advantage of a CCD sensor over holographic film is the higher sensitivity. The Slavich VRP-M emulsion we use needs 20 - 40 $\mu J/cm^2$ for exposure and is only linear in a very limited range. In comparison, a typical sensitivity for a CCD is 0.01 - 0.1 $\mu J/cm^2$. So the energy demand for the exposure is about three orders of magnitude lower. This means that the laser can be operated in *pilot mode* where a high repetition rate can be achieved with a pulse energy of 3 μJ.

In conventional holography the intensity of the reference beam is dominant compared to the object beam ([Bon02]). The intensity of the object beam depends on the reflectance of the surface, its distance and orientation towards the sensor. So the domination of the reference beam ensures that the optimal intensity interval of the emulsion is met, with the drawback of a reduced contrast.

For the contrast it is ideal if the reference beam and the object beam have the same intensity. In digital holography both beam intensities may be balanced easily, enhancing the contrast to the maximum. This can be done by measuring the response of the CCD chip separately for the object beam and the reference beam. These should have equal intensity while not overexposing the sensor when measured together.

5.1.2 Camera for digital capture

For the recording of the fringe pattern a digital camera is used. The available sensor chips are obviously a lot smaller in size than film plates. The dimension of the chip (aperture) defines the spatial resolution of the real image (see section 2.1.4).

The digital camera is triggered by the laser and synchronized to the short pulse. Due to internal delay of the camera, the typical exposure time is 1 ms, which is sufficient to suppress the ambient light. A better coordination would allow an even shorter exposure time to fit the 20 ns pulse.

For hologram capture three different types of monochrome cameras are used: an interline transfer camera, a CMOS camera and a full-frame camera (table 5.1).

A Kodak Megaplus ES 4.0 interline transfer camera is the default capture device. This camera features a rather dated KAI-4000 CCD microlens sensor which is nevertheless still being used for its excellent dynamics (62 dB, 12 bit), fill factor (60 %), and high sensitivity (0.08 $\mu J/cm^2$). The CCD sensor has 2048 x 2048 square pixels (15.2 mm x 15.2 mm) with a 7.4 μm pitch. The minimum exposure time is 98 μs and the camera may be triggered externally with a fast response. The camera is connected to the PC with a Matrox Meteor II digital LVDS framegrabber and delivers a frame rate of 2 Hz. The sensitivity of silicon substrate CCD sensors is typically from 400nm to 1000 nm in wavelength, usually restricted to the visible range by an infrared filter. Without such a filter infrared topometry is easily possible.

The PixelLink PL-A781 Firewire camera with a monochrome Fill Factory IBIS4-6600 CMOS sensor of 2208 x 3000 square pixels (7.73 mm x 10.5 mm) and a pitch of 3.5 μm shows a wide field-of-view. With the fast reset shutter it is apt for strobe illumination. The minimum shuttered exposure time is 63 μs, so holograms may be captured in bright sunlight. The camera shows a very long trigger delay and the noise equivalent is poor, even after flat field correction. Nonetheless the CMOS cameras are most promising candidates for shrinking the pixel pitch. One enormous advantage of CMOS cameras is that the ROI (area-of-interest) may be chosen deliberately. At the highest resolution the frame rate is 5 Hz, by selecting a smaller pixel area the frame rate increases proportionally. Especially for aperture synthesis applications these cameras might be a good, cost-sensitive choice.

The high resolution full frame sensor DALSA FTF5066M with a customized evaluation board as a camera is the third camera used.[1] With a Bayer color coding these sensors are included in digital backs to equip large format cameras (e.g. Sinar eMotion75, JenOptik). The sensor has 6668 x 4992 pixels (48 mm x 36 mm) with 7.2 μm pixel pitch and a fill factor of 90 %. The resolution is true 12 bits at room temperature. The quantum efficiency has its maximum of 43 % at 530 nm wavelength. The chip may deliver 0.7 Hz with one output channel and 1.4 Hz with two channels.

The motivation for increasing the sensor dimension is to obtain a shorter Rayleigh length of the real image. This reduces effectively reduces the axial resolution (equation 2.31) since the axial resolution scales proportionally to the sensor size. When comparing the relative sizes of the sensors, the new sensor[2] yields a reduction in focus of more than a factor of 8. The computational

[1] The procurement of this sample sensor was time-consuming since it is not available on the general market. The high resolution camera was delivered right before this thesis was handed in, so unfortunately there are no results included.

[2] Number of pixels compared to the Kodak Megaplus ES 4.0, θ_{max} for a wavelength of 532 nm.

camera type	pixel pitch	resolution	θ_{max} (532nm)	rel res
Kodak Megaplus ES 4.0	7.4 μm	4 Mpixels	2.06^o	1 x
PixeLink PL-A781M	3.5 μm	6.6 Mpixels	4.35^o	1.65 x
DALSA FTF5066M	7.2 μm	33 Mpixels	2.12^o	8.25 x

Table 5.1: A direct comparison of the 3 cameras shows the increase of resolution. The relative resolution (rel res) is calculated with respect to the KODAK chip.

effort is a lot higher, yet, due to the introduced optimizations (section 5.2.3), still feasible.

The full frame sensors have the advantage of using the full light-sensitive area. But opposed to interline transfer or frame transfer chips, which may be shuttered electronically, no light insensitive shift registers are present ([Hol98]). The shifting is performed in the same registers that do the recording. So while recording and reading out the chip is still light sensitive. As a consequence this type of chip always needs an external shutter to regulate the exposure.

The blocking of undesired light is not solved for the use of this sensor type in digital holography. When using dim light while capturing, the stray light may be reduced widely. The background may be reduced also by subtracting the stray background after exposure. Since no lens is present, the background will contribute mainly low spatial frequencies to an offset, by the described approaches for DC-term elimination (section 2.2.2) these will vanish. Another effective measure to reduce the influence of the no-green spectrum is to use a narrow green selective filter before the camera aperture.

Currently the camera data bandwidth is the only limiting factor for the repetition rate of the set-up. This merely technical restriction may be overcome by high speed cameras with fast internal memory access.

5.2 Numerical reconstruction

The known methods for numerical reconstructions of the real image have been described in section 2.2.1. These provide the possibility to calculate an image slice at an arbitrary position within the wave field.

For gaining full control over the numerical reconstruction of digital holograms we implemented the algorithms ourselves. Programs for single image reconstruction are available as freeware (see e.g. HoloVision)[3] or commercially, some of which also showed unsatisfactory results.

A drawback of our Java implementation is the slow computational speed, which is a common shortcoming of Java. Having a real-time functionality in mind, Java is a highly inappropriate choice.

5.2.1 Implementation of the numerical reconstruction

The reconstruction algorithms are fairly simple to implement, yet care has to be taken for boundary conditions and image preprocessing. This work was partly done in the context of a diploma thesis by Stephanie Heintz ([Hei06]). The software we developed contains all the extensions for image filtering, stack reconstruction and scaling correction.

For rapid development we implemented the algorithms initially in ImageJ, which is a Java based open framework for image processing [RS03]. The routines for image and stack handling, like imports or exports are provided and the program can be extended by programming plug-ins in Java. This program is widely used in our research group, e.g. for the surface finding or in stack

[3] http://www.edge.no/holovision

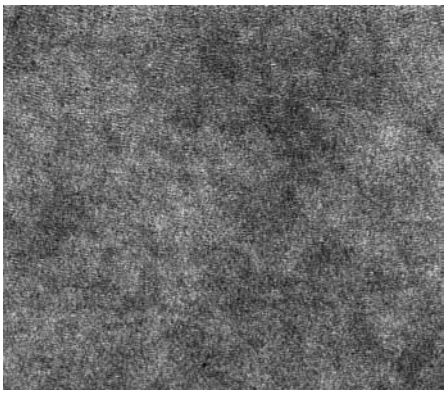

Figure 5.3: A clipping from a digital hologram of a coin recorded with the Kodak Megaplus ES 4.0 CCD camera.

simulations.

As described above we use the Fresnel approximation for numerical reconstruction (equation 2.54). The phase factor and the reference wave are calculated, multiplied with the hologram and finally an inverse Fourier transform (iFFT) is applied.

In the reconstruction program we can set all required parameters:

- reference wave type (plane/spherical wave)
- reference wave origin (for spherical wave)
- tilt of the reference wave (two angles towards optical axis)
- wavelength of laser light source
- pixel pitch of the detector
- object distance
- optional mean value subtraction + high pass filter
- number of slices
- spacing of slices
- lateral scaling correction.

The convolution approach was implemented as an option, but was not used throughout this work.

The holograms are captured with a resolution of 12 bit. For the transfer to ImageJ 16 bit gray scale images are used, so no information is lost. The calculations are performed on complex double precision float values.

With this implementation we are able to reconstruct image stacks of the real image with correct scaling. The results of the reconstruction may be used for metrology already, since target points can be easily identified and due to the constant lateral scaling, the volumes can be measured without further accounting for the perspective scaling.

For improvement of computation speed a newer implementation is realized entirely in C^{++}. A command line tool contains only the basic functionality for Fresnel reconstruction, using a spherical reference beam and the optimized filtering. The output of each slice is written directly to disk as a raw-format, so no memory restrictions apply. In future the program will be integrated with image capture routines and a hardware acceleration will allow a live display (section 5.2.3).

5.2.2 Reconstruction of image stacks

The final aim of the digital holographic approach is to attain the numerically reconstructed real image in tomographic slices. These slices are then further processed for surface finding.

For digital hologram tomography the complete real image is needed, but in literature only single slice reconstructions are used. As described earlier the imageable area increases proportionally to the squared object distance, which is a typical perspective projected view. The reconstructed image is a plane within a pyramid (figure 5.4). The pixel size is not isotropic throughout the image stack, which has to be accounted for.

Favorable is a corrected parallel projected view, where the lateral scaling is constant throughout the stack.

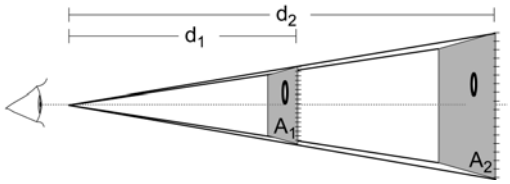

Figure 5.4: The visible space is described by a pyramid. Objects closer to the observer appear bigger in respect to the total imageable field A.

In the Fresnel reconstruction the size of the pixel is described by equation 2.53. An object further away from the observer ($d_1 < d_2$) appears smaller in relation to the total imageable area ($A_1 < A_2$). In the numerically reconstructed image each plane is represented by the same number of pixels. So the resolution within the reconstructed stack varies with the distance to the observer (figure 5.5 a)).

For further processing it is most convenient to handle an image stack with constant scaling. Otherwise in registration steps the anisotropic scaling has to be handled appropriately. To obtain a constantly scaled stack, each plane has to be corrected in dimension. As a first approach, we chose to down-sample the planes closer to the observer. The loss in resolution is tolerable since the image stacks will be smoothed at a later point anyways, which is equivalent to a effective loss of resolution. A different option may still be implemented at a later point.

The scaling factor s_i of a plane is according to the relative distance d_i in relation to the farthest distance d_0 from the observer. According to the intercept theorems, each image i is scaled by

$$s_i = \frac{d_0 - d_i}{d_0}. \tag{5.1}$$

After scaling (figure 5.5 b)), the image is padded with black pixels to fill the original image size. This procedure is applicable if the axis of the image pyramid is perpendicular to the optical axis. The recording set-up is usually designed to meet this requirement. A deviation will occur if the simulated reference beam does not coincide with the alleged reference beam during recording.

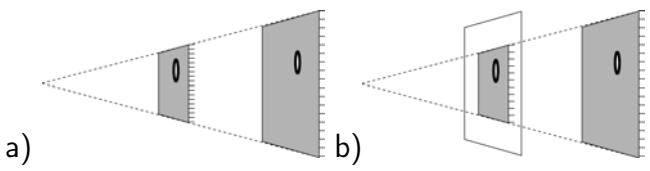

Figure 5.5: a) Before scaling correction, planes closer to the observer are resolved finer. b) After down-scaling of the planes, the image is embedded in an image of the original size. The lateral resolution is constant throughout the real image stack.

If the image pyramid includes an angle with the optical axis, not only a scaling but also a shift

have to be compensated for (figure 5.6). The shift is proportional to the relative distance of the plane. Each image has to be shifted by:

$$r_i = \frac{|d_0 - d_i|}{|d_0|} r \tag{5.2}$$

After scaling (and shifting), the lateral resolution is constant throughout the stack. A deviation may occur when the simulated reference beam does not coincide with the recording reference beam. The shifting will be described later (section 5.4), where a higher order cell is imaged.

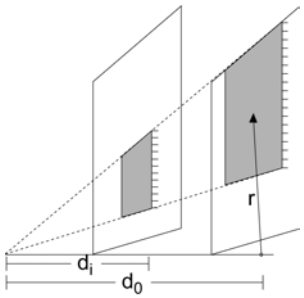

Figure 5.6: Generally a scaling and a shift have to be applied to transform the object into the image plane by the factor $(|d_0 - d_i|)/|d_0|$. r is the difference from the axis of the image pyramid to the axis perpendicular to the object plane.

After scaling, the images are padded with a black background. Figure 5.7 shows a stack reconstruction, where the zero order diffraction term is completely eliminated with an optimized high pass filter (section 2.2.2).

Figure 5.7: Exemplary slices of a scaled image stack, the images closer to the observer are scaled and padded with black. The coin was positioned at 40 cm distance, tilted towards the camera. The inter-slice distance for the examples is 8 mm, a focus progression is visible.

5.2.3 Real-time numerical reconstruction

We investigated further possibilities for the speed-up of the numerical reconstruction of holograms. The dominant main part of the computational cost is the Fast Fourier transform (FFT). Besides the standard ImageJ Java implementation (FFTJ), two alternative FFT implementations were compared.

- FFTJ
- FFTW
- GPUFFT

The speed judgment of an implementation does not include the time required for loading and saving the image, only the algorithm itself is evaluated. The complex multiplication of the

hologram preceding the FFT is omitted. The FFT library used in the Java implementation is provided as an ImageJ plugin.

There are common libraries available with highly optimized FFT algorithms. We chose the FFTW algorithms, which claims the highest performance ([fft]) and is at the same time rather simple to implement.

The second approach uses specialized hardware acceleration. There are very recent efforts to calculate an FFT on the graphics board directly ([OSH05]) and not by the processor of the computer (CPU). Modern highly accelerated graphic processors (GPU) for normal computers are dedicated to very specific calculations needed for display purposes. The libGPUFFT developed at *caesar* utilizes the graphics hardware to formulate the FFT algorithm as OpenGL commands. These processes are hardware accelerated, so an enormous speed boost is possible.

The GPUFFT algorithm is designed for graphical realtime rendering of textures for 3D, aiming at image sizes of up to 1024 pixels. For our needs the algorithm was extended to cope with larger images, we achieved sizes up to 4096 pixels. The GPUFFT transfers the image data from the CPU to the GPU, performs the calculation and transfers the information back to the CPU.[4] The algorithm was implemented in C^{++}.

Table 5.2 shows the comparison between the 3 FFT implementations. The benchmarks were computed with a PC equipped with 2x Dual Core AMD CPU (64-Bit) with 2.2 GHz each, 16 GByte main memory and the graphics board QuadroFX 4500 PCI-Express with 512 MByte.

PIXEL	FFTJ (JAVA)	FFTW (C++)	GPUFFT (C++)
256	94 ms	5 ms	5 ms
512	360 ms	51 ms	13 ms
1024	1846 ms	218 ms	49 ms
2048	7536 ms	920 ms	193 ms
4096	-	9549 ms	1299 ms

Table 5.2: The computation time for the FFT with different algorithms for various image sizes.

The comparison showes that the performance increases from the Java to the FFTW by a factor of 8, for larger images the GPU further accelerates the computation by an additional factor of 5-8. The speed improvement of the GPUFFT to Java increases with increasing image size, for 2048 pixels it is 40 times. Images of 4096 pixels side length did not reconstruct in ImageJ due to memory restrictions of the program. For the performance of the GPUFFT the processor speed is widely irrelevant, since most operation is performed on the graphics card. The CPU is available for other tasks.

For larger images the speedup is nearly two magnitudes. In the GPU implementation the image is transferred to the GPU and back after the computation. For larger images the transfer time is negligible compared to the computation time. The acceleration increases with the image size processed. The results above show clearly that realtime reconstruction of the holograms are possible even for larger sizes.

The Fourier transform is implemented completely with GPU acceleration and shows a good performance as shown above. The only restriction is the complex multiplication, which is still implemented in C^{++} and not optimized. We are currently implementing a complete computation of the reconstruction on the GPU which will further optimize speed. If only a display is needed, the transfer to the CPU has to be performed once, a transfer back is not needed. A tool where the user can interactively manoeuvre through the real image in realtime will be available then.

[4]The bandwidth from the CPU to the GPU is very high. The transfer from the GPU back to the CPU was very slow in the old PCI standard and posed a bottleneck for the GPUFFT. Only in the newer PCI-e this channel has the same bandwidth.

Figure 5.8: A metal ruler is used as a gauging object. With the micrometer screw, the ruler is translated parallel to the optical axis.

5.3 Gauging of the real image

Theoretically the gauging for a reconstruction of the real image would be superfluous, if all the reference wave properties were known. Then the conjugate reference wave could be replicated precisely.

In optical reconstruction the beam is formed to approximate the goal as good as possible. The fine tuning of the reconstruction wave is done by reducing the abberations of the real image. If the real image is free of abberations, the beam must be exact.

For numerical reconstruction all necessary parameters are theoretically given, yet in experimentation cumbersome or nearly impossible to access. So a gauging method was developed to provide reconstructions with a correct scaling. By imaging an object of known dimension the correct scaling of the real image may be obtained.

5.3.1 Gauging approach

The determining factor for the scaling of the real image is the origin of the reference wave. All other properties, such as wavelength, sensor pixel pitch and size are known. As pointed out in section 3.2.2 for the optical case, a wrong choice of the reference wave will lead to a scaling of the real image.

Measuring the optical path length of the reference wave is error prone. In the set-up used, the reference wave was shaped by a convex lens and resided in the camera housing. The optical path length of the object beam and the reference beam may be measured by a laser tracker, yet there is a direct method to gauge the set-up.

With the following method the real image may be gauged without measuring the reference distance nor the object distance. Any wrong reference wave origin may be assumed, only the gauge object of known extent (figure 5.8) has to be numerically reconstructed, the focus has to be found.

5.3 Gauging of the real image

The hologram may be regarded as a lens with the focal length f (figure 3.9). d_g being the object distance and d_b being the image distance, the lens equation gives

$$\frac{1}{f} = \frac{1}{d_g} + \frac{1}{d_b}. \tag{5.3}$$

If the hologram is illuminated from the reference wave with its origin in the distance d_{ref} a focus will appear at d_{obj}. The focal length of the hologram is

$$\frac{1}{d_{ref}} + \frac{1}{d_{obj}} = const. \tag{5.4}$$

It has to be understood that however the reference beam is chosen, an image will evolve. A wrong reference wave will nonetheless provide a real image, only with wrong dimensions. Dependent on the choice of the reference source a scaling is introduced. Unfortunately a wrong choice of the reference wave source is not as apparent as in the analog case, where the real image will be obviously distorted.

The properties of the hologram will remain the same, so for two arbitrary pairs of reference/object values equation 5.4 yields

$$\frac{1}{d^1_{ref}} + \frac{1}{d^1_{obj}} = \frac{1}{d'_{ref}} + \frac{1}{d'_{obj}}. \tag{5.5}$$

For an estimated (or arbitrary) reference wave origin d^{est}_{ref} the object appears at a resulting position d^{est}_{obj}. The position of the real reference wave origin d^{real}_{ref} is determined by

$$d^{real}_{ref} = \Big(\frac{1}{d^{est}_{ref}} + \frac{1}{d^{est}_{obj}} - \frac{1}{d^{real}_{obj}}\Big)^{-1} \tag{5.6}$$

So the real reference value can be deduced for the estimate values and the real object distance. The length of the optical path between the object and the sensor may not be directly accessible due to two reasons. Firstly, the light beam passes a beam splitter, where it has a longer optical path than in air. Secondly the position of the CCD sensor in the camera case is not obvious or the object sometimes difficult to measure. The real object distance can be deduced, simply by measuring the numerically reconstructed image.

Depending on the distance between sensor and object, each plane has a different resolution. The factors determining the pixel size of the real image is the pixel pitch $\Delta\xi$ of the sensor, the number of pixels N, the wavelength of the light λ and the extent of the object d_{obj}, given by relation 2.53:

$$\Delta x = \frac{d_{obj}\,\lambda}{N\Delta\xi}. \tag{5.7}$$

The first two values may be extracted easily from the sensor specifications, the wavelength of the light is known.

With a target of known extent d_{ext}, the real image distance can be determined without measuring the set-up. The correct pixel scaling Δx_{real} can be deduced only by measuring the pixel extent ΔN in the reconstructed image:

$$\Delta x_{real} = \frac{d_{ext}}{\Delta N} \tag{5.8}$$

Reformulating equation 5.7 gives

$$\frac{\Delta x}{d_{obj}} = \frac{\lambda}{N\Delta\xi} = const. \tag{5.9}$$

A constant ratio between the object size (i.e. the resolution) and the distance may be intuitively derived from the intercept theorem (see as well figure 5.5 a)).

So we attain

$$\frac{\Delta x^{est}}{d_{obj}^{est}} = \frac{\Delta x^{real}}{d_{obj}^{real}} \tag{5.10}$$

Substituting the real value of the object extent, equation 5.8 reveals the real object distance:

$$d_{obj}^{real} = \frac{d_{ext} d_{obj}^{est}}{\Delta N \Delta x^{est}}. \tag{5.11}$$

or with relation 5.7

$$d_{obj}^{real} = \frac{d_{ext} N\xi}{\Delta N \lambda}. \tag{5.12}$$

With equation 5.12 the real object distance d_{obj}^{real} may be calculated only by measuring the pixel extent of the reconstruction at the estimated distance. Finally, in equation 5.6 all values are known to calculate the correct d_{ref}^{real}:

$$d_{ref}^{real} = \Big(\frac{1}{d_{ref}^{est}} + \frac{1}{d_{obj}^{est}} - \frac{\Delta N \lambda}{d_{ext} N \Delta\xi}\Big)^{-1}. \tag{5.13}$$

The exact reference wave origin may be obtained by this rather simple approach. For an arbitrary reference value the resulting object distance is calculated. Measuring the pixel extent of a gauge object at this alleged distance directly yields the scaling factor. Neither the real object distance nor the reference wave origin need to be measured directly.

A refinement towards gauging with a spatially extended object with two scaling dimensions is the next step. This generalization will include not only the reference point's origin, but also its tilt. This procedure will ease the experimentation further, by reducing the alignment effort.

5.3.2 Gauging procedure

A target of known dimensions is placed perpendicular to the optical axis and is recorded. In the case shown in figure 5.9 we used a ruler with obvious dimensions (figure 5.8). A slight deviation away from the perpendicular orientation introduces a negligible error.

The reference beam length is estimated or guessed d_{ref}^{est}. The choice of d_{ref}^{est} may be completely arbitrary, but reasonable value eases the finding of the real image focus. The object is reconstructed numerically and the distance is determined, where the object is clearly in focus, this is the estimated object distance d_{obj}^{est}.

Closer to the sensor the Rayleigh length z_r is shorter (equation 2.31). In closer distances the the focus point may be determined clearer. Yet the relative error is determined by the $\Delta d/d$. Since $\Delta d \approx z_r \propto d^2$ a position close to the sensor is favorable. A tilt towards the camera is noted easily, in this case the object runs out of the focus.

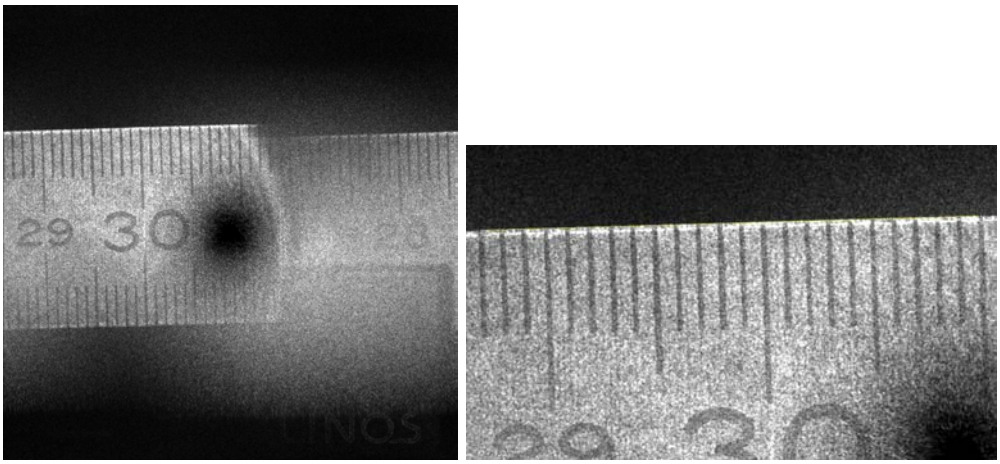

Figure 5.9: Numerical reconstruction of a ruler, positioned perpendicular to the optical axis. The estimated reference beam was -1.8 m and resulted in an object distance of 65.8 cm. The original image dimension is 2048 x 2048 pixels.

With the knowledge of the estimated reference and object distance the correct position of the ruler can be easily calculated as follows. The reconstructed slice with the focussed ruler is measured, with an imaging program like ImageJ ([Ras06]) it is simple to measure the pixel distance ΔN between two known points precisely. The real extent d_{ext} of the pixel distance equivalent is known. Given the gauging formula 5.13 the correct reference wave origin can be calculated.

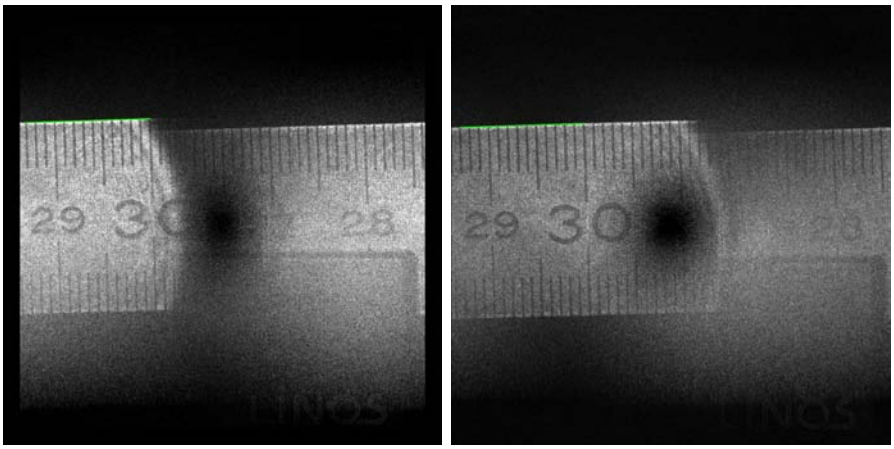

Figure 5.10: Two reconstructions of a ruler 50 mm distance apart, at an object distance of 60.5 cm and 65.5 cm.

After the gauging, the reference wave origin is determined. Each reconstructed plane has a correct scaling. For verification, a ruler was imaged two times, with a micro-positioned offset of 50 mm distance. These holograms were reconstructed numerically and the gauging was performed as described above. The distance of the two slices in the reconstruction are exactly 50 mm, were each ruler is in sharp focus (figure 5.10). The scaling is corrected to be constant in the image, so both times the distance in pixels is equal. The results prove the concept.

The error of the procedure is difficult to quantify. The measuring error of the pixel distance is in this simple set-up 1 pixel. The typical measuring distance is 1000 pixel length, so the error is $\pm 0.1\%$ This could be further reduced by implementing a fit to a target of known geometry. This way an accuracy well below 0.1 pixel can achieved. The second source of error is the gauge target, a metal ruler has a precision of about $\pm 20\ \mu m$. The most deciding factor is the estimated distance of the gauge target which is assessed by bringing the object into focus. The error in the

positioning is the Rayleigh length of the focus, which is dependent on the distance of the object and the aperture of the sensor. With the 1.4 x 1.4 cm^2 sensor size, the positioning error in 60 cm distance was ±1 mm. By multiple measurements at different distances, the accuracy of the gauging may be further improved.

5.4 Extended field-of-view

By evaluating Shannon-Weavers sampling theorem (equation 2.26), it may be suggested that no information outside the imageable area may be reconstructed. The imageable area is indeed not limited to this range [JS04], [SJ06]. Figure 5.11 shows the reconstruction of a metal ruler where image contents overlay.

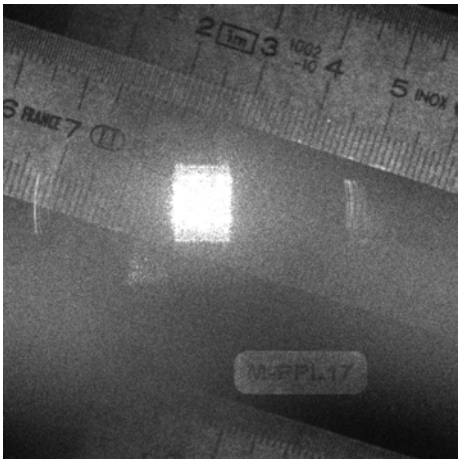

Figure 5.11: Reconstruction of a metal ruler with an obvious overlay of several images.

The sampling theorem formulates the border frequency (Nyquist frequency), above which an *unambiguous* reconstruction is not possible. Above this frequency, aliasing will occur. In figure 5.12, the central dark cell denotes the primary area.

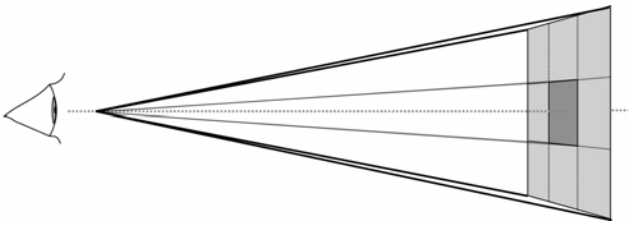

Figure 5.12: The central dark cell shows the theoretical imageable area delimited by the sampling theorem. In the reconstruction the surrounding cells appear as well.

The imageable area at an arbitrary distance may be subdivided into cells of equal extent with the lattice constants u_x, u_y. The extent of the cell is defined by the spatial resolution formula (equation 2.29) and the distance to the sensor. Provided an appropriate illumination the objects from all cells are visible, the view is not confined to the primary cell (0,0). In reconstruction the information is projected into the primary cell, shifted by the lattice constant. The reconstructed image is an overlay of all cells (figure 5.13).

On the sensor, the entire object waves interfere with the reference beam, regardless of the origin of the contributions. The signals from non-central cells will lead to higher frequencies on the sensor (equation 2.24). The incident frequencies are sampled with the grid of the sensor array. So in the sampled signal the frequency information f_i will alias to a frequency f_a. This is a

reduction by multiples of the Nyquist frequency f_N:

$$f_a = f_i \pm k f_N, \tag{5.14}$$

for $k = 0,1,2,\cdots$

So by the sampling step the information originating from different points of the grid becomes indistinguishable. Consequently the complete area is a periodic function of the overlayed information. This is as well inherent in the use of the Fourier transform in reconstruction, where the signal is by assumption regarded as periodic.

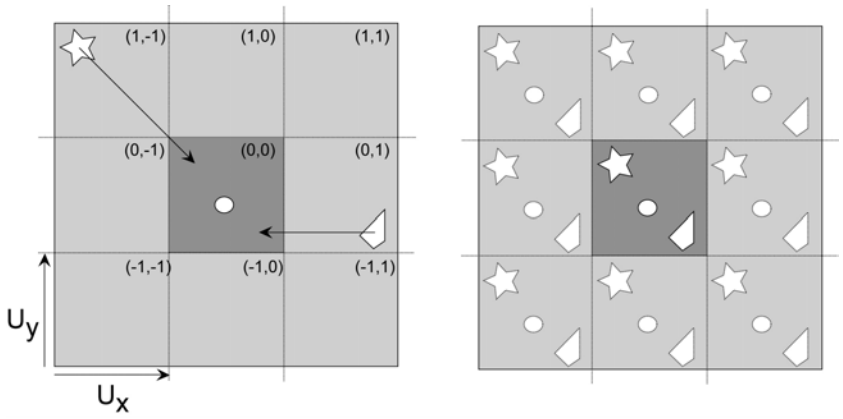

Figure 5.13: The imageable area is subdivided in cells of equal extent (u_x,u_y). The reconstruction is not confined to the primary cell (0,0), highlighted in dark gray. Objects from the other cells can be seen, these are projected into the primary cell, the real image is a periodic overlay of the combined information.

If the image from figure 5.11 is patterned horizontally, the origin of the overlay may be easily identified. These objects originate from adjacent cells and appear to be continuous. As can be seen the spatial aliasing effect may occur both vertically and horizontally (figure 5.14).

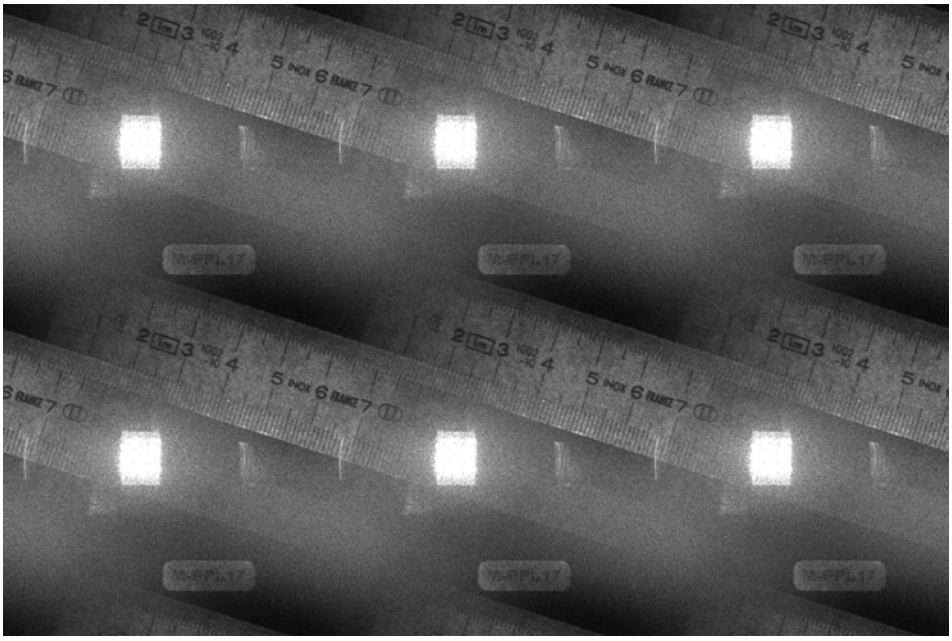

Figure 5.14: A horizontal and vertical pattern of the ruler reconstruction shows a continuous image, overlapping from several cells. The field-of-view is extended, yet the ambiguity makes the contributions difficult to distinguish.

This circumstance must be acknowledged for in numerical reconstruction.

Higher order cells may be visualized. All image parts appear, which were exposed to illumination before. If an object is not illuminated, it will not appear in the reconstruction. For avoiding disturbances, the illumination should best be confined to the target area, whether the primary cell or a higher order cell. This measure improves the image quality significantly, since outlying areas will not contribute to the signal.

An extended field-of-view may be imaged if a coding of the individual cells is accomplished. By illuminating the individual cells successively the information of each cell can be reconstructed separately. This enhances the visibility beyond the Nyquist frequency, which was as well described by [SJ06]. The different cells can easily be combined after reconstruction. The scaling is in accordance to the above mentioned model with shear, additionally an image pyramid shear is compensated (figure 5.6).

Usually the sampling step is described by a multiplication of the signal with a comb function ([Jäh02]). In this simplified notion the aliasing will exhibit undisguised. The physical sampling is rather an integration of the signal intensity over the pixel extent. With low spatial frequency there will be hardly any difference, yet for higher frequencies the differences are notable, and especially the signal will get weaker in the higher order cells.

In the convolution approach, the information retrieved outside the primary cell is simply a multiplication of the self. It is not reasonable to extend the area further, so the lens factor is best fitted so the reconstructed image is identical to the image pyramid described by the sampling theorem.

5.5 Illumination techniques

A careful choice of the illumination is the key to a good digital hologram. One part of the laser beam is directed towards the target for illumination. The light scattered back forms the object beam. In our experiments the aim was to maximize the balance between object wave and the reference wave, which yields an optimal image contrast.

Also a careful confinement of the illumination to the imageable area fosters the reconstruction quality enormously.

For objects with a good texturing or surface variation, a direct illumination is usually sufficient. Low texture contrast may be overcome by a spatially modulated illumination. With this technique an additional image contrast is induced on the image surface.

5.5.1 Homogeneous illumination

The first object that was reconstructed successfully is a 20 cent coin. The coin was tilted towards the camera, since otherwise the height variations were too small to resolve. The object has a matt surface and thus shows a diffuse yet partly directional reflection. This property was used to create an object beam with a high intensity. The hologram was adjusted to maximum contrast, such that reference beam and object beam showed a similar intensity.

The coin shows a high contrast in the real image as well. Dentition, scratches and even marks from embossing are visible on the coin surface (figure 5.15). For a hologram close to the sensor the confined focus is clearly visible.

Most objects were imaged with direct illumination, without further diffusion. With an additional diffusor plate in the broadened illumination beam, eyes-safe captures of the face can be realized.

Figure 5.15: Reconstruction of a coin in 40 cm distance from the sensor.

5.5.2 Structured illumination

If the object does not display enough variation in its texture, or the texture is invisible to the laser light, structured illumination may be applied. These different illumination techniques were performed with the objective of visualizing skin with a digital recording.

By spatially modulating the illumination, an additional texture is projected onto the object surface. The spatial frequency may be optimized to exhibit the surface for later surface detection ([Gie03]). The use of modulated illumination is known for laser scanning techniques or white light scanners. [LKW02] proposes an inverse pattern projection, where the pattern is adapted to the object.

For digital holography two static patterns were tested, stripe projection and speckle pattern projection.

The stripe projection in figure 5.16 was generated with a Fresnel lens in the illumination beam. A simple way for the generation of speckle illumination is by introducing a diffusor screen into the illumination. By varying the beam spot size on the diffusor, speckles of different extent are generated. A smaller beam leads to larger speckles and vice versa.

Pattern projection enhances the contrast of object surfaces in the digital recording. This illumination can be applied to skin as well, examples for speckle projection can be found in the previous works about the analog method ([Bon02], [Gie03]).

5.6 Skin visibility

Holographic measurements techniques are usually performed on objects. The ultimate goal for the digital hologram tomography is to be able to perform surface detection on a living subject. With the green pulsed laser, skin is visible in the real image already. The following recordings were performed with the reference beam, produced by a pinhole in 1.42 m distance. In the *pilot mode* (3 mJ pulse energy), there is not enough energy for the illumination of larger areas. The object beam intensity was low compared to the reference beam (1:20), so the modulation in the real image is dominated by speckle noise. The very low reflectance of skin was enhanced with an application of a cosmetic powder.

Figure 5.16: A plaster statue shows low texture contrast. The visibility of the surface may be significantly enhanced by the projection of a fringe pattern. Although the object was positioned about 1.4 m from the sensor, a focus progression may be observed.

Figure 5.17 shows the reconstruction of a hologram from the knuckles of a hand captured at 57 cm distance. The skin pores can be identified easily, a focus progression is detectable.

Throughout this thesis usually objects of small extent have been captured, which is due to the limited field-of-view of digital holography. The object distance was generally 40 cm - 80 cm. The face in figure 5.18 is recorded at a distance of 1.8 m, the skin pores and wrinkles are clearly visible. At this distance the focus progression is too low for a reconstruction of the surface. At longer distances, the zeroth order term is small compared to the total imageable area. Clearly visible is the virtual image (figure 5.18, left image part), which gets more dominant the further the object resides.

The recordings can be made eyes-safe. A diffusor in the illumination beam, like it is common practice in the analog method (figure 3.5), increases the spot size of the illuminating beam. In the shown set-up the total pulse energy was not high enough to allow further intensity compromises. This may be solved simply by providing a higher energy.

As shown in the next section, surface reconstruction of objects is already possible with digital hologram tomography. It is only due to the lack of pulse energy that made reconstructions of skin tissue difficult. Yet especially when imaged at shorter distances, skin could be discriminated in the focus profile.

5.7 Surface reconstruction

With the analog tomography technique an accurate determination of an object surface was shown by our preceding work. The determination of the focus from a real image reconstruction is the last step towards a surface detection.

The known 20 cent coin is a very instructive example for the surface reconstruction. The dimensions of the object are known to everyone and the geometrical correctness of the reconstruction is

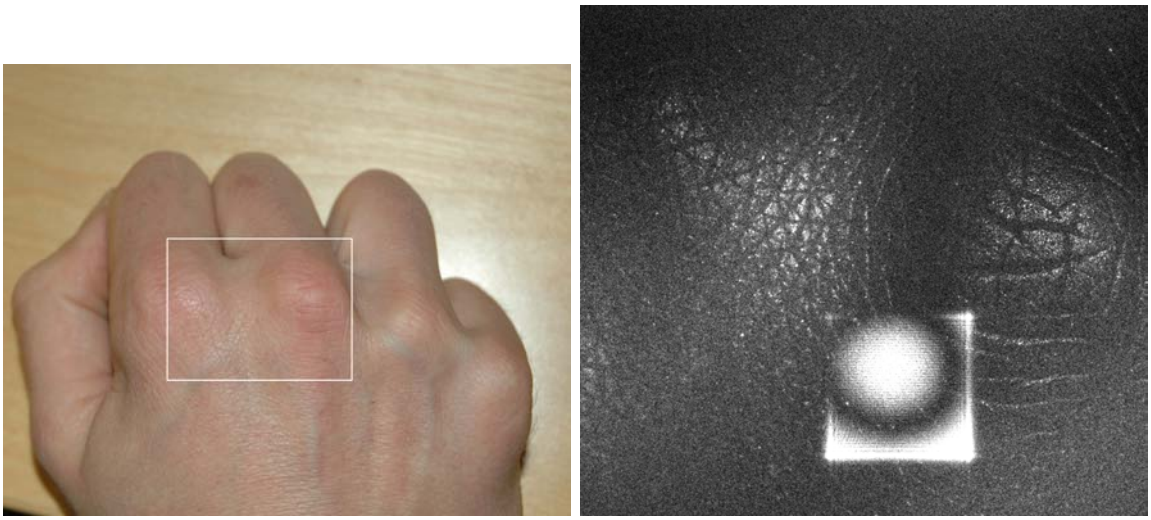

Figure 5.17: Numerical reconstruction of a hologram from human skin (knuckles of right hand) at 57 cm distance. The imaged area is marked with a white rectangle. The skin pores are easily visible in the real image, a focus confinement may be observed.

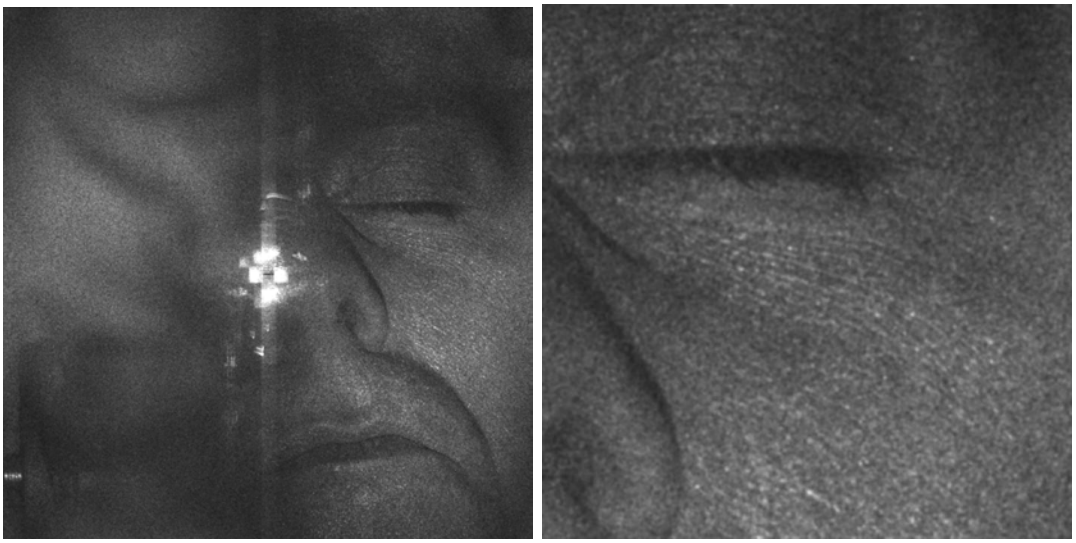

Figure 5.18: Numerical reconstruction of a face at 1.8 m distance. The closeup shows the region of the left eye.

directly accessible. For the shown surface reconstructions the coin was imaged at 40 cm distance, tilted towards the optical axis. The hologram was captured with the 2k x 2k Kodak camera. The stack contained 25 images (sample images shown in Figure 5.7) with an inter slice distance of 1 mm. The pixel size is 13 μm.

One has to keep in mind the dimensions of the real image extent in digital holography. At 40 cm distance the visible area is about 28 mm x 28 mm. In the analog method the accuracy of the surface finding is 0.4 mm, despite the fact of a short focus extent. In this light the surface finding from digitally reconstructed image stacks has to be evaluated. The surface detection was performed with the Sum-Modified-Laplace operator ([The06]), which determines the pixel variance in a defined neighborhood. A typical neighborhood size for the focus measure in analog topometry is 9 pixels, which equals a physical extent of 1 mm (200 dpi = 127 μm/pixel). The seemingly high neighborhood size of 25 pixels (figure 5.19 b)) equals a physical size of 300 μm. So compared to the analog method the focus determination is computed in a smaller neighborhood.

The focused part of the real image resided in 18 slices, from the front to the back of the coin.

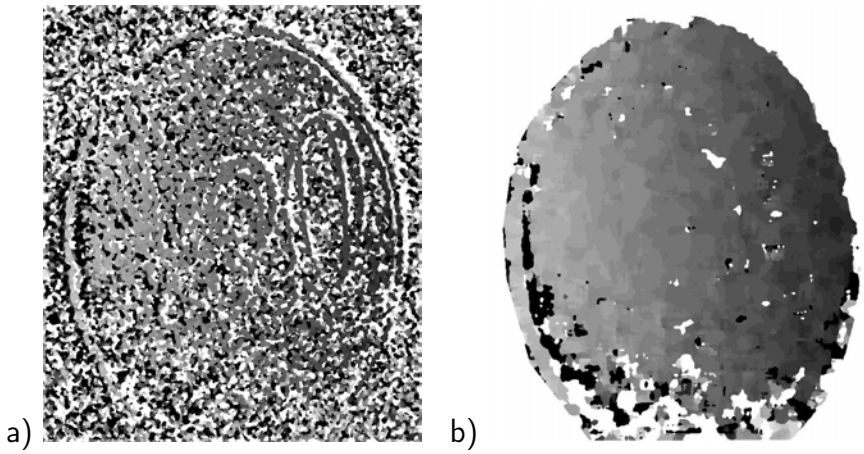

Figure 5.19: Evaluation of the surface with two different neighborhood sizes of the focus measure. a) 15 pixel ≡ 200 μm b) 25 pixel ≡ 300 μm. The surrounding noise in b) was removed for better visibility. White denotes low elevation, black denotes high elevation.

Consequently the resolution of the reconstruction is limited to these 18 discreet steps. These plateaus are visible in the surface plot (figure 5.20). The tilted surface reveals the round shape of the coin again, although the coin appears oval in the real image.

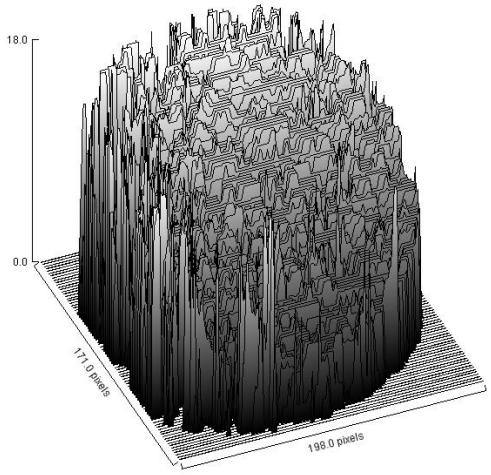

Figure 5.20: The surface plot of the tilted coin shows the digitization steps. The surface describes a disk.

The surface of the real image is extracted at the focus position, as it was demonstrated in analog topometry (section 3.3). This procedure yields a texture map with high detail and full focal depth (figure 5.21 b)), compared to a single slice with a limited focal depth (figure 5.21 a)). As stated before, the coin was tilted towards the optical axis, so in the parallel projection the coin appears elliptic.

The surface finding from the numerically reconstructed real image is possible and shows a good reproduction of the geometrical dimensions. Although a small lateral neighborhood is used, the accuracy in depth is limited by the large axial focus extent. Fluctuations in the surface map are clearly visible. It is possible to extract the surface and the texture at the same time, with the same techniques as used for analog data.

The shown example is calculated from a 2k x 2k hologram. When using a sensor with a higher resolution, the same depth resolution may be achieved at a further distance. The newly acquired DALSA sensor (section 5.1.2) is about 8 times larger than the Kodak sensor, so an 8 times larger area will be imageable with the same focal length. This alone will bring new possibilities to the surface reconstruction quality.

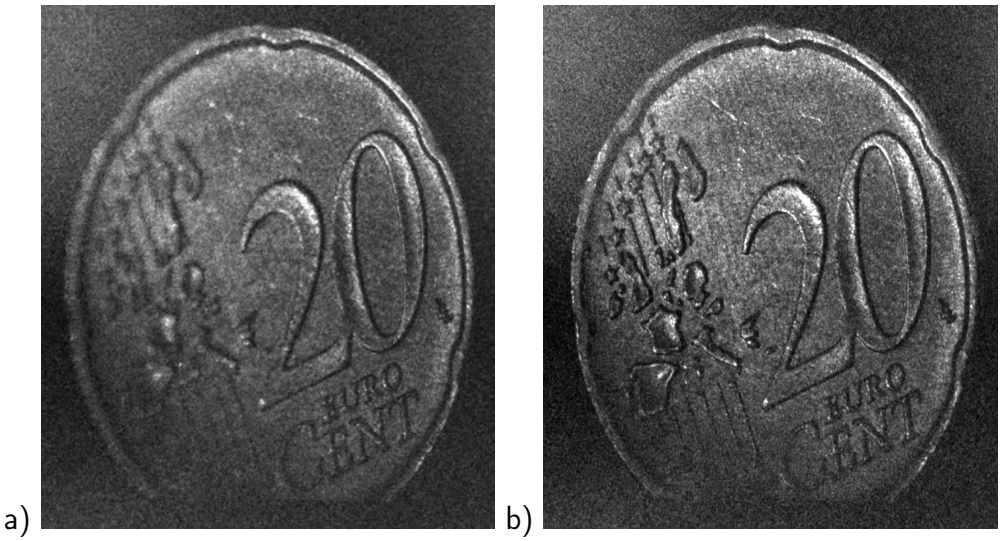

Figure 5.21: a) One slice of the real image shows a clear focus region. b) The parallel projected texture of the coin reveals a full depth of focus.

The digitally reconstructed real image suffers strongly from speckle noise. This behavior is problematic for the focus finding at high resolution.

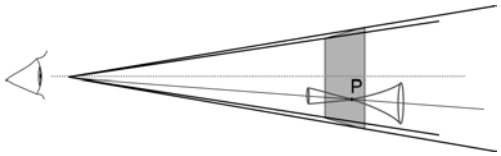

Figure 5.22: The point spread function (PSF) gives the radius to which a point P spreads away from its focus. In the numerical reconstruction the PSF aligns along a ray originating from the sensor. In the uncorrected stack the PSF appears to be symmetric.

The interference pattern on the chip naturally varies with a statistical speckle pattern, so a random phase factor is added to each pixel. For the complete image this factor averages out, but locally it determines the noise. The speckles behave like a conventional conical point spread function (PSF). The intensity profile is distributed noise, following a gaussian probability profile (figure 5.22). Even though a general focus progression is observable, the speckles induce a high local contrast even off the surface.

In the image stack the PSF appears symmetric, since the physical convergence is compensated by the decreasing image extent. In real space the PSF is not point symmetric. As explained, the speckles formate in a cone described by the PSF. In a geometrically uncorrected image, the speckles develop axially. When the stack is geometrically corrected before surface reconstruction, the speckles move radially towards the back. Consequently the surface finding should be performed on an uncorrected image stack.

The surface detection, as it is currently implemented, searches for the maximum contrast in the axial direction for each point (see section 3.3). This method performs best with a symmetric focus progression, otherwise the search strategy for the contrast maximum has to be adapted to the PSF direction ([The03]).

The geometric correction described in section 5.2.2 must be applied after the surface extraction. This results in a vastly improved surface map with less radial distortions (figure 5.24). The displacement of the slice due to the scaling increases towards the outside of the image (figure 5.23). As a consequence, off-center regions show more artifacts in the height map than the central parts.

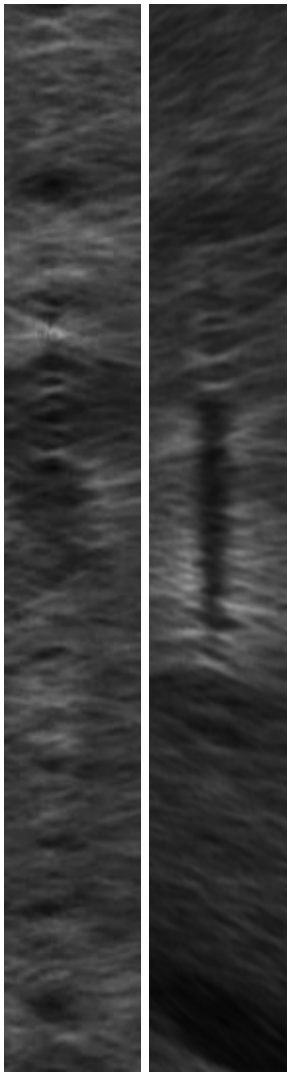

Figure 5.23: In the turned image stack the focus progression can be judged easily. Left: The unscaled image displays a symmetrical focus progression. Right: The scaled image shows a radial focus progression.

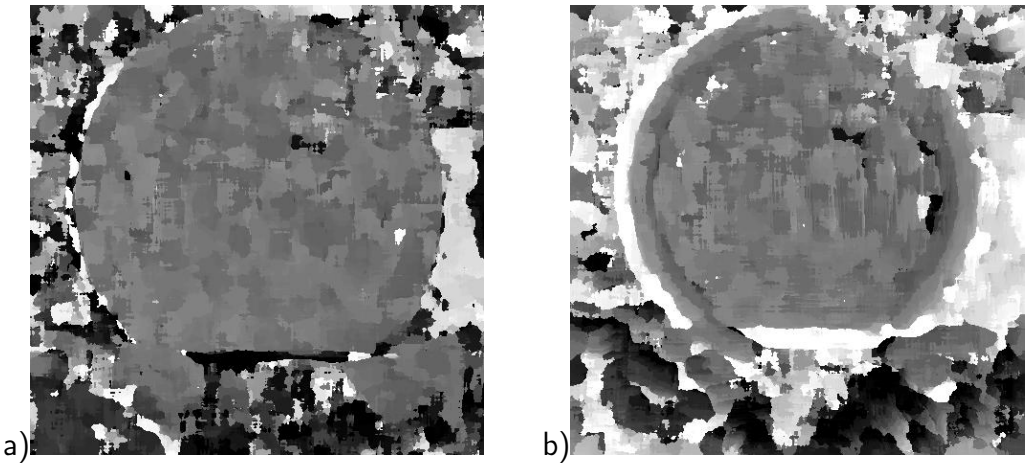

Figure 5.24: a)The uncorrected image stack reveals a well-reconstructed hight map. b) The height map from a scaled image stack shows the correct geometric relations, but the focus finding is distracted by the asymmetric PSF. (both maps were generated with an SML of 21 pixel neighborhood)

The speckle formation has to be investigated further as it is the key to a successful focus determination. The surface finding algorithm has to be further adapted to the special demands in the reconstructed image slices.

5.8 Aperture synthesis

A successful focus detection is dependant on a short Rayleigh length in the real image. As shown before, first surfaces may already be determined, even with a reasonably small sensor size.

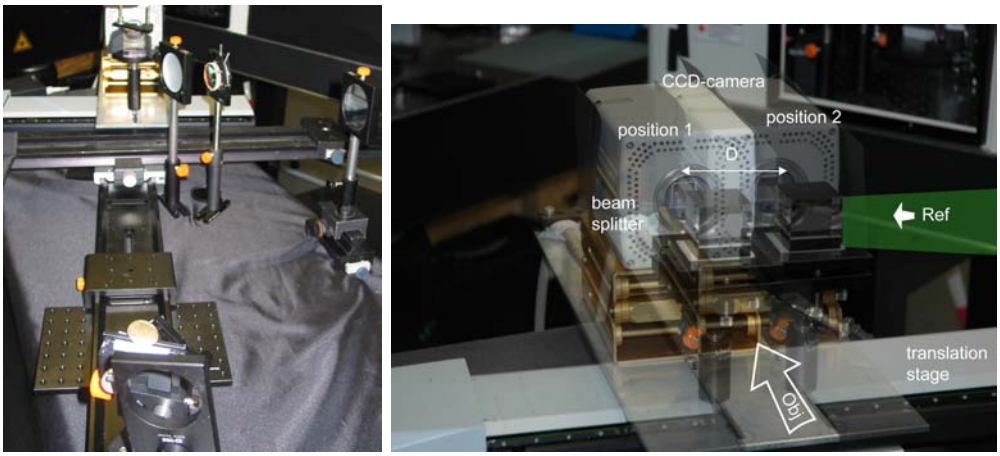

Figure 5.25: Recording set-up for quasi simultaneous aperture synthesis. The beam splitter and the camera travel as a unit. The unit is moved with a linear positioning table to successively record holograms of a static target. The reference beam comes from the right side. Additional mirrors were used for beam guidance.

The lateral resolution of the reconstructions are well below 0.1 mm. The axial focus extent is a lot higher due to the low sensor dimension. For a further decrease of the Rayleigh length the aperture must be extended. It is one strategy to increase the sensor size of a single chip (section 5.1.2).

Another strategy is to combine (synthesize) the information of many sparsely distributed small aperture sensors into one image. This aperture synthesis approach was originally developed for radio astronomy ([Cut90]), where it is widely used. With the sparse array the computation is

much faster.

It is a common interest to combine the holograms from several perspectives. Attempts have been proposed in literature to realize the aperture synthesis. [KAJ02] inserts the small single hologram into one big hologram, which is then reconstructed as a whole. The sub-images are aligned by shift to the appropriate position, the rest being black. This crude attempt is computational demanding, and opposes the original idea of area/computation reduction. The holograms also need to reside in the same plane. Other approaches perform the alignment of the image by calculating the cross-correlation between overlapping holograms ([Mas02], [BCL02]) or by an aperture shift ([LGC01]). A satisfactory approach for the synthesis of apertures has not been proposed yet.

With the developments described in this chapter, a new aperture synthesis approach from arbitrary perspective is possible. The lateral scaling of the reconstructed real image stack is perfectly isotropic, the axial scaling is known by the reconstruction steps.

It is the final aim to capture the different views with one laser pulse. With this short exposure, moving subjects can be holographed. Until now we do not have the facilities to capture two holograms simultaneously. To nonetheless prove the feasibility of the concept, we recorded two holograms of a static target sequentially. Between the quasi-simultaneous recordings, the sensor is shifted. The camera and the beam splitter are mounted on a linear positioning table (figure 5.25). The difference of reference beam length in both recordings is compensated.

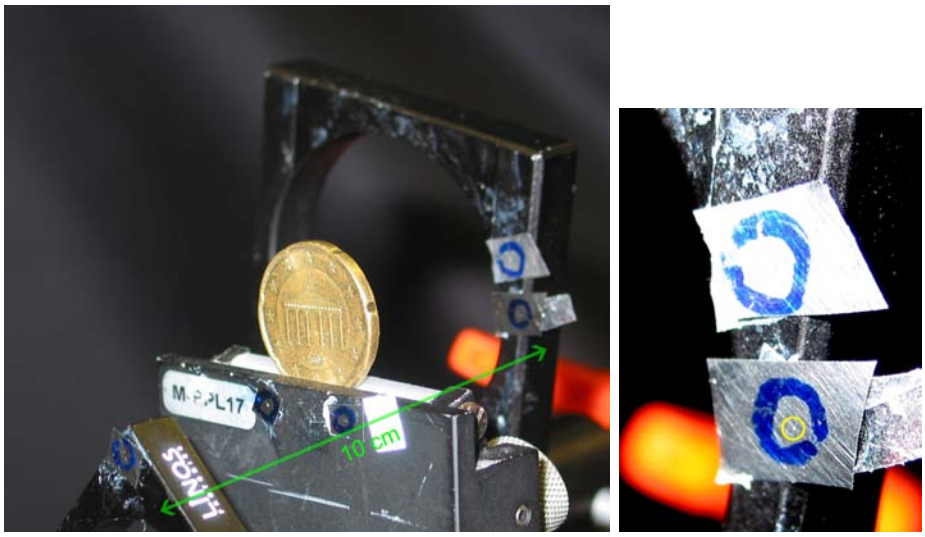

Figure 5.26: The target coin is surrounded by marker points. The marker points are spread over an axial distance of 10 cm. The points are highlighted with a big blue circle for better visibility. Each marker point (indicated with the yellow circle) has a spot diameter of 200 μm.

Two perspectives of the same scene are captured (quasi-simultaneously). By introducing a gauging target, visible to both views, the geometric relation between the views can be established taking into account the correct geometric scaling. For this purpose a set of marker points, which can be precisely identified in the real image, is holographed with the target. In a registration step, these marker points are brought to correspondence. The accuracy will increase with the number of marker points. Due to the spatial resolution, the localization will be more precise laterally than axially. The points were spread over a high axial distance of 10 cm to minimize the alignment error of the registration.

With the registration, the rigid transformation matrix between the formerly independent camera coordinate systems is calculated. With this knowledge, the real image may be transformed into a shared coordinate system, where the stacks are merged incoherently.

The markers are made of roughly polished stainless steel, the matted surface reflected partly

diffuse. The marker dots were shot with a CO_2-laser to a diameter of 200 μm (figure 5.26). The marker is chosen to be very small, so the center can be identified with little error. The choice of a dark spot on a light material makes the manual determination of the focus point easier. The blue circles mark the rough position of the small marker. The marker points are spotted successfully in the real image, where the lateral resolution is about $\leq 50\mu$m. Axially the position of each marker was detected with a positioning error of ± 1.6 mm.

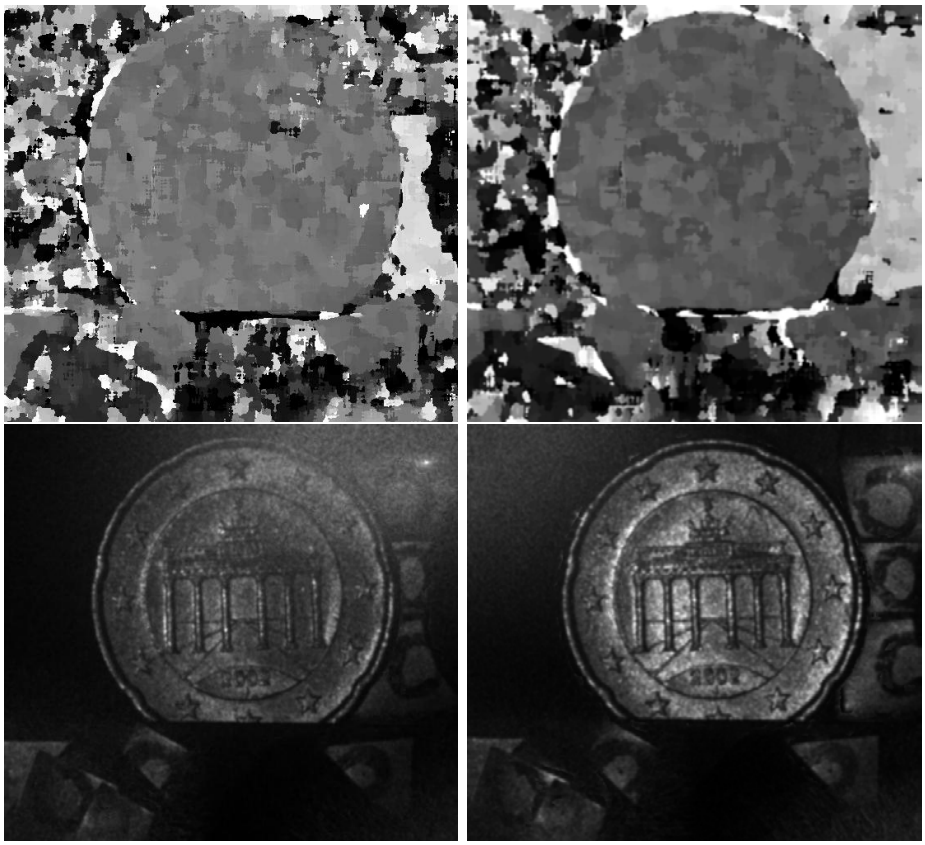

Figure 5.27: The reconstructions of the individual views on the same scene (figure 5.26) yield a height map and a texture map with complete depth-of focus. The individual marker points can be spotted easily in the image.

The matching of the two perspectives did not show satisfactory results yet. This was mainly due to two reasons: mismatch of the reference beam parameters and an insufficient matching algorithm.

One prerequisite for a geometrically consistent real image is the exact matching of the reference beam with the reconstruction beam. Although the reference beam origin was determined precisely, the tilt of the reference beam was not reproduced sufficiently. This shortcoming has to be overcome with a better alignment or the gauging method has to be extended to account for the tilt as well.

The matching was performed with an ICP-approach (iterative closest point), where the coordinates of each point are weighted equally. The axial resolution ($\approx 1mm$) and the lateral resolution (≈ 50 μm) are very different, which has to be accounted for.

These are the only remaining issues for a successful application of the synthetic aperture. It can be expected that the synthesis of several holographic views will be possible very soon with the devised method.

5.9 Summary

Hologram topometry offers the potential to reconstruct a digitally recorded hologram numerically. The process is fully digital from image capture to the final height map and was never accomplished before. In comparison to the analog method no additional optical unit or a wet-chemical processing is needed.

Yet restrictions apply due to the limited resolution of a CCD in comparison to a holographic emulsion. A real image stack may be calculated numerically, the lateral resolution is constant. A novel gauging procedure was developed, not described in literature yet.

We showed that a real-time calculation of large size holograms is possible with an implementation on the graphical hardware. With this implementation we gain the possibility of a real-time reconstruction even of large holograms.

It was proved that skin may be visualized by the system, which is a big advance towards facial topometry. Different illumination techniques display the applicability to various objects. With structured illumination an additional contrast enhances the surface visibility. The illumination should be fitted to the imageable area to avoid image overlap of neighboring zones.

First height maps were extracted from the real image stacks. The surface finding was performed with the algorithms used for analog hologram tomography. After an optimization of the algorithms even better results may be expected. It is the first time that this process is possible fully digital. The simultaneous extraction of surface and texture have never been reported before.

With the present system it is possible to record motion series with 3 Hz, whereas the only technical restriction is the camera speed. A new full-frame camera is purchased with an increased resolution of 8 times.

A promising approach to synthesize the aperture is presented, which is expected to solve this difficult task in near future by incoherently overlaying the perspectives.

Due to the novelty of the development of digital hologram tomography we have not used the technique in medical applications. One field of application is the time-resolved measurement of facial gestures. Another target field is in the forensics field, where the study of bite marks in skin is of high interest ([BTG$^+$06]). There are numerous industrial applications for contact free 3D metrology, where objects may be imaged in movement due to the short pulse duration.

Chapter 6

Applications of Analog Holographic Topometry

One part of this thesis is dedicated to the instrumental improvement of the real image digitization. With the sum of improvements introduced into the analog technique, some applications are possible for the first time.

Two of these applications will be outlined in this chapter. All known 3D digitizing techniques suffer from a long data acquisition time. Especially uncooperative patients (e.g. small children) are impossible to capture. With the new high performance digitizing a topometry of child faces is possible reliably for the first time (section 6.1). The improved mechanical stability of the digitizer yields a data quality free of artifacts.

It has been demonstrated in earlier work that analog hologram topometry of adults was generally possible with high precision. Yet the reconstructed faces showed a minor yet irreproducible geometric skew within the models, which became eminent when two views from different positions where compared. With the improved direct scanning instrument these errors are eradicated, allowing an accurate measurement of the soft tissue shift free of geometric distortions.

Section 6.2 gives a very instructive example is of a comparison between a reclined and an upright recording. This research is part of an investigation conducted with a forensic odontologist (Frank Prieels). We used a special device mounted to the teeth for the verification of the registration process.

6.1 Topometry of child faces

The knowledge of the individual spatial morphology is the prerequisite for an individualized surgical planning and evaluation. For adults optical 3D data acquisition is widely used ([MMP+02]), but an acquisition of child faces is not possible with the known methods. Until now photographs serve as the only option for documentation and evaluation (figure 6.1).

Cleft lip and palate malformations are very common birth defects, about every 500th child is affected. In case of complete cleft lip nose, hard and soft palate are not closed in the first three months of the development. The grade of the cleft expression varies widely. In developed countries the correction is commonly operated during the first year of life. In a technically demanding operation soft and hard tissues are reorganized. The surgeon restores the functional aspects of the palate (ingestion, breathing, speech development) and reharmonizes the aesthetic appearance of the patient. The overall quality of the aesthetic result has improved vastly over the last decades. There are different operation techniques described in medical literature, but the success of the intervention is difficult to asses.

Figure 6.1: Especially with young patients the digitizing of the face surface is impossible due to the movement of the patient during the measurement. The holographic method allows a face capture even for uncooperative patients.(image source: Dr. Dr. Schwenzer-Zimmerer)

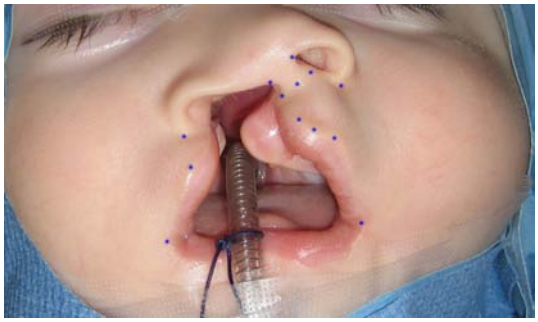

Figure 6.2: Important landmarks identified on the cleft lip before operation (image source: Dr. Dr. Schwenzer-Zimmerer).

Especially the morphology of the cleft lip and nose region shows a major demand to the surgical intervention and preoperative planning (figure 6.2). In every case the 3D soft tissue morphology in cleft lips is individually different and could be operated with a different surgical technique. Therefore it is desirable to have a measuring procedure where the 3D surface is captured as accurate, easy and fast as possible for routine documentation.

Dr.Dr. Schwenzer-Zimmerer (University hospital Basel) attempts to systematize and verify the surgical results ([KCJ+98], [KDI+06]) dependent on operation technique. Experiments with a linear laser scanner and a white light scanner conducted on young children rendered useless.

The established methods for object scanning show excellent results for static objects (white-light, photogrammetric, laser scanner) where the acquisition time may be deliberately long. When applying these systems to living persons the performance and accuracy drops rapidly. Only if the person is immobilized during the measurement, the results are satisfactory. Even shallow breathing, shivering or heart beat will result in distortions above several millimeters. The accuracy of the surface is directly linked to the duration of the data acquisition.

The data retrieval is extremely difficult with baby patients. Where an immobilization over seconds time is hardly possible for cooperative adults, this demand cannot be accomplished by a small child. Even sleeping the child moves for breathing.

One strategy to retrieve a model of the patient is to form a plaster cast of the face. This may only be done with a sedated and intubated patient without further risks. It is clear that this procedure is only reasonable immediately before the actual intervention itself, inside the

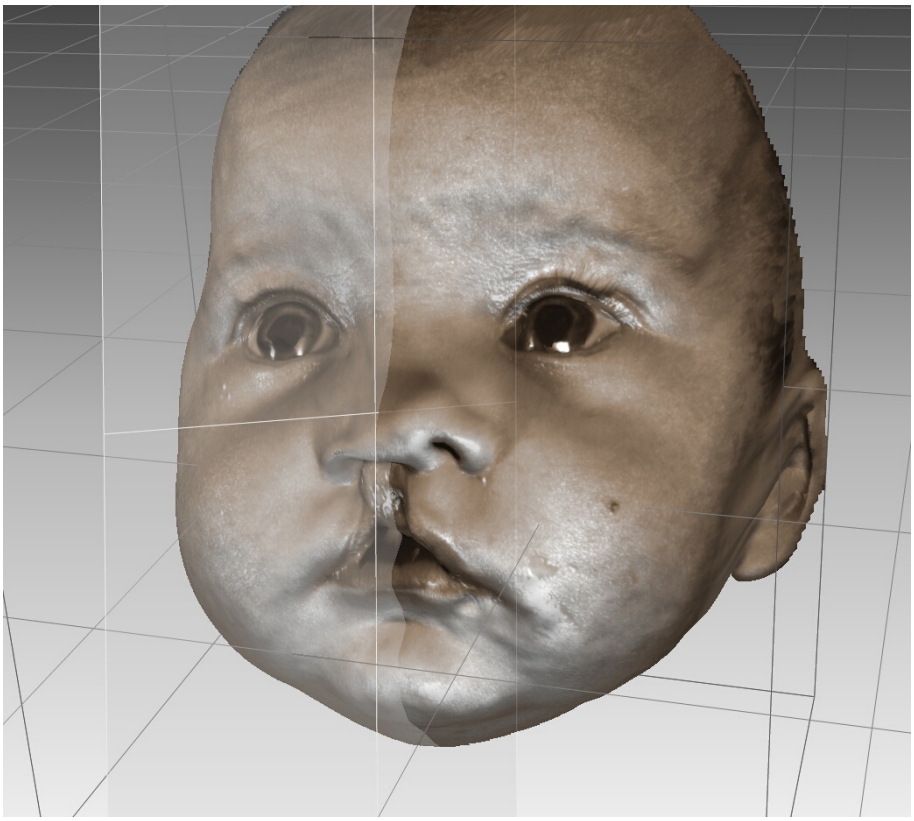

Figure 6.3: The cleft lip patient before operation. The symmetry plane is marked.

operation theater.

The plaster forms very nicely to the skin, so a full representation may be achieved. Unfortunately the mass exerts pressure on the skin, displacing the soft tissue. Consequentially the surface representation may never be correct. The procedure is time consuming (30 min), which is especially costly inside the operation theater. As the model is not available before the operation for planning, a positive is fabricated after the surgery. For further comparative measurements the plaster model or its negative have to be digitized with a conventional scanner.

The holographic technique is capable of capturing the face of the child with one short pulse (20 ns), no movement artifacts degrade the surface quality. This non-contact method is quick, convenient and safe for the young patient. The only challenge is to convince the child to look towards the holographic camera. The child usually sits on the parental lap, so a successful capture is easily manageable with common distraction and guidance techniques (goofing, talking, toys).

After hologram capture the reconstruction reveals the digital replicate of the patients face. The surface model is measured with a commercial engineering software, *RapidForm* from INUS technologies[1], which provides the functionality for distance measures, profiling, surface matching, data reduction and much more. Figure 6.3 shows a patient with the symmetry plane marked.

We use this commercial software at the initial phase of the project. Within the CO-ME[2] network a general platform for planning, navigation and simulation in surgery is developed.

For the first time it is now possible to capture the face of the young patients with good accuracy. The availability of the perfectly fitting surface texture additionally eases the identification of the respective landmarks of the cleft lip. The well known landmarks ([Far94], [SSH06]) are identified in the 3D model and distances and symmetries can be established (figure 6.3). Since this accomplishment is very young, we are still gaining experience towards the exhaustive exploitation

[1] http://www.rapidform.com

[2] The holographic scanning project was partly funded by the Swiss NCCR CO-ME (http://www.co-me.ch) , where efforts towards a computer aided surgery are concentrated.

of the data. In this project medical doctors, physicists and computer scientists are involved. Figure 6.1 shows an example of the processing of the data of a baby cleft patient before correction.

As can be seen, holographic topometry is accompanied with a lot of potential towards the clinical evaluation of dismorphologies. The accuracy and the image quality provides an excellent data base for the evaluation of cleft operations. The scans may be performed at any time before and after the operation, making these methods a valuable tool for documenting the healing progress and finally allow for the planing of surgical interventions. It is our future aim to monitor the growth of the correction over a longer time period by scanning the patients in defined intervals.

In the field of maxillofacial surgery the reception of the holographic topometry method is especially appreciative. The success of operation techniques may be validated and their individualization fostered.

Figure 6.4: Three views of a digital face model. The landmarks of the cleft lip are identified in the digital face model.

6.2 Soft tissue shift due to gravity

The appearance of the body is strongly determined by the effect of gravity on the skeleton and the soft tissue. The skin and underlying layers are well described, yet the reaction to external and internal forces is difficult to model. The elasticity modules of the tissue components are being investigated ([MPR+05], [WBN+04]), but the heterogeneous and anisotropic character still poses difficulties for computer simulation.

Figure 6.5: The difference between an upright (left) and reclined posture (right) is directly visible in a digital photograph. The images were taken at approximately the same distance with the same focal length.

The gravitational effect can be studied if the displacement between different orientations of the tissue can be quantified. The skin is tightly connected with underlying tissue, but nonetheless partly slides and deforms. Comparing the visual appearance of a person sitting and reclining (see figure 6.5), demonstrates the effect of gravity on the facial soft tissue.

In medicine and forensics the correspondence between a reclined and upright face is relevant for the appearance of a face. CT scans are recorded and the surgery is performed in reclined position, whereas the outcome of an operation is appraised in an upright position. The same accounts for forensics where the body is examined in a reclined position, but relevant for recognition is the upright posture. For these applications a compensation of the orientations would be essential. Consequently a differentiated soft tissue data base classified by gender, age, size, body mass index and ethic origin is needed.

The exact information of soft tissue shift gives the possibility to verify the validity of models used for computer simulations. The lack of exact soft tissue displacement measurement hampers the development of physically correct simulations. If the soft tissue displacement may be quantified a correction between reclined and upright position can be realized.

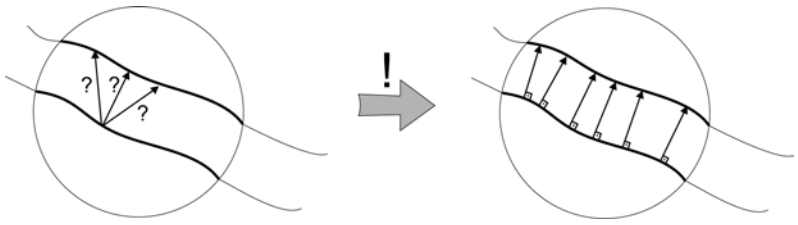

Figure 6.6: The aperture problem: When a line is tracked in a limited field-of-view the correspondence is ambiguous. By declaring the perpendicular shift vector as the distance this problem resolves.

The challenge in determining the soft tissue displacement is to establish the correspondence

between the two states of the face. As the skin not only moves perpendicular to the surface, but laterally as well. Consequently a volumetric assessment will not reveal the correct shift.

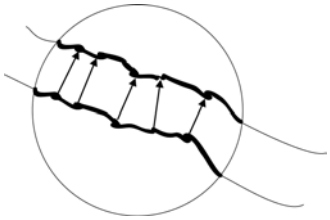

Figure 6.7: Unique features in the image (like the texture) may resolve the correspondence problem.

When a line segment is traced between two different states the determination of the correspondence has one degree of freedom (figure 6.6). It cannot be resolved where the a corresponding point moved to. It is the only reasonable solution to define the perpendicular distance at each point as the correspondence vector. This correspondence uncertainty is called aperture problem in image processing ([Jäh02]).

This ambiguity is resolved, when unique features are present in the image. With this additional knowledge the correspondence is well-defined and the displacement vector may be determined for each point (figure 6.7). So the intrinsic texture information from the holographic topometry is the key to a correct evaluation of the soft tissue shift.

Figure 6.8: Set-up for upright and reclined topometry. The proband wears a jig in each recording.

As shown in chapter 3.3 the holographic topometry method provides the surface and the texture information at the same time, both are aligned perfectly. No additional mapping is necessary, since both are extracted from the real image stack at the same location.

Position dependent measurement Two holograms are captured, one in a reclined position and one in an upright position. For the lying capture a 45^o first surface mirror is placed over the proband so the face is imaged in reflection with the regular portrait set-up. The person lays horizontally, perpendicular to the camera system, the head is supported by shell to allow a reliable positioning. The upright portrait is captured in the sitting position with a straight back.

The skull is the only reliable absolute reference object for registering the two models. Affixing the reference points to the soft tissue is insecure. We choose to fix the reference points to the jaw of the proband, who wears a jig (figure 6.9 b)). The purpose of the jig is to carry defined marker points that can be identified in the reconstructed image. The findings of this approach will help to identify facial landmarks or regions, which may be used to reliably register the respective models without the necessity for absolute registration points. We chose this approach to proof the concept of the registration process between the two views.

a)  b) 

Figure 6.9: a) The jig was fitted to the proband bite. b) White marker points with small holes of 200 μm spot size are fixed on wire extensions for later registration.

The jig fixates the closure of the jaw, it is fabricated specially to the proband's bite by a dental technician (figure 6.9 a)). To this jig we fix metal wires that extend outside the mouth towards the sides of the face. The construction is kept very slim to avoid a displacement of the lips as far as possible (figure 6.9 b)). The wires fork at the end, where two marker points are attached at each side. Each marker consist of a diffusely reflective foil, cut to a diameter of approximately 5 mm, penetrated by a small hole of 200 μm diameter. These holes are identified in the real image and used to register the two views.

Figure 6.10 shows the two models with the reference points identified as red spheres. The measurements of the models are performed with the software *RapidForm*. The lower cheeks of the models are not included, since these areas suffered from artifacts induced by the metal wires.

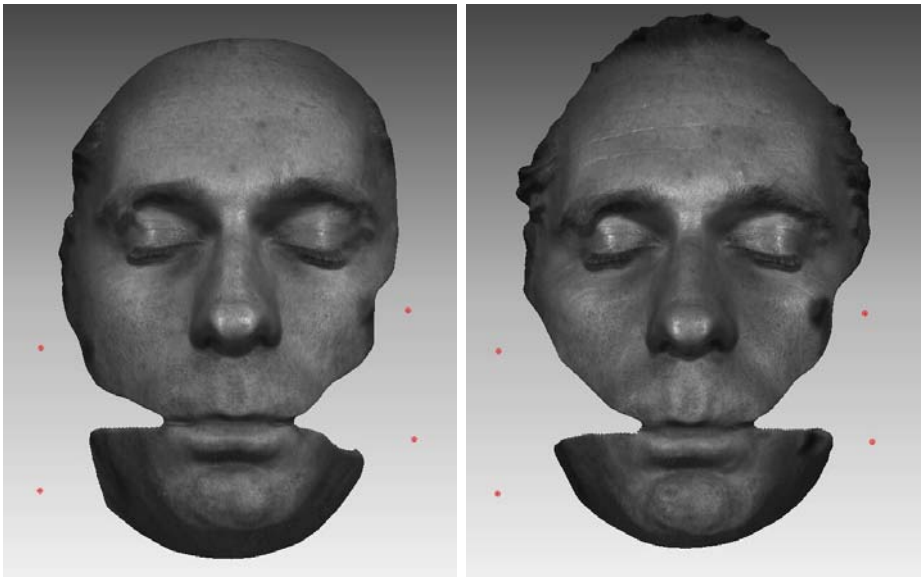

Figure 6.10: The captures resulted in two digital models of the proband, one reclined (left) and one upright position (right). Both cheeks are missing in this surface model, since these regions were strongly affected by artifacts form the wires suspending the marker points. The red balls beside the cheeks are the identified marker points.

The reference points are used to register the two views, which revealed a very good agreement between the two views (figures 6.13). The next step is the comparison between the two surfaces. Features of the skin like marks or skin pores are identified in both models and the shift between these points is calculated. This procedure is repeated for several prominent features on the model.

The general movement of the soft tissue surface can be estimated with this manual feature

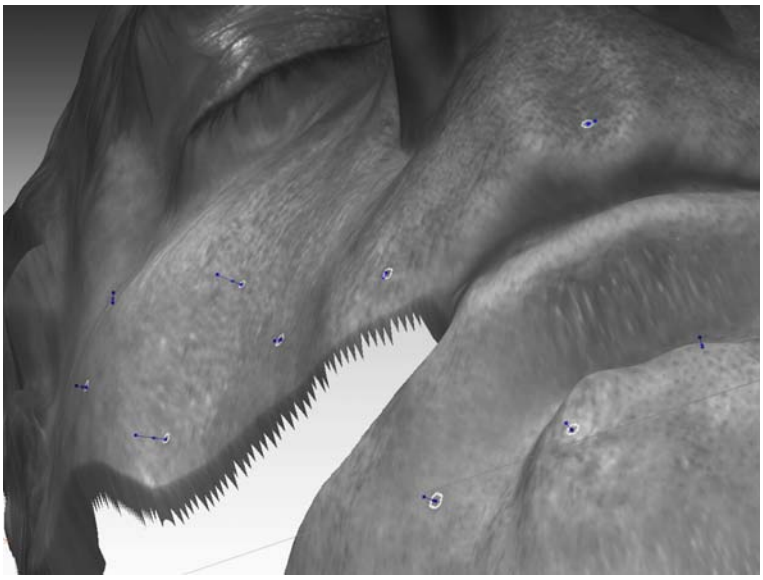

Figure 6.11: Closeup to the displacements in the chin and the cheek regions.

identification. From sitting to reclined position the soft tissue lifts up and shifts to the outwards. So the upper cheek moves towards the ears (figure 6.11). The displacement vector is largest in the upper cheek region where we quantify 6 mm, around the mouth the movement is less (2 mm). Both sides show a symmetrical behavior suggesting the successful registration of the two views.

The volumetric difference (figure 6.12) of the two face models estimates a much smaller displacement field of between 1 mm and 2.3 mm. As conjectured, a volumetric approach underestimates the displacement field by far. With the outlined approach, it is possible to identify the shift vectors manually, only a little number of features is identified. It is desirable to get a dense displacement vector field from the comparison of the two models. A technique based on optical flow might solve this task ([Jäh02, 419ff]).

The given results must be appreciated as first insights into the shift of the facial skin. Additionally to the above mentioned recordings, we captured the proband without the jig in all orientations. These measurements are free of the artifacts from the metal jig and show no protrusion of the lower lip. The measurements with jig presented above verifies the registration and will help to identify the candidate regions for a registration without a jig.

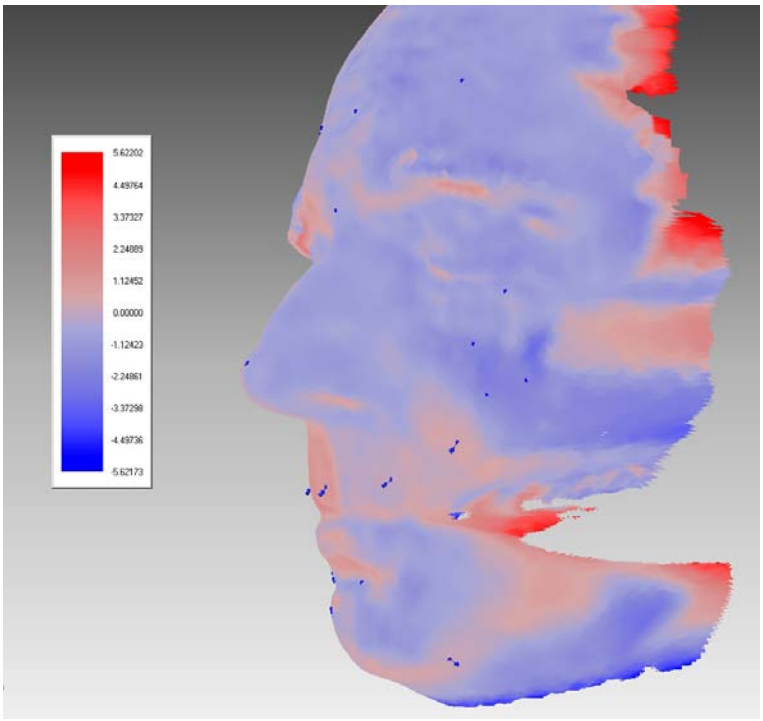

Figure 6.12: A color coded difference map from comparing the upright and the reclined face model volumetrically.

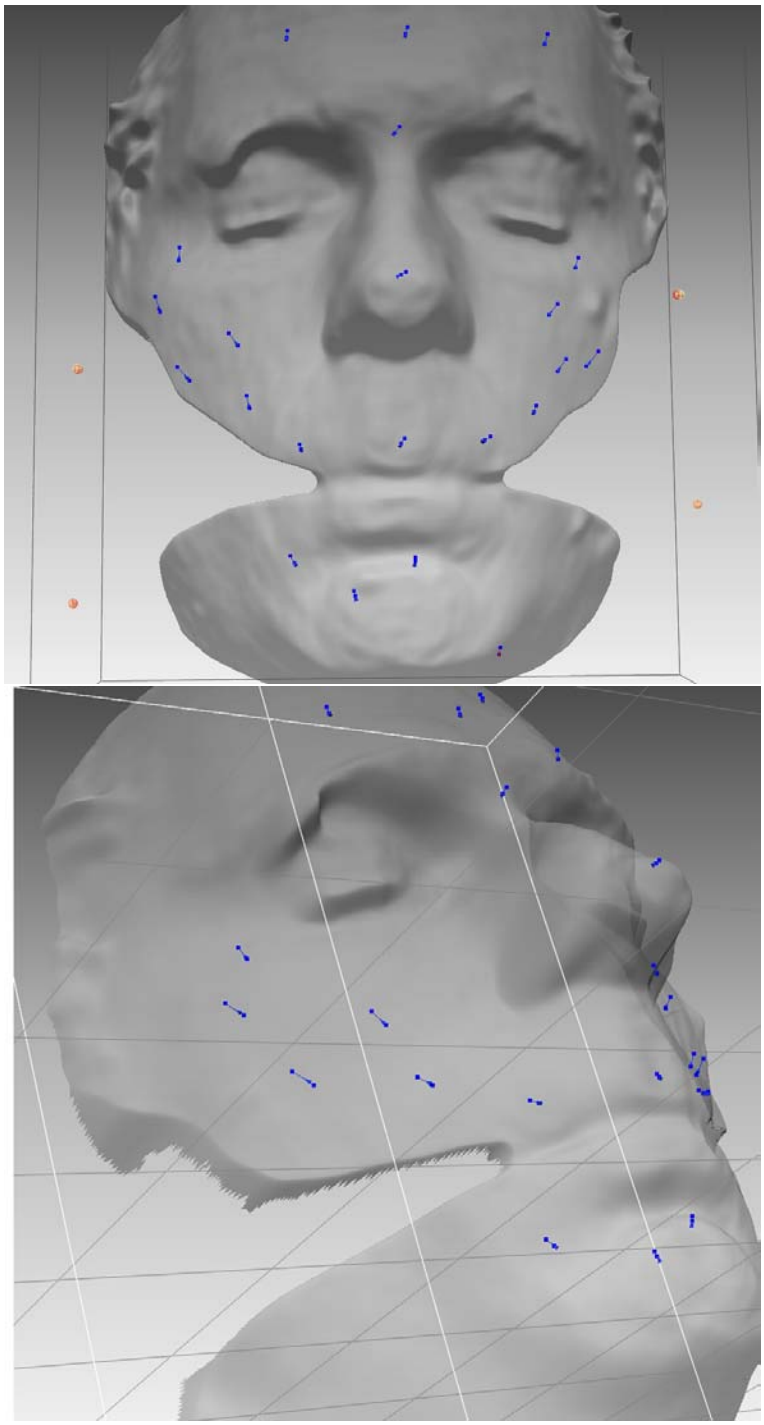

Figure 6.13: Two perspectives of the registered face models.

Chapter 7

Conclusion

7.1 Summary

This work deals with holographic topometry and its applications for facial measurements. Hologram topometry has the unique potential to capture the surface of a living subject even in motion and with an accurately fitting texture. Both tasks cannot be accomplished by any other method.

As a primer, both, the analog and the digital variants, are introduced and their common concepts outlined. The implications of hologram size and the resolution of the sensing material are described.

The capture and the evaluation processes are decoupled in the method. A pulsed hologram is captured with a short exposure time (20 ns) avoiding any motion artifacts in principle. The hologram contains the complete spatial information of the object, phase and amplitude are recorded. The real image is reconstructed, from which the surface is detected.

A holographic camera system for the mobile capture of analog holograms was presented in detail. The camera is the first mobile system with the possibility to capture the holograms in daylight. The components pulsed laser, beam formation, mechanical shutter and the software control are built to a compact system, which can be set up in 15 minutes in the field. This system enables us to perform measurement campaigns outside the lab. It is easy to operate and enables the use of the system in our partner hospital (University hospital Basel) by medical personnel.

The mobile camera asks for an adapted optical reconstruction unit. The reconstruction beam was designed to meet the high demands for the scanning of the real image without artifacts.

Improvements for real image digitization In the analog method, major innovations are introduced with this thesis. A replacement for the direct image scanning procedure was needed to eliminate the shortcomings of the CMOS flatbed scanner. The issues are speed, dynamic range, mechanical instability and image artifacts.

A stabilized CMOS scanner prototype was presented, which successfully removed artifacts and provided a better stability. Unfortunately the CMOS device still showed a low dynamic range due to the typical noise problem. As well the capture was still slow.

As a next generation a high performance scanning method was developed, which uses a X-ray flat panel detector (FPD) as an area sensor to capture each image at once. This instrument is an absolute novelty, which was co-developed with the manufacturer. The FPD was modified to fulfill the the optical sensing needs. The origin of degrading artifacts of the scanner were eliminated, gaining a sensor with excellent image quality and high frame rate.

The improvements introduced by this new instrument are manifold. With a frame rate of 10 Hz the time demand for the scanning process is reduced drastically from 2 hours down to only

30 seconds. The real image may now be monitored on-line and the sensor can be adjusted optimally to the laser intensity. The direct visual inspection of the real image finally allows a quick alignment of the hologram for reconstruction.

The output of the detector has a 12 bit resolution with only little noise equivalent, which is equivalent to a dynamic range of about 65 - 72 dB. Compared to low dynamic of the CMOS sensor (effective 5-6 bit, dynamic range 30 - 36 dB), this is a quantum leap. Dark and bright regions can be visualized easily at the same time, and the surfaces can be determined, even in regions of low image intensity variations. Even holograms with poor image contrast show good surface results.

With the absence of the selfoc lens the stripe artifacts disappeared, making a further compensation by smoothing dispensable, the inherent resolution reduction is avoided. The restricted field-of-view from the selfoc lens is also overcome. The distinctness of the contours increases through the complete image field due to the shorter Rayleigh length.

The mechanical stability eliminates alignment artifacts originating from the mechanical tolerances of the flatbed scanner. Since the monolithic sensor is rigid, it shows no image distortions due to the wobbling of the scan head. The scanner is positioned exactly perpendicularly to the scan axis which systematically resolved the random occurrence of geometric distortions. The resulting real image stack is free of geometric aberrations. With this newly gained image isotropy, comparisons between different 3D models are finally possible.

Digital hologram tomography The second absolute novelty is the digital hologram topometry which was developed newly during this thesis. A lot of effort was invested in basic research to finally arrive at a fully functional topometry system. A completely digital tomography has not been reported in literature.

A pulsed laser is used for recording a near in-line hologram on a CCD sensor. The field-of-view is restricted for digital holography due to limitations of the sensor resolution.

Three different cameras were presented to capture the holograms, a CMOS camera (PixeLink PL781M), an interline CCD camera (Kodak Megaplus ES 4.0) with 4 Mpixel and a full-frame CCD camera (DALSA FTF5066M) with 33 Mpixel. Due to its speed the Kodak interline camera was used throughout this thesis. The full frame sensor has a 8 times larger resolution than the interline CCD camera. (Unfortunately this custom design arrived too late to be included in this thesis).

The algorithms, necessary for the numerical reconstruction of digital holograms were implemented in Java. The Fresnel approximation was identified as appropriate for our needs. By using techniques for image improvement like mean value subtraction and high pass filtering the real image is removed of unwanted contributions. An optimized high pass filter was beneficial to the image quality.

With a simple scaling procedure we calculate image stacks with constant lateral scaling and a geometrically correct positioning. We optimized our reconstruction algorithms in C^{++} to benefit from the speed increase of roughly 10 times. A comparison of three implementations of the Fast Fourier transform (FFT) revealed the enormous speed boost, possible with an algorithm that performs the calculation on the graphics hardware. By using a hardware accelerated calculation a further speed step of 7-10 times was achieved. With this system an on-line reconstruction of the real image may be achieved, even for large scale images (2k x 2k pixels).

A unique gauging method was developed to adjust the reference beam origin merely by measuring a target of known extent. The sampling theorem teaches us that the field-of-view is indeed not limited to the Nyquist frequency and that illumination is most critical to avoid image overlap.

With an optimal illumination, human skin can already be visualized from digital holograms,

which is a major advance towards a topometry of the face. With structured illumination the surface visibility may be additionally enhanced for any given object.

It was demonstrated that surface maps can be established from numerically reconstructed image stacks. Due to the speckle pattern progression it is necessary to perform the scaling corrections after the surface finding. The texture and the height profile were extracted at the same time which has never been done like this before. The knowledge is derived from our expertise in analog holography. With the arrival of the full-frame sensor the accuracy of height profile will further increase.

Efforts to synthesize different perspectives are presented and show first promising results. It is the strategy to gauge the different perspectives by known targets and determine the transformation matrix in the object space. With the known transformation the real image stacks can be overlayed incoherently. The reference points are identified reliably already and the separate real image stacks are calculated. The views did not quite coincide. This will be accomplished by an improved alignment or a refined gauging procedure. By facilitating a better matching algorithm, it can be expected that this approach to aperture-synthesis will be fruitful in near future.

Applications of analog hologram topometry Two applications of analog hologram topometry were presented, both in tight connection with medicine. The shown applications can be realized exclusively by holographic topometry and are only feasible due to the instrumental improvements presented in this thesis.

The first example shows the planning possibilities and documentation for a cleft correction. These patients may not be captured with any 3D technique without prior immobilization of the patient. With only one pulse the analog hologram contains the necessary data for the surface extraction. The digitization and surface extraction were not possible with acceptable accuracy prior to this thesis. Only with the novel digitizer the slices can be recorded free of distortions. The subtle image contrast introduced by the infantile skin pores are detectable with the new device and lead to an excellent 3D surface model.

The surface model is loaded into an engineering tool where the distances of the landmarks are measured in 3D. Currently this 3D information is used solely for the documentation and evaluation of cleft correction techniques. We aim to integrate the new 3D topometry into the routine planning of cleft interventions with our clinical partner.

The second application shows the evaluation of gravitational effects on soft tissue. This study requires the precisely fitting texture for a tracking of the skin shift. The reconstruction benefits from the improved alignment, which results in geometrically undistorted 3D models.

The proband wears a jig which is steadily connected to the jaw. We used marker points of 200 μm size affixed to the jig to align the models. After registration of the models the soft tissue shift can be quantified. Prominent image texture features were identified and the corresponding points were tracked in the texture maps. With this manual method the shifts may be quantified for single points. The skin shifted maximally in the upper cheek region by 6 mm, compared to a volumetrically determined difference of only 1 - 2.3 mm.

The soft tissue shift of the face between an upright and a reclined person is of enormous interest to the medical field and the forensics. The findings will provide input to numerical simulations for soft tissue behavior and will help verify existing deformation models.

7.2 Perspectives

As demonstrated in this thesis, there is still a lot of potential for further developments in hologram tomography, in the digital as well as in the analog method.

In analog holographic topometry the new high-performance digitizer offers an on-line monitoring of the real image. With this, an automated hologram alignment is thinkable, which would further simplify the optical reconstruction process. With this measure a constant quality of the surface models may be secured.

In digital hologram topometry, the extent of the focus needs to be further reduced. One first step is the implementation of a new sensor, with a larger overall dimension.

The second approach for a focus reduction is the aperture synthesis. It is still a challenge to combine several perspectives into one real image. By solving this problem, the focus of the real image will be defined more sharply, making the surface extraction more precise. A simultaneous recording of multiple views is desirable to foster the advantage of a single fast exposure.

The computation on the graphics board showed an enormous speed-up in the wave field reconstruction. With this possibility an immediate, real-time visualization of the image stack may be realized.

With a migration to shorter wavelengths, the size of the resolvable structures decreases. By using a X-ray light sources, it is imaginable to produce holograms of single cells.

Appendix A

The Fourier transform

The one-dimensional *iFourier transform* of the function $f(x)$ is defined as

$$\mathcal{F}\{f(x)\} = F(u) = \int_{-\infty}^{\infty} f(x) exp[-i2\pi ux]dx. \tag{A.1}$$

The reverse operation, namely the reconstruction of an original signal form the Fourier spectrum is called *inverse Fourier transform.*

$$\mathcal{F}^{-1}\{F(u)\} = f(x) = \int_{-\infty}^{\infty} F(u) exp[i2\pi ux]du \tag{A.2}$$

The assignment between a pair $f(x)$ and $F(u)$ is unique, together they are called *Fourier-Transform pair.*

The Fourier transform is defined for one-dimensional signals as well as for multidimensional $f(x, y)$ data accordingly.

$$\mathcal{F}\{f(x,y)\} = F(u,v) = \int_{-\infty}^{\infty}\int_{-\infty}^{\infty} f(x,y) exp[-i2\pi(ux+vy)]dxdy \tag{A.3}$$

and the according inverse:

$$\mathcal{F}^{-1}\{F(u,v)\} = f(x,y) = \int_{-\infty}^{\infty}\int_{-\infty}^{\infty} F(u,v) exp[i2\pi(ux+vy)]dudv. \tag{A.4}$$

For a numerical computation, the function is sampled in discreet steps. This yields the two dimensional discreet Fourier transfrom (DFT) and its reverse.

$$F_{mn} = \frac{1}{N^2}\sum_{k=0}^{N-1}\sum_{l=0}^{N-1} f_{kl} exp[-i2\pi(\frac{km+ln}{N})] \tag{A.5}$$

$$f_{kl} = \sum_{m=0}^{N-1}\sum_{n=0}^{N-1} F_{mn} exp[i2\pi(\frac{km+ln}{N})]. \tag{A.6}$$

The maximal frequency is determined by the sampling interval in the spatial domain:

$$u_{max} = N\Delta u = \frac{1}{\Delta X} \tag{A.7}$$

Bibliography

[Ans70] D. A. Ansley. Techniques for pulsed laser holography of people. *Applied Optics*, 9:815, 1970.

[BB05] Wilhelm Burger and Mark J. Burge. *Digitale Bildverarbeitung. Eine Einführung mit Java und ImageJ.* Springer, Berlin, 2005.

[BCL02] R. Binet, J. Colineau, and J.-C. Lehureau. Short-Range Synthetic Aperture Imaging at 633 nm by Digital Holography. *Applied Optics*, 41(23):4775–4782, August 2002.

[Bje95] H. I. Bjeklhagen. *Silver-Halide Recording Materials for Holography and Their Processing.* Springer-Verlag, Berlin Heidelberg New-York, 1995.

[Bon02] J. Bongartz. *Hochauflösende dreidimensionale Gesichtsprofilvermessung mit kurzgepulster Holographie.* PhD thesis, Mathematisch Naturwissenschaftliche Fakultät der Heinrich-Heine-Universität Düsseldorf, 2002. http://docserv.uni-duesseldorf.de/servlets/DocumentServlet?id=2192.

[BTG+06] S. A. Blackwell, R. V. Taylor, I. Gordon, C. L. Ogleby, T. Tanijiri, M. Yoshino, M. R. Donald, and J. G. Clement. 3-d imaging and quantitative comparison of human dentitions and simulated bite marks. *Int J Legal Med*, 4(1):1–9, 2006.

[CMD00] E. Cuche, P. Marquet, and C. Depeursinge. Spatial filtering for zero-order and twin image elimination in digital off-axis holography. *Appl Opt*, 39(23):4070–4075, 2000.

[CNG01] T. E. Carlsson, B. Nilsson, and J. Gustafsson. System for acquisition of three-dimensional shape and movement using digital Light-in-Flight holography. *Optical Engineering*, 40:67–75, January 2001.

[Cut90] L. J. Cutrona. *Synthetic aperture radar.* McGraw-Hill, 1990.

[dFu] Berufsgenossenschaft der Feinmechanik und Elektrotechnik. Berufsgenossenschaftliche Vorschrift für Sicherheit und Gesundheit am Arbeitsplatz. Unfallverhütungsvorschrift Laserstrahlung vom 1. April 1988 in der Fassung vom 1. Januar 1997 mit Durchführungsanweisung vom Oktober 1995.

[Die02] T. Dierig. *Gewinnung von Tiefenkarten aus Fokusserien.* PhD thesis, Fakultät für Physik und Astronomie der Ruprecht-Karls-Universität Heidelberg, 2002.

[DMS03] N. Demoli, J. Mestrovic, and I. Sovic. Subtraction digital holography. *Apl Opt*, 42:798–804, February 2003.

[EA93] J. Eichler and G. Ackermann. *Holographie.* Springer Verlag, Berlin, 1993.

[Far94] L. G. Farkas. *Anthropometry of the Head and Face.* Raven Press New York, 2nd edition, 1994.

[fft] http://www.fftw.org.

[Fre05] S. Frey. *Three-dimensional facial measurement by portrait holography and texture-based focus detection.* PhD thesis, Mathematisch Naturwissenschaftliche Fakultät der Heinrich-Heine-Universität Düsseldorf, 2005. http://docserv.uni-duesseldorf.de/servlets/DocumentServlet?id=3166.

[Gab48] D. Gabor. A new microscopic principle. *Nature*, 161:777–778, 1948.

[Gab49] D. Gabor. Microscopy by reconstructed wave-fronts. *Proceedings of the Royal Society of Biology*, A 197:454–487, 1949.

[Gat86] J. W. C. Gates. The influence of holography on measurement technology. *Journal of Physics E-scientific Instruments*, 19:998–1007, 1986.

[Gie03] D. Giel. *Hologram Tomography for Surface Topometry.* PhD thesis, Mathematisch Naturwissenschaftliche Fakultät der Heinrich-Heine-Universität Düsseldorf, 2003. http://docserv.uni-duesseldorf.de/servlets/DocumentServlet?id=2598.

[Gis05] N. Gisbert. Helligkeitsbasierte Registrierung von Farbinformationen auf holographisch gewonnene Gesichtsmodelle. Master's thesis, Fakultät Digitale Medien der Fachhochschule Furtwangen, 2005.

[Goo05] J. W. Goodman. *Introduction to Fourier Optics.* Roberts and Company, 3rd edition, 2005.

[GSRP05] J. Garcia-Sucerquia, J. H. Ramírez, and D. V. Prieto. Improvement of the signal-to-noise ratio in digital holography. *Revista mexicana de física*, 51(1):76–81, 2005.

[Har96] P. Hariharan. *Optical Holography. Principles, Techniques and Applications.* Cambridge University Press, 1996.

[Hei06] S. Heintz. Einsatz der digitalen Holographie im Verfahren für die 3d Oberlächenerfassung. Master's thesis, Fakultät Digitale Medien der Fachhochschule Furtwangen, 2006.

[Hol98] G. C. Holst. *CCD Arrays Cameras and Displays.* JCD Publishing, 2nd edition, 1998.

[Jäh02] B. Jähne. *Digitale Bildverarbeitung.* Springer-Verlag, Berlin Heidelberg, 2002.

[Joh06] Sean F. Johnston. *Holographic Visions : A History of New Science.* Oxford University Press, 2006.

[JS04] M. Jacquot and P. Sandoz. Sampling of two-dimensional images: prevention from spectrum overlap and ghost detection. *Optical Engineering*, 43:214–223, January 2004.

[KAJ02] Thomas M. Kreis, Mike Adams, and Werner P. O. Jueptner. Aperture synthesis in digital holography. volume 4777, pages 69–76. SPIE, 2002.

[KCJ+98] Schwenzer K., Holberg C., Willer J., Mast G, and Ehrenfeld M. 3-d imaging of the facial surface by topometry using projected white light strips. *Mund Kiefer GesichtsChir*, 2(1):130–134, 1998.

[KDI+06] Schwenzer-Zimmerer K., Chaitidis D., Borner B. I., Kovacs L., Sader R., Zeilhofer H. F., and Holberg C. Lip, jaw, and palate clefts: Analysis of unilateral cleft lip using 3-d laser topometry. *Mund Kiefer GesichtsChir*, 10(6):377–384, Nov 2006. German.

[KF86] Miles V. Klein and Thomas E. Furtak. *Optics, 2E.* Wiley, 1986.

[KG02] K. Khare and N. George. Direct sampling and demodulation of carrier-frequency signals. *Optics Communications*, 211:85–94, October 2002.

[KG03] K. Khare and N. George. Direct coarse sampling of electronic holograms. *Optics Letters*, 28(12):1004–1006, June 2003.

[KJ97] T. Kreis and Jüptner. Suppression of the DC term in digital holography. *Opt Eng*, 36(8):2357–2360, 1997.

[Kre02a] T. Kreis. Frequency analysis of digital holography with reconstruction by convolution. *Opt Eng*, 41(9):1829–1839, 2002.

[Kre02b] T. M. Kreis. Frequency analysis of digital holography. *Optical Engineering*, 41:771–778, April 2002.

[Lad04] N. Ladrière. Optische und chemische Aspekte der hochauflösenden, vollautomatischen Hologrammentwicklung. Master's thesis, Fachbereich Photoingenieurwesen und Medientechnik der Fachhochschule Köln, 2004.

[Lat71] J. N. Latta. Computer-based analysis of hologram imagery and aberrations. I. Hologram types and their nonchromatic aberrations. *Applied Optics*, 10(3):599–608, 1971.

[LBC+02] M. Liebling, T. Blu, E. Cuche, P. Marquet, C. Depeursinge, and M. Unser. A novel non-diffractive reconstruction method for digital holographic microscopy. *Biomedical Imaging*, pages 625– 628, 2002.

[LFT+04] N. Ladrière, S. Frey, A. Thelen, S. Hirsch, J. Bongartz, D. Giel, and P. Hering. Ultraschnelle holografische Gesichtsprofilvermessung mit vollautomatischer Hologrammentwicklung. In *Aktuelle Methoden der Laser- und Medizinphysik*, pages 272–274. VDE-Verlag, 2004.

[LGC01] F. Le Clerc, M. Gross, and L. Collot. Synthetic-aperture experiment in the visible with on-axis digital heterodyne holography. *Optics Letters*, 26(20):1550–1552, October 2001.

[LK03] W. Lauterborn and T. Kurz. *Coherent Optics*. Springer-Verlag, Berlin, Heidelberg, 2003.

[LKW02] S. Li, J. T. Kwok, and Y. Wang. Multifocus image fusion using artificial neural networks. *Pattern Recognition Letters*, 23:985–997, 2002.

[LLB+02] C. Liu, Z. Liu, F. Bo, Y. Wang, and J. Zhu. Super-resolution digital holographic imaging method. *Applied Physics Letters*, 81(17):3143–3145, October 2002.

[LU62] E. N. Leith and J. Upatnieks. Reconstructed wavefronts and communication theory. *Journal of the Optical Society of America*, 52(10):1123–1130, 1962.

[LU63] E. N. Leith and J. Upatnieks. Wavefront reconstruction with continuous-tone objects. *Journal of the Optical Society of America*, 53:1377–1381, 1963.

[LU64] E. N. Leith and J. Upatnieks. Wavefront reconstruction with diffused illumination and three-dimensional objects. *Journal of the Optical Society of America*, 54:1295–1301, 1964.

[Mas02] J. H. Massig. Digital off-axis holography with a synthetic aperture. *Optics Letters*, 27(24):2179–2181, December 2002.

[Mei65] R.W. Meier. Magnification and third-order aberrations in holography. *Journal of the Optical Society of America*, 55:987–992, 1965.

[MMP+02] Krimmel M., Bacher M., Cornelius C. P., Schubert S., Göz G., and Reinert S. 3-dimensionale Bildakquisition zur Analyse der primären spaltbedingten Gesichtsdeformität mit optoelektronischem Oberflächenscanner. *Mund Kiefer GesichtsChir*, 6:157–161, 2002.

[MPR+05] E. Mazza, O. Papes, M. Rubin, S. Bodner, and N. S. Binur. Nonlinear elastic-viscoplastic constitutive equations for aging facial tissue. *Biomechanics and Modeling in Mechanobiology*, 4:178–189, 2005.

[MWLJ04] L. Ma, H. Wang, Y. Li, and H. Jin. Numerical reconstruction of digital holograms for three-dimensional shape measurement. *Journal of Optics A: Pure and Applied Optics*, 6:396–400, 2004.

[NN94] S. K. Nayar and Y. Nakagawa. Shape from focus. *IEEE Transactions on Pattern Analysis and Machine Intelligence*, 16:824–830, 1994.

[oNI00] International commision on non-ionizing radiation protection. revision of guidelines on limits on exposure to laser radiation of wavelength between 400nm and 1.4μm. *Health Physics*, 79(4):431–440, 2000.

[OSH05] J. D. Owens, S. Sengupta, and D. Horn. Assessment of Graphic Processing Units (GPUs) for Department of Defense (DoD) Digital Signal Processing (DSP) Applications. October 2005.

[Ras06] W. Rasband. ImageJ. Image processing and analysis in Java, 2006. http://rsb.info.nih.gov/ij/.

[Rog50] G. L. Rogers. Gabors diffraction microscopy: The hologram as a generalized zone-plate. *Nature*, 166:236–237, 1950.

[RS03] P. K. Rastogi and A. Sharma. Systematic approach to image formation in digital holography. *Optical Engineering*, 42:1208–1214, May 2003.

[Sch94] U. Schnars. Direct phase determination in hologram interferometry with use of digitally recorded holograms. *Journal of the Optical Society of America A*, 11:2011–2015, July 1994.

[Sie68] L. D. Siebert. Large scene front-lighted hologram of a human subject. *Proceedings of the Institude of Electrical and Electronics Engineers*, 56:1242–1243, 1968.

[Sie86] A. E. Siegmann. *Lasers*. University Press, Oxford, 1986.

[SJ94] U. Schnars and W. P. Jueptner. Direct recording of holograms by a CCD target and numerical reconstruction. *Appl Opt*, 33:179–181, January 1994.

[SJ05] Ulf Schnars and Werner Jueptner. *Digital Holography: Digital Hologram Recording, Numerical Reconstruction, and Related Techniques*. Springer, 2005.

[SJ06] A. Stern and B. Javidi. Improved-resolution digital holography using the generalized sampling theorem for locally band-limited fields. *J Opt Soc Am A Opt Image Sci Vis*, 23(5):1227–35, 2006.

[sla] http://www.slavich.com.

[SM00] A. Stadelmaier and J. H. Massig. Compensation of lens aberrations in digital holography. *Optics Letters*, 25(22):1630–1632, November 2000.

[SSH06] G. R. J. Swennen, F. Schutyser, and J.-E. Hausamen. *Three-Dimensional Cephalometry*. Springer, 2006.

[ST98] M. Subbarao and J. Tyan. Selecting the optimal focus measure for autofocusing and depth-from-focus. *IEEE Transactions of Pattern Analysis and Machine Iintelligence*, 20:864–870, 1998.

[The03] A. Thelen. Holographische Topometrie: Off-Axis Effekte in der Digitalisierung holographischer Rekonstruktionen. Master's thesis, Mathematisch-Naturwissenschaftliche Fakultät der Rheinischen Friedrich-Wilhelms-Universität Bonn, 2003.

[The06] A. Thelen. *Optimized surface extraction from holographic data.* PhD thesis, Mathematisch-Naturwissenschaftliche Fakultät der Heinrich-Heine-Universität Düsseldorf, 2006. http://docserv.uni-duesseldorf.de/servlets/DocumentServlet?id=3430.

[TW81] B. A. Tozer and J. M. Webster. Holography as a measuring tool. *Journal of Photographic Science*, 28:93–98, 1981.

[VR02] VDI / VDE-Richtlinien. Opitsche 3d-Messsysteme: Blatt 2: Bildgebende Systeme mit flächenhafter Abtastung - optical 3-d measuring systems, optical systems based on area scanning, 2002. VDI/VDE 2634.

[VRM97] VRML97. The virtual reality modelling language: ISO / IEC 14772-1:1997, 1997. http://www.web3d.org/x3d/specifications/vrml/.

[WBN+04] S. Weiss, M. Bajka, A. Nava, E. Mazza, and P. Niederer. A finite element model for the simulation of hydrometra. *Technology and Health Care*, pages 259–267, 2004.

[WLJ+03] H. Wang, Y. Li, H. Jin, C. Yin, X. Su, and W. Chen. Three-dimensional visualization of shape measurement data based on a computer generated hologram. *Journal of Optics A: Pure and Applied Optics*, 5:195–+, September 2003.

[YAC02] L. Yu, Y. An, and L. Cai. Numerical reconstruction of digital holograms with variable viewing angles. *Optics Express*, 10(22):1250–+, November 2002.

[YFB02] R. M. Yin, P. J. Flynn, and S. L. Broschat. Position-dependent defocus processing for acoustic holography images. *International Journal of Imaging Systems and Technology*, 12:101–111, 2002.

[YIYY06] I. Yamaguchi, T. Ida, M. Yokota, and K. Yamashita. Surface shape measurement by phase-shifting digital holography with a wavelength shift. *Appl Opt*, 45:7610–7616, October 2006.

[YYMY06] I. Yamaguchi, K. Yamamoto, G. A. Mills, and M. Yokota. Image reconstruction only by phase data in phase-shifting digital holography. *Appl Opt*, 45:975–983, February 2006.

[Zep05] A. Zepp. Aufnahme und Rekonstruktion von Hologrammen unter Verwendung von Spiegeln zur Aperturvergrößerung. Master's thesis, Fachbereich Lasertechnik des RheinAhrCampus Remagen, Fachhochschule Koblenz, 2005.

Acknowledgements

In the first place I thank Prof. Dr. Hering for investing the time and effort in me and giving me the opportunity to work with this extremely interesting subject. Additionally I thank Prof. Dr. Schierbaum for accepting the second referee of this work.

My deepest gratefulness belongs to my family Gerit, Paul, Elva, Bruno and Frida. Without them and their patience this undertaking would not have been successful. We went this winding path together and may we continue for a long time.

My coworkers at caesar were an enrichment for me and I would like to thank Dr. Andrea Thelen, Dr. Susanne Frey for the fruitful discussions over the years as well as the former colleague Natalie Ladriere.

The new coworkers in the holography group, Stephanie Heintz, Nicola Gisbert helped me enormously during the finishing of this work.

The extended work group of the CO_2 laser cutting group with Dr. Mikhail Ivanenko, Dr. Martin Werner, Manfred Klasing were true companions over the past years as well as the new students Daniela Harbecke and Henne Steigerwald. The former students Andreas Zepp and Oliver Gisbert are also remembered well. Jolanta Kremer kindly supported my with proofreading.

My Belgian friend Frank I thank for the good and fruitful atmosphere during our gravity effect experiments and for providing me with prosperous career alternatives.

Prof. Dr. Jens Bongartz from the Fachhochschule Remagen was always present for academic discussions and finally he was the one attracting me to caesar. Urs Fries I owe thanks and numerous favors for his advisory over the past years.

I like to thank the caesar foundation for providing a pleasant atmosphere and all the possibilities over the past years. With Prof. Dr. Karl-Heinz Hoffmann, Dr. Hartwig Bechte, Margeret Schilling and Francis Hugenroth I would like to name but a few from this institution. They supported my exhibition project "marthavision" at caesar.

One part of my work was accomplished at the High-Tech Forschungszentrum der Mund-Kiefer-Gesichtschirurgie of the University hospital in Basel under the direction of Prof. Dr. Dr. H.-F. Zeilhofer, where I was warmly welcome by many of the colleagues. Besides the valuable experiences in Switzerland, the atmosphere there was very enlightening and many friendships spun out of this intense work relation. I would like to thank especially Dr. Dr. Katja Schwenzer-Zimmerer nebst Ehemann Stefan for her continued support and productive collaboration. Many thanks go to the team related to the holography project: Thoralf Seewald, Dr. Zdsislaw Krol, Isabelle Börner, Prof. Dr. Dr. Robert Sader, and not to forget Francesca and the numerous unmentioned but nonetheless well respected colleagues.

I gratefully thank all the people who have contributed to the holography project and who helped me during the course of this thesis.

A special thank goes to CO-ME, who partly funded the holography project, and in representation their (former) CEO Prof. Dr. Bert Müller. With Tina, Stefan, Arzu we had a fabulous time preparing the Luzern workshop.

For the steady support I would like to thank my parents Karin and Detlef and the Hirsch family Brigitte and Christian.